1975

THE ELECTROLESS PLATING SYSTEM AND THE MICROSTRUCTURE AND ELECTRICAL PROPERTIES OF ELECTROLESSLY DEPOSITED THIN METAL FILMS.

SHUI-LEE. CHOW
University of Windsor

THE ELECTROLESS PLATING SYSTEM AND THE MICROSTRUCTURE AND ELECTRICAL PROPERTIES OF ELECTROLESSLY DEPOSITED THIN METAL FILMS

by

SHUI-LEE CHOW

A Dissertation

Submitted to the Faculty of Graduate Studies through the Department of Physics in Partial Fulfillment of the Requirements for the Degree of Doctor of Philosophy at the University of Windsor

Windsor, Ontario, Canada

1974

ABSTRACT

A comparative study of the transmission electron micrographs and diffraction patterns in the different stages of the electroless plating process has been made. Investigations of the structure and measurements of electrical resistivity and Hall effect in electroless thin films of nickel and cobalt have also been made. The comparisons were made using conventional ($SnCl_2$/HCl), ($PdCl_2$/HCl) sensitizer and activating solutions, a newly developed system based upon the incorporation of aged stannic component and a commercial catalytic system ($SnCl_2$/$PdCl_2$/HCl) in conjunction with various accelerating solutions. Results of electron micrographs have demonstrated that the use of the improved method or the commercial catalytic solution increases the catalytic site density by one order of magnitude. Besides, they have also resulted in the formation of finer and denser metal particles during the early stages of nucleation and growth. Electron diffraction analysis indicate that the deposit after the acceleration step is f.c.c. Pd_3Sn. In addition, it was found that the best plating results for surfaces treated with catalytic solution are obtained whenever Pd_3Sn is present on the substrate surface. Also, ultra-violet light is effective in inhibiting the electroless deposition of copper, nickel and cobalt if applied after sensitization, and of nickel and cobalt after activation. It is concluded that structural changes in the sensitizing and activating agents induced by the u.v. light are connected with the inhibition of metal deposition.

High resolution electron micrographs and diffraction patterns of thin films of nickel and cobalt deposited electrolessly under various conditions are presented. It is concluded that nickel, when deposited from strongly alkaline solutions assumes a f.c.c. structure. Evidence is presented that the structure of cobalt deposits can be either f.c.c. or h.c.p. depending on the chemistry of the metalization solution. Mixed cobalt-nickel films appear to form a f.c.c. structure like nickel.

No crystalline structure changes have been observed in thin films of cobalt and nickel when annealed in vacuum in the temperature ranges of 290°-450°K, however, an irreversible change in sheet resistivity was observed. This kind of irreversible change in sheet resistivity is attributed to the desorption of gases and the annihiliation of the micro-crystallites. The sheet resistivity of as-deposited thin films of nickel and cobalt was found to be much too high to be explained by the size effect theory of Fuchs and Sondheimer. Again, absorbed gases are considered to be the major contribution to the observed high sheet resistivity.

Hall effect measurements have established that the charge carriers in electroless Ni-P films are electrons, while those of Co-P and Ni-Co-P (65% Ni) films are holes. The high Hall mobility in heat treated Ni-Co-P and Co-P films is attributed to the ferromagnetic properties of these films. The very low Hall mobility of as-deposited thin films of Ni-Co-P and Co-P is attributed to their discontinuous structure.

No appreciable variation as a function of sheet resistivity

was observed in extraordinary Hall coefficient for thin metal films deposited electrolessly; however, for thicker films, it has been observed that the extraordinary Hall coefficient decreases with increasing film thickness.

ACKNOWLEDGEMENTS

I am greatly indebted to Professor M. Schlesinger for suggesting the research project and constant encouragement. I would like to express my gratitude to Professor M. Schlesinger and Professor N. E. Hedgecock for many stimulating suggestions and discussions. I would also like to take this opportunity to thank Mr. B. Sears for the technical assistance in electron microscopy.

I dedicate my appreciation to my parents Mr. and Mrs. C. F. Chou without their faith this work probably never would have been completed.

Last, but not the least, the financial assistance from the Physics Department is also acknowledged.

TABLE OF CONTENTS

FIGURE CAPTIONS

Page

LIST OF TABLES

INTRODUCTION

Thin films have very large surface-to-volume ratios, and consequently, the surface greatly influences the film's properties. In fact, a number of fundamental questions about a given substance can best be answered by an examination of the material's property in film form. For example, much of the recent insight into the mechanism of super-conductivity came in connection with the study of thin film samples. It is also hoped that study of very thin films might provide further understanding into the properties of liquid state.

In recent years, thin metal films deposited by the electroless process [1] have attracted the interest of a number of workers. This is largely so because of the considerable technical potential this kind of film has. Ni-P deposits have been used as resistors for some time already. Meanwhile, thin films of cobalt have replaced ferric-oxide films as recording tapes. They are also used often for very high density digital magnetic recording. The successes of such films for these purposes are due to their thinness, high coercive force and high magnetic-moment density, etc. Another rather interesting characteristic that these films have is the relative ease with which they can be selectively deposited. This special property should find its application in the electronic industry.

Selective electroless plating also lends itself to the forming of precision metal parts and eliminates typical problems of undercutting commonly observed in etch down processes. The technique of selective

deposition of metals on dielectric substrates can be achieved by a variety of methods, of which ultraviolet irradiation has been demonstrated to be very effective [2,3].

In the art of plating on dielectric substrates, chemical treatment of the surface is an essential step required for the initiation of the electroless plating processes. Although quite a number of chemical systems for metal deposition have been developed [4], little is understood about the actual mechanisms which govern the physical chemistry of these systems. With the increased interest of commercial applications, several investigators [5,6,7,8] have examined the mechanisms of the pretreatment systems, the nature of the treated surfaces, as well as the nucleation and growth of thin metallic films. It has been generally demonstrated that the nucleation and growth of the electroless thin films is initiated at catalytic sites [5,6].

Marton and Schlesinger [6] have investigated previously the nucleation and growth of thin electroless Ni-P deposits. Sard [6] has carried out similar studies on electroless copper deposits. The nucleation and growth of electroless Co-P deposits have been studied to some extent by Frieze et.al.[9]. The nucleation and growth of electroless Ni-Co-P deposits have, however, been omitted.

Because of their practical applications, most investigators [10,11-16] devoted special attention to the magnetic properties of electroless Co-P deposits with almost complete omission of their electrical properties.

In the present investigation, transmission electron microscopy techniques have been employed to study the nature of the treated surfaces, the nucleation and growth of electroless thin films of Ni-P, Ni-Co-P and Co-P. The electrical properties of these metallic films were studied by combining the electrical resistivity and Hall effect measurements.

These experiments were undertaken with the aim of adding to the understanding of the co-relationships between structures and electrical properties. It is also intended to provide further insight into various debated aspects of electroless plating. Specifically:

1) the role of u.v. light irradiation in the inhibition of electroless deposition,
2) the actual microscropic and chemical processes responsible for the pretreatment stages,
3) the chemical nature of the sensitized and/or activated or catalyzed surface prior to plating.

The materials present in this dissertation can be divided into three sections. The first section deals mainly with the chemical treatment of the substrate surfaces for subsequent electroless deposition. The second section describes the structures of electrolessly deposited metallic thin films. The last section presents the electrical properties, i.e. electrical resistivity and Hall effect, of these metallic thin films.

CHAPTER I

GENERAL BACKGROUND

(I) Principle of Electroless Deposition

1. Introduction

"Electroless Deposition", a name first suggested by Brenner and Riddel [1], can be described as a controlled autocatalytic chemical reaction for metal deposition. It resembles electroplating in that the process may be run continuously to build up a thicker coating. It differs from a displacement process in that the electroless process deposits metal only on a catalytic surface.

To be more specific, electroless deposition is a process whereby the metal ions in an aqueous solution are reduced to the metallic state by a suitable reducing agent which is simultaneously oxidized in the course of the reaction.

The essential chemicals in an electroless bath are a simple metal salt, a reducing agent, a buffer and a complexing agent. The function of the complexing agent is to prevent the spontaneous precipitation of metal salt. The action of the buffer is to keep the pH of the electroless bath from dropping too rapidly and hence stopping the reaction.

2. Electroless Nickel Plating

For the electroless deposition of nickel, the process involves the reducing action of hypophosphite in a solution of nickel ions in the

presence of certain catalytic metals. The reaction can be expressed by the following equations:

$$(1)\quad Ni^{++} + H_2PO_2^- + H_2O \rightarrow Ni + 2H^+ + H_2PO_3^-$$

$$(2)\quad H_2PO_2^- + H_2O \rightarrow H_2PO_3^- + H_2\uparrow$$

It may be seen from the above equations that the hypophosphite undergoes oxidation to phosphite, and nickel ions are reduced to the metallic state. Experimentally, it has been found that the rate of deposition of electroless nickel depends on the concentration of hypophosphite and on the pH value of the metalizing bath. Based on these results, Brenner and Riddel [1] postulated a two-step intermediate mechanism. They believe that the rate of deposition is determined by the catalytic decomposition of the hypophosphite to hypophosphate and hydrogen. The hydrogen produced then reduces the nickel ions on the catalytic surface. The overall utilization of hypophosphite for reducing nickel is only about 37% under the best conditions. On the other hand, Gutzeit [17] considered that hydrogen and metaphosphite are products of the catalytic dehydrogenation of the orthophosphite on the catalytic surface. The atomic hydrogen is adsorbed on the catalytic surface, and reduces nickel ions to metallic state. In the meantime, the metaphosphite ion reacts with water to form the orthophosphite ion. Hence a fresh nickel surface is found constantly and the reaction proceeds autocatalytically. The overal reaction can be expressed as:

$$(3)\quad H_3PO_2^- + \text{Catalyst} \rightarrow PO_2^- + 2H$$

(4) $Ni^{++} + 2H \rightarrow Ni + 2H^{+}$

(5) $PO_2^{-} + H_2O \rightarrow HPO_3^{--} + H^{+}$

For the plating of nickel on silicon substrates, Iwasa et.al. [18] suggested a "local cell" model. They considered the oxidation of hypophosphite to be an anodic reaction, and the reducing of nickel ions by atomic hydrogen to be a cathodic reaction. The rate of deposition is thus determined from the migration of the electrons (or holes) in the substrate surface. The overall reaction is given by:

(6) Diffusion of reactants to the interface

$$H_2PO_2^{-} + H_2O \rightarrow H_2PO_3^{--} + 2e^{-} + 2H^{+}$$

(7) Migration of the electrons in the substrate surface

$$Ni^{++} + 2e^{-} \rightarrow Ni$$

$$2H^{+} + 2e^{-} \rightarrow H_2\uparrow$$

More recently, Feldstein and Lancsek [19] proposed a modified hydride mechanism. In this model, an intermediate species, a meta-phosphorous acid (HPO_2) is produced during the oxidation reaction. Also, this species is responsible for the production of elemental phosphorus or orthophosphorus acid (H_3PO_3). The basic steps occur in the course of reaction can be summed up in the following equations:

(8) $H_2PO_2^{-} + OH^{-}(\text{catalyst}) \rightarrow PO_2^{-} + H_2O + H^{-}(\text{catalyst})$

(9) $PO_2^{-} + OH^{-} \rightarrow HPO_3^{--}$

(10) $2H^{-}(\text{catalyst}) + Ni^{++} \rightarrow Ni + 2H(\text{catalyst})$

(11) $2H(\text{catalyst}) \rightarrow H_2\uparrow$

(12) $3H^-(\text{catalyst}) + 2H_2O + PO_2^- \rightarrow P + HOH^- + 3H(\text{catalyst})$

(13) $H^-(\text{catalyst}) + H_2O \rightarrow H_2\uparrow + OH^-$

(14) $H_2PO_2^- + OH^- \quad HPO_3^{--} + H_2\uparrow$

In this model, the rate of deposition is controlled by equation (8) and the co-deposited phosphorus results from equation (12). It is believed [19] that the above reactions occur in both acidic and alkaline nickel baths.

3. Electroless Cobalt Plating

Since the chemical nature of cobalt is quite similar to that of nickel, it is not surprising to find that the reactions occuring in the electroless cobalt bath are similar (if not identical) to those in the electroless nickel bath. The reactions can be tentatively expressed as [10]:

(15) $NaH_2PO_3 + Co^{++} + H_2O \rightarrow Co + 2H^+ + NaH_2PO_3$

(16) $3H_3Po_2 \rightarrow H_3PO_3 + 3H_2O + P$

(17) $NaH_2Po_2 + H_2O \rightarrow NaH_2Po_3 + H_2\uparrow$

As in the case of electroless nickel, the rate of deposition depends on the concentration of the reducing agent and the pH value of the metalizing bath.

(II) PRETREATMENT OF THE SUBSTRATES

1. Introduction

In electroless metal plating, a preparatory treatment of a non-conductor substrate surface is necessary. The function of this pretreatment process is to form a deposit of catalytic sites on the substrate. When the pretreated substrate is subsequently immersed in the metalizing bath, oxidization of metal ions to their metal form is initiated at these sites.

To date, the most widely used pretreatment processes consist of a two-step immersion system based upon the combination of tin and palladium. Specifically, the various available processes can be classified into two systems as follows:

(i) Sensitization step ($SnCl_2$/HCl) followed by an activation step ($PdCl_2$/HCl)

(ii) Catalyzation step ($SnCl_2$/$PdCl_2$/HCl) followed by an acceleration step (HCl or NaOH and similar)

In the following, a brief account of each system is given.

2. Conventional Sensitizer Solutions

The conventional sensitizer involves a two-step immersion sequence in acidic stannous chloride solution followed by an acidic palladium chloride solution. The first bath is often referred to as the "sensitizer" while the second the "activator". The function of

sensitizing is to adsorb a certain material on the substrate surface. The material is held to the substrate surface by either chemical or physical means. The nature of adsorption is not yet completely understood. It may be caused by any one or combination of the phenomena known as adsorption: physical adsorption, chemisorption, wetting or absorption. After sensitization the substrate must be rinsed to remove excess sensitizer from the surface. The activation step is to form catalytic sites on the substrate. A simple explanation [2,4,5,20,21] for the sensitization and activation mechanism is a redox reaction of the type:

$$(18)\quad Sn^{+2} + Pd^{+2} \rightarrow Pd + Sn^{+4}$$

in which the stannous ions reduce the palladium ions to their metallic form.

Recently, some doubts [3,22,23] have been raised against this simple explanation. We [3] found that u.v. light is effective in inhibiting the electroless deposition of copper, nickel and cobalt if applied after sensitization, and of nickel and cobalt after activation. We believe this is connected with the structural changes in the sensitizing and activating agents, and that the redox model is thus rather incomplete. A more detailed discussion on this aspect will be presented later. Feldstein and Weiner [22] in the study of an improved sensitizer (to be discussed next) found that the redox reaction is at best of 25% in efficiency on a Teflon surface. Also, the surface activity (Air II) of sensitized Teflon was not changed by subsequent immersion in the activation solution. They, therefore, suggested that ionic

palladium may still be present at the conclusion of the activation step. On the other hand, de Minjer and V. D. Boom [23] claimed that no metallic palladium is present after the sentizing and activating steps, but a tin-palladium complex, containing one palladium atom per two tin atoms, might be the material responsible for subsequent electroless deposition of nickel on glass substrate.

3. Improved Sensitizer Solution

In recent publications [19, 24-28], it has been demonstrated that the incorporation of stannic chloride solution, aged at room temperature for one week, to the conventional sensitizers resulted in a better uniformity of metallic coverage on hydrophobic or hydrophilic substrate surfaces. The aged stannic chloride solution may either be added to the conventional stannous chloride sensitizer or used in a separated step prior to immersion in conventional sensitizers. A suggested mechanism for the improvement is that the aged stannic component provides a new path for the adsorption of stannous ions at the interface. The result is the formation of a β-stannic acid, a polymeric substance of the type [27,29]:

$$(HO)_3 - Sn - [OSn - (OH)_2]_n - OH$$

or

$$(HO)_2 - Sn - [O_2Sn]_n - (OH)_2$$

where 'n' is an integer. It is the presence of this β-stannic acid and its interaction with stannous ions that accounts for the improvement in sensitizing performance.

3. Catalytic Solutions

The catalytic solution, which was first developed by Shipley [30], is produced by combining the tin chloride and palladium chloride in excess of hydrochloric acid to a dark brown solution. The making of the catalyst sol was believed [31,33] to be characterized by a two-step process. The first step is assumed to be the reduction of a palladium salt to palladium metal in colloidal form. It is then followed by the stabilization of the colloidal palladium. The stabilization is achieved by the addition of excess stannous salts which form a protective layer about the palladium metal particles. In order to activate the adsorbed catalyst, an additional step, termed acceleration [33] is required. The function of the acceleration step is to remove the protective layer and thus exposing an active palladium colloidal particle. On the other hand, it has been found [32] that in the tin-palladium chloride solution, a Pd-Sn complex was first formed and that the chemical mechanism that incorporated the tin in the colloid is presumably a redox reaction involving:

$$(19)\quad (Pd\text{-}Sn)\ \text{complex} \rightarrow (Sn\text{-}Pd)\ \text{alloy} + 2\ Sn^{+4}$$

However, Rantell and Holtzman [34] reported that the active component of the colloidal catalyst is a complex chloride of tin II and palladium II, and that metallic palladium is formed on an ABS substrate surface after post-acceleration rinse. The product of metallic palladium is believed to be due to a redox reaction (equation 18) occuring during the hydrolysis in the catalyst and the accelerator

treatment.

Tsukakara et.al. [35] reported that the substance which acts as an active site in the electroless deposition is the negatively charged palladium in a colloidal state with adsorbed tin II.

An extensive study of the catalytic solutions has been carried out in this laboratory. The results [36] will be discussed in the following chapters.

(III) ELECTRICAL CONDUCTION IN CONTINOUS METAL FILMS

1. Introduction

Electrical conduction in metals is due to the net drift of conduction electrons under the action of an external electric field. The general behavior of electrons in metals has been treated by various authors [37-39]. Several concepts are of importance in considering metal films. They are:

a) Resistivity ρ_o and the electron mean free path ℓ_o

Within the context of the free electron gas theory of Drude-Lorentz-Sommerfeld [37], the mean free path is related to the resistivity of bulk metal by the equation

$$\rho_o = m\bar{v}/ne^2\ell_o \qquad (20)$$

where m is the effective mass of the electron, $\bar{v}$ is the electron velocity at the Fermi surface, e is the electronic charge and n the density of conduction electrons given by

$$(21) \quad n = \frac{8\pi}{3} \left(\frac{\bar{mv}}{h}\right)^3$$

where h is Planck's constant.

In a perfect, rigid lattice, an electron can move freely without resistance. This can be seen in the Bloch scheme, for then the one electron functions, having the same amplitude at equivalent positions in each unit cell, have the form:

$$(22) \quad \psi_k = \chi_k(\bar{r}) \exp \cdot(2\pi i\, \bar{k} \cdot \bar{r})$$

where $\bar{r}$ is the position vector, $\chi_k(\bar{r})$ has the translational periodicity of the lattice, and $\bar{k}$ is the momentum vector. The velocity of an electron having a given energy $E(\bar{k})$ and a momentum $\bar{k}$ is

$$(23) \quad \bar{v}(\bar{k}) = \frac{1}{h} \operatorname{grad}_k E(\bar{k})$$

Thus, in the absence of any perturbation, an electron should continue in this state indefinitely.

An ordinary metal does not satisfy these ideal conditions because (i) its lattice is undergoing thermal vibration, and (ii) it usually contains imperfections, such as impurities and grain boundaries. Both these effects may cause scattering of electrons and thus shorten the mean free path.

b) Matthiessen's Rule

We consider the scattering of electrons by the geometrical defects and the thermal defects to be independent. If Q_r is the cross-section for scattering by geometrical imperfections, and N_r is the

density of imperfections, the mean free path ℓ_r for scattering by imperfect ions is given by:

$$(24)\quad 1/\ell_r = N_r Q_r \ .$$

Thus, according to equation (20), the residual resistivity ρ_r due to the geometrical imperfections is

$$(25)\quad \rho_r = m\bar{v}/ne^2\ell_r$$

which is temperature-independent.

On the other hand, the thermal vibration causes the instantaneous spacings of the atoms to be slightly irregular so that the electron waves experience some scattering. The thermal vibration is usually treated as standing waves, each of which can be resolved into two waves travelling in opposite directions. The energy contained in the waves is quantized and the quantum unit is called a phonon. If the mean free path for scattering by phonons be denoted by ℓ_T, then ℓ_T is proportional to the cross-section of a lattice atom. In turn, the cross-section is governed by the square of the mean amplitude of atomic vibrations and is thus proportional to the lattice energy. At temperatures sufficiently above the Debye temperature, it is inversely proportional to temperature. Hence, the resistivity due to thermal vibrations can be written in the form:

$$(26)\quad \rho_t = m\bar{v}/ne^2\ \ell_T(1/T)$$

which is linearly dependent on temperature.

Matthiessen's rule states that the total resistivity ρ_o may be considered as the sum of the residual resistivity and the thermal resistivity:

$$(27)\quad \rho_o = \frac{m\bar{v}}{ne^2}\left(\frac{1}{\ell_r} + CT\right)$$

where C is a proportionality constant.

This linear dependence of resistivity on temperature is a result which agrees with observed data for most metals at sufficiently high temperature.

c) Temperature Coefficient of Resistivity (T.C.R.)

The T.C.R. arises from the component CT in equation (27) and is defined for bulk metals as:

$$(28)\quad \alpha_o = \frac{1}{\rho_o}\frac{d\rho_o}{dT}$$

In most metals the temperature variation of the mean free path is the same as that of the resistivity, thus, we have

$$(29)\quad \alpha_o = \frac{1}{\ell_o}\frac{d\ell_o}{dT}.$$

It will be made clear that equation (29) provides a way for the study of the smoothness of thin film surfaces.

2. Size Effect

Conduction in continuous thin metal films can be considered in terms of the electron movement through the metal layer under the influence of an applied electric field. The electron flow is usually examined in a direction parallel to the plane of the film.

The surfaces are thought to behave as a sort of structure imperfection imposing a geometrical restriction on the motion of the conduction electrons. Due to those extra scattering centers, the mean

free path of the conduction electrons is shortened, thus increasing the resistivity. The scattering at the surface can be considered to be either as

i) Diffuse scattering in which the electron momentum parallel to the surface changes after collision, or as

ii) Specular scattering in which there is no changes in the electron momentum parallel to the surface after collision

The idea of diffuse scattering was first suggested by Thomson [40]. He considered a film defined, as shown in Fig. 1 with

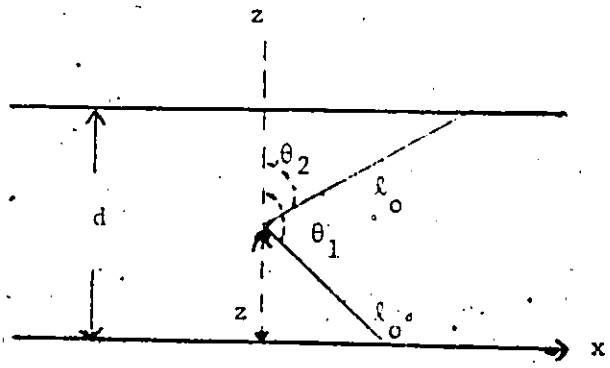

Fig. 1: The effect of surface scattering on the mean free path ℓ_o

thickness d, but of infinite extent in the other two dimensions. He then calculated the mean value of all the possible free paths of an electron incident at any angle θ to and starting a distance Z from the surface and arrived at a formula for the conductivity of a thin metal film relative to the bulk given by:

$$(30)\quad \frac{\sigma}{\sigma_o} = \frac{3k}{4} + \frac{k}{2}\ln\frac{1}{k}$$

where $\sigma = 1/\rho$ is the conductivity of the thin metal film, k is the ratio of the thickness d to the mean free path ℓ_o in the bulk.

This approach, however, ignores the statistical distribution of electron free paths about the mean free path of the bulk. The proper approach was subsequently studied by Fuchs [41].

By using the Boltzman transport equation and assuming a spherical Fermi surface, an isotropic electron mean free path and diffuse scattering of the electrons at the film surface, he obtained an expression:

$$(31)\quad \frac{\sigma}{\sigma_o} = 1 - \frac{3}{8k} + \frac{3k}{4}\left(1-\frac{k^2}{12}\right)E_1(k) + \left(\frac{3}{8k} - \frac{5}{8} - \frac{k}{16} + \frac{k^2}{16}\right)e^{-k}$$

where $E_1(k) = \int_k^\infty \frac{e^{-x}}{x}\,dx$

for the film conductivity.

If k is either much greater or much less than unity, equation (31) can be simplified to:

$$(32)\quad \frac{\sigma}{\sigma_o} = 1 - 3/8k \qquad \text{for } k \gg 1$$

$$(33)\quad \frac{\sigma}{\sigma_o} = \frac{3k}{4}\ln\frac{1}{k} \qquad \text{for } k \ll 1$$

In 1952, Sondheimer [42] modified Fuch's result by introducing a reflection parameter P at the surface boundaries. The reflection parameter is defined as the probability that an electron will be specularly reflected upon scattering from a film surface, and takes

on values from zero to one. The equation for the conductivity ratio is then given by:

$$(34)\quad \frac{\sigma}{\sigma_o} = 1 - \frac{3}{2k}(1-p)\int_1^\infty \left(\frac{1}{t^3} - \frac{1}{t^5}\right)\frac{1-e^{-kt}}{1-pe^{-kt}}\,dt$$

with $t = 1/\cos\theta$, where θ is the polar angle of the polar-coordinate (V,θ,ϕ) in the velocity space.

It is easily seen that equation (34) reduces to equation (31) by putting $P = 0$, and becomes unity if $P = 1$, that is, the surface has no effect at all on the behavior of the electrons.

The limiting case of either large k or small k is:

$$(35)\quad \frac{\sigma}{\sigma_o} = 1 - \frac{3(1-P)}{8k} \quad \text{for } k >> 1$$

$$(36)\quad \frac{\sigma}{\sigma_o} = \frac{3k}{4}\frac{(1+P)}{1-P}\left(\ln\frac{1}{k} + 0.4228\right) \quad \text{for } k << 1$$

The detailed derivations of equations (31) and (34) are given in Appendix (A)

Note that equation (36) is valid only for $P<<1$. The theoretical variation of the resitivity of a thin metal film as a function of both k and p have been calculated by Sondheimer [42], Brandi and Cotti [43], Chopra [44] and Campbell [45], and is reproduced here for several values of P as shown in Fig. 2. The solid curves are given by equation (34) whilst, the dotted curves are calculated from limiting equation (35). The equations are more conveniently plotted as resistivity ratios rather than the conductivity ratios to enable details at low k-value to be separated. A comparison of the two sets of curves shows that the

approximation is sufficiently accurate for the k-value to be as low as 0.1.

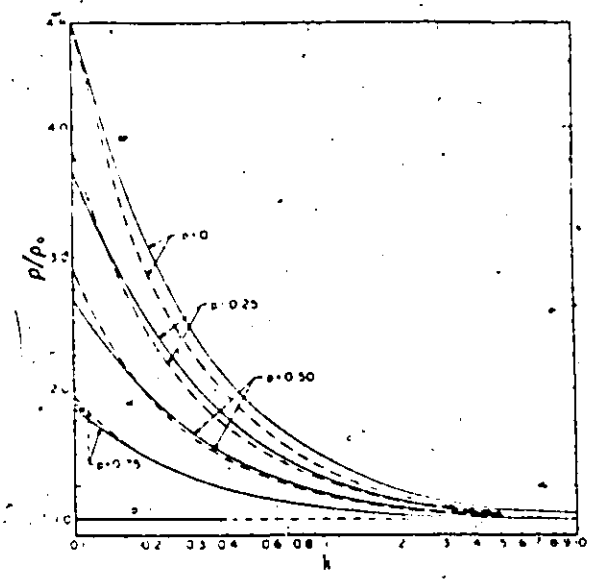

Fig. 2 Theoretical variation of the film-to-bulk resistivity ratio with normalized thickness $k = d/\ell_0$ for several values of scattering parameters

It must be pointed out that the Fuchs-Sondheimer theory only applies to single crystal, plane parallel films and to isotropic materials. Nevertheless, many workers have applied the theory to polycrystalline films. Most of them assume the bulk resistivity and the mean free path to be thickness independent, and fit the resistivity data to equation(34) by adjusting the specular parameter P. The normal analysis always led to the conclusion that p = o for polycrystalline films.

Recently, it has been shown that for a polycrystalline film, the average grain diameter is about equal to the film thickness [46-48]. In this case, the contribution to the total resistivity by grain boundary

scattering is significant. Mayadas and Shatzkes [49] have proposed a model for the interpretation of the electical resitivity of polycrystalline films. They assumed that the grain boundaries can be represented by a series of partially reflecting planes randomly spaced according to a gaussian distribution and that the grain boundary potential can be represented by a δ-function potential. Among those planes, only those perpendicular to the applied electric field cause an extra electron scattering, which results in an increase in resistivity. The grain boundary resitivity is then calculated by solving the Boltzman transport equation. In the presence of the size effect, the total resitivity is obtained by following the Fuchs-Sondheimer calculation. The authors concluded that the resistivity of a film in which significant grain boundary scattering is present decreases more rapidly as thickness increases than the Fuch-Sondheimer theory predicts. This is due to the fact that the average grain size is approximately equal to film thickness, so that as the latter increases, the contribution from grain boundary scattering decreases.

Several good review articles on this subject can be found in recent literatures[44, 50-52].

3. Matthiessen's Rule

In case of a thin film, it is possible to rewrite the Matthiessen rule as

$$\rho_f = \rho_o + \rho_p + \rho_b \qquad (40)$$

where ρ_b is the resistivity value due to the effect of the boundary on the mean free path, ρ_p is the resistivity caused by the method of preparation and is independent of temperature.

Deviation from Matthiessen's rule has been found to become increasingly large as the film thickness decreases [53-59]. This is due to the fact that the effect of surface scattering cannot in general be represented by a simple additive term in the resistivity. Hence, Mattheissen's rule is only valid for fairly thick films.

4. Temperature Coefficient of Resistivity

By using the resistivity ratio for the limiting cases of very thick and very thin films, we can conveniently calculate the T.C.R. of metal films. They are given by:

$$(41)\quad \frac{\alpha_f}{\alpha_o} = 1 - \frac{3(1-P)}{8k} \quad \text{for } k > 1$$

$$(42)\quad \frac{\alpha_f}{\alpha_o} = 1/\ln(1/k) \quad \text{for } k \ll 1, \; k < 1$$

Note that equation (42) is independent of P only if P is very small. The prediction of these equations is that the T.C.R. of the film will be suppressed below that of the bulk film material approximately the same order as the resistivity.

Now from equation (40), we can write:

$$(43)\quad \frac{d\rho_f}{dT} = \frac{d\rho_o}{dT} + \frac{d\rho_b}{dT}$$

which in the limiting case of very thick film reduces to:

$$(44)\quad \alpha_f \rho_f = \alpha_o \rho_o = \text{constant}$$

The importance of equation (44) is that it provides a good method for the determination of the mean free path since α_o is related to the mean free path through equation (29). But the value of the specular parameter cannot be deduced from these equations because the size effect is insensitive to the specular parameter for thick films.

Even though T.C.R. should decrease with decreasing film thickness, one should never expect the T.C.R. of a continuous thin metal film to become negative, no matter how thin the film might be, instead, it should approach zero according to equation (42).

(IV) Electrical Conduction of Discontinuous Thin Metal Films

1. Introduction

As the thickness of a metal film is reduced, a striking change in conduction behavior takes place. First of all, the resistivity increases abruptly to values many orders of magnitude higher than the bulk resistivity; secondly, the temperature coefficient of resistivity becomes negative. This sudden change in resistivity is much too large to be explained by the reduction of the electron mean free path. Electron microscopy has revealed an island structure for metal films possessing this abnormal behavior, thus it is believed that electrons transferred from island to island result in the measured high resistivity. Furthermore, the negative temperature coefficient of resistivity suggests that the electron transfer process is an activated one. There are many ways in which this activated process can occur. In what

follows, we shall consider some of the most important ones.

2. Thermionic Emission

In this model, one assumes that only those electrons which have an energy of at least the maximum barrier height, can be transferred to a neighboring island. The maximum barrier height equals the metal-insulator work function minus the effect due to the image force between the islands. This is so because when the island separation is small, the image force potentials overlap, hence reducing the barrier height. Based on those ideas, Minn [60] derived the following expression for the conductivity of a discontinuous metal film:

$$(45)\quad \sigma_f = \frac{AeT}{k}\gamma \exp\left(-\frac{\Psi - Be^2/r}{kT}\right)$$

where Ψ is the work function of the bulk metal, r the average distance between islands, A and B are constants characteristic of each film, and k is the Boltzman constant.

The term Be^2/r represents the effect of the image force. This takes on a value of several electron volts if r is sufficiently small, say about several Å. For low applied field, the activation energy equals the barrier height and the current depends exponentially on the barrier height. Since the activation energy measured experimentally is much smaller, however, than the barrier height, it has been postulated that a small island might have a lower work function than that of a bulk material. Also, the shape of a small island might reduce its work function. Nonetheless, this model has been rejected recently by most

investigators [61-63] except one [64].

3. Quantum Mechanical Tunneling

There are two ways in which electron transfer by quantum mechanical tunneling can occur. One way is the electron tunneling from island to island through the free space that separates them. The other is the substrate assisted tunneling. We will consider the two mechanisms separately.

A) Tunneling via free space

It is well known, however, that tunneling is a relatively temperature independent process [65]. The major problem in analyzing the conduction mechanism in discontinuous thin metal films lies in reconciling the temperature dependence observed experimentally. Corter [66] and Dermois [67] introduced a thermally-activated term in the tunneling mechanism. They proposed that an electron must first be thermally activated to a certain energy level before it can tunnel from island to island. The activation energy for conduction was taken as the energy required to transfer charge from one initially neutral island to another one some distance removed. This energy is of order of magnitude:

$$\epsilon = e^2/\kappa d \qquad (46)$$

where d is the average linear dimension of the islands and κ is the dielectric constant, which in practice is assumed to be somewhere between that of the substrate and vacuum. Only electrons or holes excited to

states of at least this energy from the Fermi level will be able to tunnel from one neutral island to another. This process is thus an activated one. On the other hand, the transfer of charge from a charged island to a neutral one is not activated because it does not lead to a net increase of the energy of the system [61]. Based on these ideas, the tunneling model proposed by Nuegebauer and Webb [61] which consists of a few islands charged by thermal activation with an electron on the charged island tunneling under the influence of the applied electric field to the next neutral island, gives the conductivity:

$$(47)\ \sigma_f \propto \frac{r^2 e^2}{d} \frac{\sqrt{2m\phi}}{h^2 \alpha} \exp\left(\frac{4\pi r\sqrt{2m\phi}}{h}\right) \exp\left(\frac{-e^2/\kappa d}{kT}\right) \Omega^{-1}\text{cm}^{-1}$$

where ϕ is the potential barrier between islands which can be approximated by the work function of the metal.

The relative Fermi level of neighboring islands in an applied field is illustrated in Fig. 3.

Equation (47) predicts that the conductivity of a discontinous metal film is ohmic and depends exponentially on island size and reciprocally on temperature.

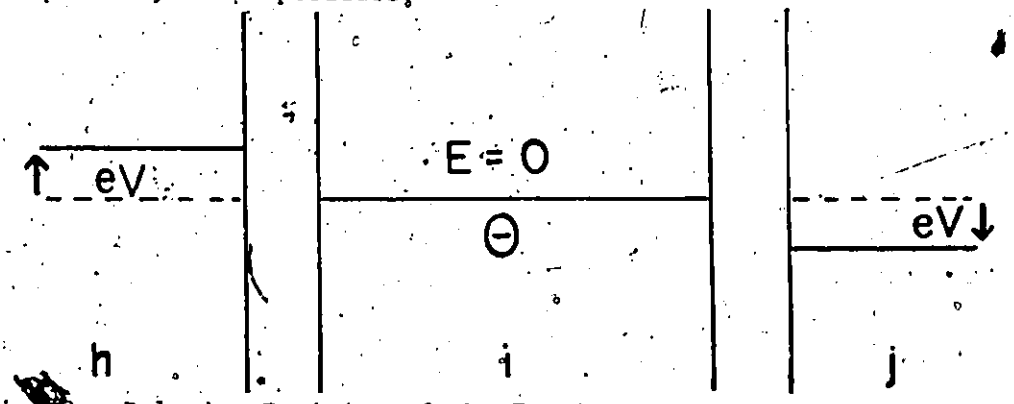

Fig. 3. Relative Position of the Fermi Levels of Neighbouring Islands

It should be noted that the activation energy; equation (46), is the energy required to remove an electron to infinity, but to transfer the electron to a distance r, the energy required is less and given by

$$(48) \quad \epsilon = e^2/\kappa d - e^2/\kappa\,(r-d)$$

If now an electric field E is applied, it has been shown [61], that the activation energy is further reduced to:

$$(49) \quad \epsilon = \frac{e^2}{\kappa d} - \frac{2e^3/2E^{1/2}}{\kappa} + \delta\epsilon$$

Because of an appreciable reduction in activation energy, it is not surprising to see that the conductivity becomes non-ohmic at high fields. Physically, the last term in equation (49) means that at high fields, the electrons are transferred faster than they are thermally created.

Recently, Sheng et.al. [68-69] proposed a field-induced tunneling model in discontinuous metal films at low temperature and high field regime. Since at low temperature, the density of thermal-activated charged carriers is negligible, however, in high field regime when the voltage drop between neighboring islands is much larger than kT/e, the majority of charge carriers are created by field-induced tunneling between neutral islands.

A point of interest here is that in the study of the magnetic properties of granular nickel films, Gittleman et.al. [70] reported that electron tunneling probability is spin dependent.

B) Substrate-assisted Tunneling

The substrate-assisted tunneling was first suggested by Hill [71-73]. The process is essentially a low-field hopping conduction for dielectrics [74-76]. Hill noted that the potential height for substrate-assisted tunneling is the work function of the metal minus the energy of the conduction band in the substrate relative to the vacuum level. The second term can be of the order of 2-3 eV. The transmission coefficient is greatly enhanced, and therefore favours tunneling through the substrate. The transfer of an electron can be pictured as follows: the electron from island i which tunnels into trap A in the dielectric substrate is thermally activated to the trap B of the next highest energy in the substrate, from which it can now tunnel into island j. Figure 4 shows an energy level diagram for substrate-assisted tunneling.

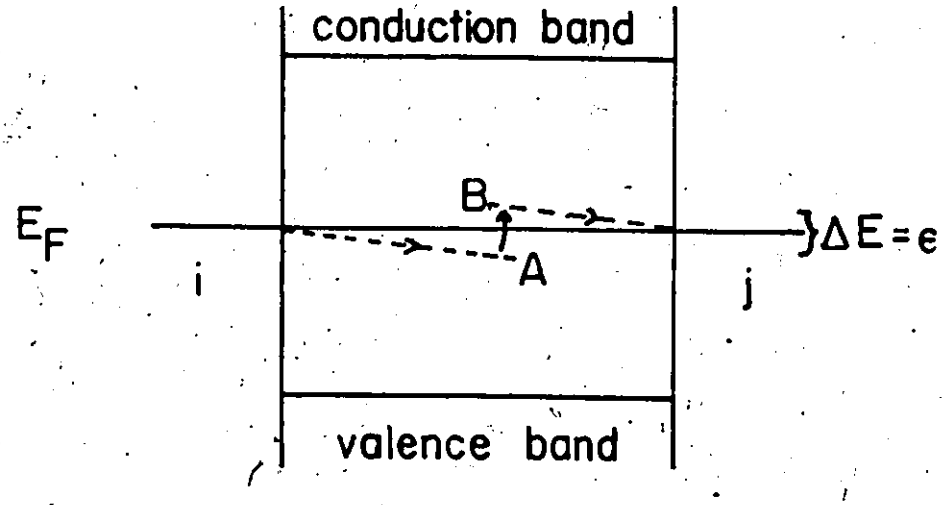

Fig. 4.. Energy diagram for substrate-assisted tunneling.

Neglecting the intrinsic resistance of the metal island, the current density is given by:

$$(50)\quad J(V,T) = \frac{8\pi me}{h^3B^2} \sinh\left(\frac{eV}{kT}\right) \frac{\pi BkT}{\sin\pi BkT} \exp\cdot(A\phi^{1/2}) \exp(-\varepsilon/kT)$$

where ϕ is the average barrier height, A and B are constant characteristics of each film.

Qualitatively, it can be seen that equation (50) describes a process in which the temperature dependence is modified by the quantum mechanical tunneling term $\pi BkT/\sin\pi BkT$. At low field, equation (50) also predicts an ohmic behaviour of conductivity.

Substrate-assisted tunneling can also occur via the stable energy states created by impurities [76] and/or traps [63,77] or even by field injection [78].

In conclusion, it appears that the Neugebauer and Webb model [61] satisfies the qualitative observations for films with smaller island size, while Hill's model represents an explanation for the films with large island films. Thermionic emission predominates for films with small island size and large island separation. Fig. 5 illustrates the various regions of island size and separation at which the proposed conduction mechanisms are most applicable [79].

4. Temperature Coefficient of Resistivity

Whatever the details of the conduction mechanisms involved in discontinuous metal films, exp (-ε/kT) is by far the most significant

temperature dependent term in the conductivity equations, hence, by definition, the T.C.R. of a discontinous metal film is given by:

$$(51)\quad \alpha_f = -\varepsilon/kT^2$$

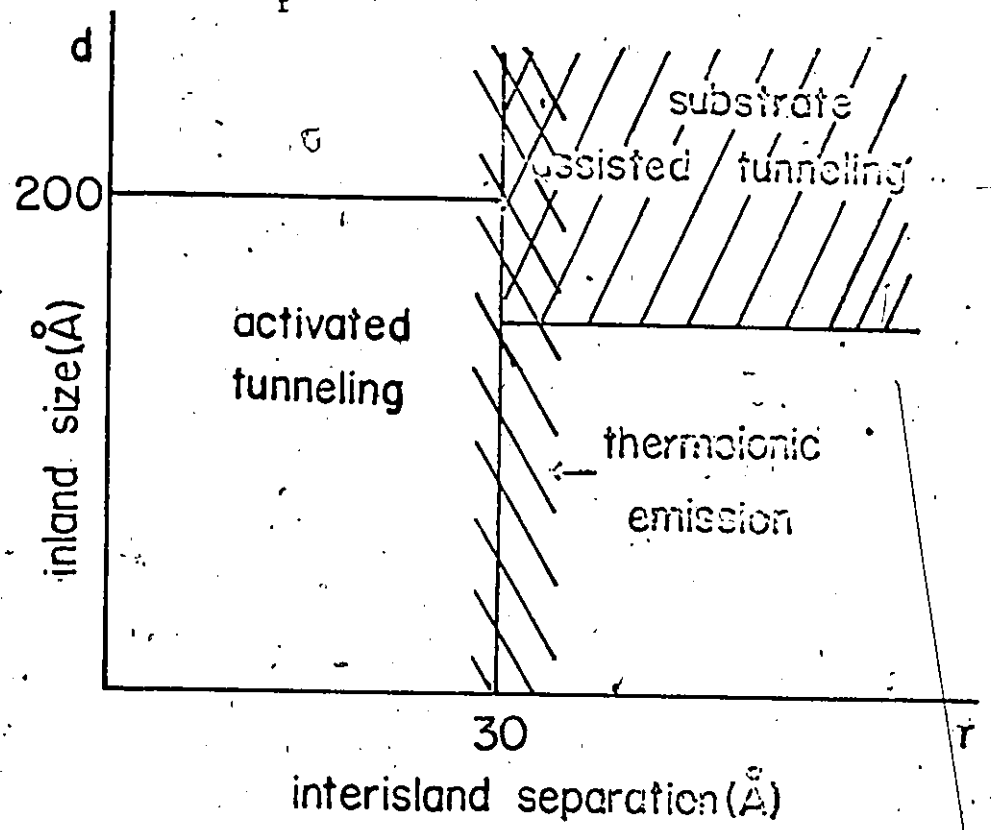

Fig. 5. Regions of island size and separation at which the proposed conduction mechanisms are most applicable.

which implies that the T.C.R. of a discontinuous metal film is negative. It is, however, not impossible to obtain a positive T.C.R. for discontinuous metal films [80]. In fact, the exact behavior of T.C.R. depends on the details of the film structure. For example, a film consisting of large islands and small interisland separations may have a positive T.C.R., because the intrinsic resistance of the metal islands is no longer negligible. Hill [72] has classified several types of discontinuous metal films according to island size and interisland separation as outlined in Table I.

TABLE I

Classification of Discontinuous Metal Films According to Hill (Ref. 72).

Type of film	Island size	Interisland spacing	Predominant type of conduction	Activation energy	T.C.R.
I	small	small	activated tunneling	large	negative
II	small	large	substrate-assisted thermionic emission	small	negative
III	large	small	substrate-assisted tunneling	small	negative or positive
IV	large	large	thermionic emission	small	negative or positive

(V) Hall Effects of Continuous Thin Metal Films

1. Introduction

When a current-carrying material is placed in a magnetic field perpendicular to the direction of the current, as shown in Fig. 6, the electrons will be subjected to a Lorentz force under the influence of the magnetic field, such that the lower surface collects a negative charge, the upper surface a positive charge. Ultimately, a stationary

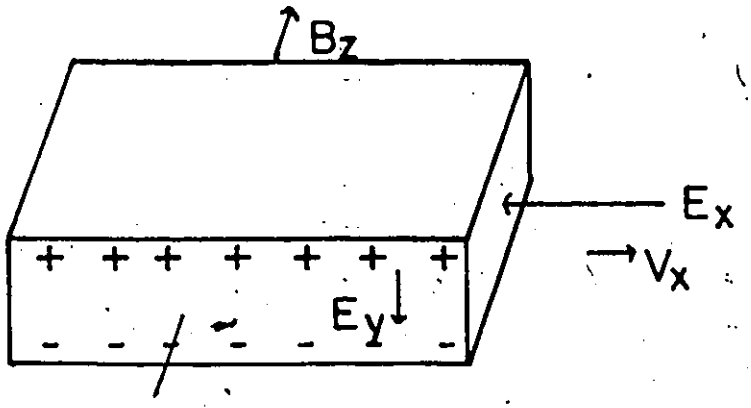

Fig. 6. Illustration of the Hall effect produced by an electric field E_x and a magnetic field B_z perpendicular to the front face.

state is obtained in that the current along the Y-direction vanishes and a field, called the Hall field [81] is set up. If the charge carrier is positive, the Hall field is reversed. Thus a measurement of the "Hall voltage" in the Y-direction gives information about the sign of the charge carrier.

The Hall coefficient R_H is usually defined by:

$$(52) \quad R_H = E_y/B_z J_x$$

where R_H is given in cm^2/amp-sec, if J_x, the current density is in amp/cm^2, E_y the Hall field in volt/cm and B_z the applied magnetic field in V-sec/cm. When the Hall coefficient is combined with electrical resistivty, we obtain the Hall mobility μ_H which is defined by:

$$(53) \quad \mu_H = R_H/\rho$$

According to the theory of two-band conductivity [38,42], the current in the transition metals is carried by s electrons, with

effective mass not very much different from that of a free electron. On the other hand, the resistance is mainly due to the scattering processes in which the electron makes a transition from the s- to the d-band. The probability of such a transition is proportional to the density of states in the d-band. Since the density of states is proportional to the cube root of the number of particles in the d-band, the conductivity σ is, therefore, proportional to

$$(54)\quad \sigma\alpha \frac{\#\text{ of electrons in s-band}}{(\#\text{ of holes in d-band})^3}$$

and the Hall coefficient is actually defined by:

$$(55)\quad R_H = -\frac{1}{eN}\left(\frac{\sigma_s^2}{n_s} - \frac{\sigma_d^2}{n_d}\right)$$

where $\sigma = \sigma_s + \sigma_d$, n_s and n_d are the number of electrons per atom in the 4s-band and the number of holes in the 3d-band respectively. N is the number of atoms per cm^3.

The conductivity of transition metals due to the holes is thought [39] to be negligible in comparison with that due to the electrons. The Hall coefficient is thus given almost entirely by electrons in the s-band, the holes in the d-band making essentially no contribution.

2. Hall Effect of Ferromagnetic Materials

The foregoing definition of Hall coefficient is defined for non-ferromagnetic material. The observed behavior for a ferromagnetic material however, shows a quite different typical behavior, such as that shown in Fig. 7 and is given by the phenomenological relation [82].

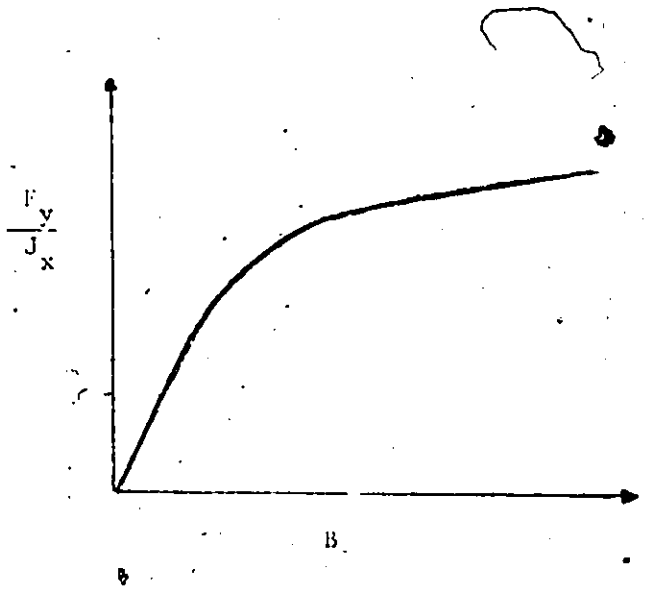

Fig. 7. Schematic behavior of Hall resistivity E_y/J_x as a function of applied magnetic field B for a ferromagnetic metal.

$$(56)\quad \frac{E_y}{J_x} = R_o H + R_1 M$$

where H is the magnetizing force in the z-direction, M is the magnetization in the z-direction, R_o and R_1 are often referred to as the ordinary and the extraordinary Hall coefficient respectively.

The magnetization, magnetizing force and the applied magnetic field are related by the expression:

$$(57)\quad H = B - 4\pi M$$

Above saturation, the magnetization has a constant value, thus in this range of field, equation (56) becomes

$$(58)\quad \frac{E_y(B)}{J_x} = R_o B + (R_1 - 4\pi R_o)M$$

Below saturation, $B = 4\pi M$, hence we have

$$(59)\quad \frac{E_y(B)}{J_x} = \frac{R_1}{4\pi} B$$

Thus, the slope of Hall voltage vs applied magnetic field below

saturation field determines the extra-ordinary Hall coefficient, and the ordinary Hall coefficient can be obtained from the intercept of $E_y(o)$ of equation (58).

3. Size Effect

In small applied magnetic field, the size effect of the Hall coefficient has been investigated by Sondheimer [83].

Under the combined action of the applied electric field and magnetic field, the distribution function, f, in the steady state is determined by the Boltzman transport equation (see also equation A-1).

$$(60) \quad -\frac{2\pi e}{h}\left(\bar{E} + \frac{1}{c}\bar{v} \times \bar{B}\right) \text{grad}_p f + \bar{v}\,\text{grad}_r f = -(f-fo)/\tau$$

The general solution of equation (60) subjected to the surface boundary conditions (see also equations A-5 and A-6) yields

$$(61) \quad \frac{R_{H-F}}{R_{H-B}} = \text{Im}\ \phi_p(s)/\beta$$

where

$$\frac{1}{\phi_p(s)} = \frac{1}{s} - \frac{3(1-p)}{2s^2}\int_1^\infty \left(\frac{1}{t^3} - \frac{1}{t^5}\right)\frac{1-e^{-st}}{1-pe^{-st}}\,dt$$

$$s = k + i\beta$$

$$\beta = d/r$$

and $r = mvc/e_\beta$ being the radius of the circular orbit of an electron in a magnetic field.

In the limiting cases of very thick and very thin films, equation (61) can be approximated to:

(62) $R_{H-F} = R_{H-B} \qquad k > 1$

(63) $R_{H-F} = R_{H-B} \frac{4}{3} \frac{1-p}{1+p} \cdot \frac{1}{k(\ln\frac{1}{k})^2} \qquad k << 1$

Similarly, the Hall mobility can be obtained by combining equations (35) and (62), (36) and (63)

(64) $\mu_{H-F} = \mu_{H-B}/(1 + (\frac{3(1-p)}{8k}) \qquad k > 1$

(65) $\mu_{H-F} = \mu_{H-B}/\ln(1/k) \qquad k << 1$

The theoretical variation of R_{H-F} and μ_{H-F} vs k are shown in Fig. 8 for various values of P. For k > 1, size effects are evidently

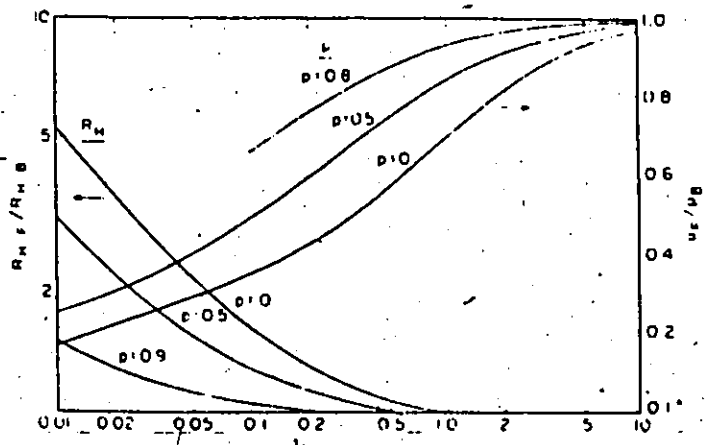

Fig. 8. Theoretical variation of μ_F/μ_B and R_{H-F}/R_{H-B} vs $K = d/\ell_o$ for several values of scattering parameters.

more pronounced in μ_{H-F} than in R_{H-F}.

If the effect of grain boundary scattering is taken into account, it has been shown [84] that relatively weak scattering from grain boundary results in a smaller increase in R_{H-F} and a much sharper decreas in

μ_{Li-F} with decreasing film thickness than would be expected from the Sondheimer theory.

CHAPTER 2

EXPERIMENTAL TECHNIQUES

(I) Electroless Deposition Procedures

1. Preparation and Cleaning of Substrates

The substrate chosen to receive an electroless deposition has to be smooth or flat and thermally stable. Even though Mylar and Kapton have been used widely in the past, "process clean" microscope slide glass was chosen for the present experiments. In addition, Formvar was used as the supporting film for studies employing the electron microscope. The selection of Formvar was based upon the following considerations. Firstly, according to Sennett and Scott [85], there is no difference in structure between vacuum deposited metal films, whether they were deposited on Formvar or on glass. Secondly, it is highly transparent to electrons and possesses adequate strength to sustain electron bombardment. Last, but not the least, is the possibility of floating the Formvar off the glass in distilled water (see specimen preparation).

Formvar films were obtained by placing a microslide glass into a solution made up of 4 grams of polyvinylformal in one litre of ethylene dichloride and leting the Formvar solution run down, finally picking up the glass and allowing to dry at room temperature.

The first step in conditioning the surface of a substrate is to clean it. A chemical cleaning method was chosen. After the "process

clean" microslide glass was wiped mechanically with Kimwipe wipers, it was cleaned in a two-step process. First, in a chromic sulfuric acid solution for about ten minutes at about 75°C; then in a warm solution of .10 N NaOH. After each step, the glass was rinsed thoroughly in distilled water. The chromic sulfuric acid solution used was made of 200 grams of chromic acid, 75 ml. of concentrated sulfuric acid, and 400 ml. of distilled water. For Formvar deposition, no cleaning process for the glass is required.

The cleaning process was always performed immediately prior to the pre-treatment and deposition of the electroless thin metal films.

2. Preparation of Pretreatment Solutions

In the present studies, three different pretreatment baths were used. Namely: (i) conventional, (ii) conventional with improved sensitizer, and (iii) catalytic.

Table II gives the composition of the conventional sensitizer solutions [6].

The presensitizing solution for the improved bath was 0.5 stannic chloride aged in air for about one week at room temperature. The working solution was made by 1:100 dilution using distilled water.

For the catalytic bath, a commercial solution was employed along with the accelerator solution recommended by the supplier [80]. The solutions were diluted as recommended and are given in Table III.

TABLE II

Composition of Conventional Sensitizer [6]

	stock solution	working solution
sensitizer	10 gm. $SnCl_2$ 10 ml. conc. HCl	1 ml. of stock solution in about 400 c.c. distilled water
activator	10 gm. $SnCl_2$ 10 ml. conc. HCl topped up to 100 ml with distilled water	1 ml. of stock solution in about 400 c.c. distilled water

TABLE III

Dilution of Catalytic Solution

	stock solution	working solution
catalyzer	Shipley 9 F	Mix 5 parts of diluted water and 2 parts of conc. HCl. Add 2 parts of 9 F
accelerator	Shipley 19 F	Mix 1 part of 19 F with 5 parts of distilled water.

3. Preparation of the Metalization Baths

The compositions of the metalizing solutions for the deposition of electroless nickel are given in Table IV, along with the compositions of the solution used for cobalt films and mixed nickel-cobalt films (with 65% nickel). The pH value of the alkaline metalizing solutions was adjusted with NaOh. The pH value of the acidic electroless nickel solution is 5.3.

TABLE IV

Composition of Metalization Baths(a)

	Acidic Ni-P	Alkaline* Ni-P	Alkaline* Co-P	Alkaline* Ni-Co-P
Nickel Sulfate	29.1	30.0		30.0(b)
Cobalt Sulfate			25.0	30.0
Sodium Hypophosphite	17.5	10.6	5 - 40	20.0
Succinic Acid Desodium Salt	14.9			
Succinic Acid	1.3			
Sodium Citrate		10.0	35.0	
Ammonium Sulfate			70.0	50.0
Ammonium Chloride		53.6		
Rochelle Salt				20.0

(a) All weights are in grams per litre

* pH adjusted with NaOH

(b) Ref. A. Brenner, in "Modern Electroplating" (F.A. Lowenheim Ed.)., p. 700, Wiley, N. Y. (1963).

In all cases, the solutions were freshly prepared and used at room temperature, unless stated otherwise.

All chemicals were reagent grade supplied by Canlab or Fisher and were used without further purification.

4. Specimen Preparation

The general procedure adopted for the electroless plating can be summarized by the following sequence : sensitizing (catalyzing), rinse, activating (accelerating), rinse and then finally metalizing.

An immersion time of 1-2 minutes was used in both the sensitizing (catalyzing) and activating (accelerating) steps, with a half-minute rinse in distilled water after each step. In the case of the improved sensitizer, an additional immersion time of one minute in the presensitizing solution was used prior to the usual procedures. The pretreated substrates were then immersed in the metalization baths for the subsequent deposition of thin metal films.

Transmission electron microscopy requires the specimen thickness to be in the range 100-1000 Å. Electroless thin metal films were first deposited on Formvar coated glass. After drying, the Formvar layers were cut at the edge of the glasswhich was then lowered slowly into a dish of distilled water at a shallow angle to float the Formvar off onto the water surface as shown in Fig. 9(a). Next, a clean microslide glass with a number of copper fine mesh grids on it was immersed into the dish, manoeuvered under the Formvar, then lifted out of the water

carrying the grids and films, as shown in Fig. 9(b), and let dry at room temperature.

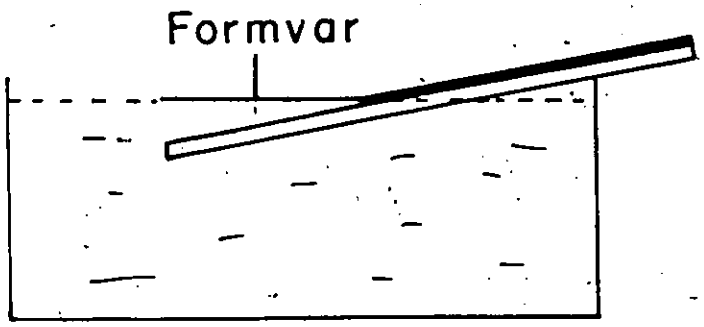

Fig. 9(a). Preparation of Formvar substrate - Floating off from glass

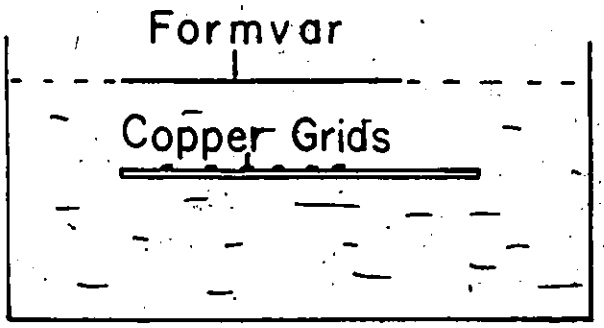

(b) Pick up by copper grids

For electrical resistivity and Hall effect measurements, the electrolessly deposited microslide glass was first cut into half. Each of them was placed in a specially made mask employing O-rings, then etched in a solution containing equal parts of concentrated HCl and HNO_3 acids diluted with water, to give a circular sample. Fig. 10 shows the dimension of the sample as well as the five electrode contact points (see below).

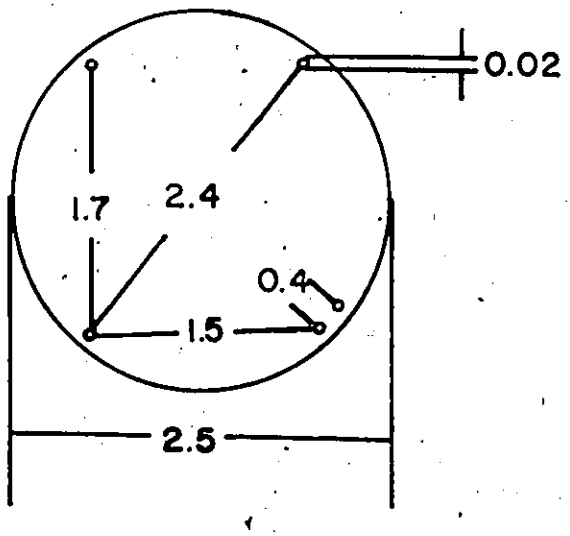

Fig. 10. Dimensions of the sample and the five probes contact configuration. (Unit in cm.)

When Formvar coated glass was used in electrical measurements, stable electrical contacts to the film were made with silver paint at the five electrode contacts.

5. Ultraviolet Light Irradiation

In investigating the effect of u.v. irradiation on the metal deposition, Formvar coated glass substrates were immersed in the sensitizing (or sensitizing and activating) solutions, and then irradiated, on one side only, with u.v. light. The opacity of the glass prevented irradiation of the other side. Continuation of the deposition process resulted in normal deposition on the non-irradiated side, showing that any inhibition of deposition on the other side was directly due to the

irradiation.

The u.v. irradiation was carried out using an Orel 50 W mercury lamp at a distance of about 5 cm. from the sample.

(II) Electron Microscopy

1. Introduction

The ability of an electron microscope to resolve extremely fine particles is based on the fact that electrons, rather than light, are used to illuminate the specimen. This is done because the shorter the wave length of the illuminating beam, the smaller the particles that can be resolved.

The fundamental difference between the electron microscope and an optical microscope are (i) electrons, which are emitted by a Tungsten wire filament heated to white heat, replacing light as a source of illumination, and (ii) magnetic fields acting on the moving electrons simulating the focussing action of a glass lens on light rays [87, 88].

Of the various electron microscopes, transmission electron microscope is by far the most important in the investigation of the nucleation and growth of thin metal films.

2. Elements of Transmission Electron Microscope

In general, a transmission electron microscope consists of three main systems. They are:

i) Illuminating System:

a) Electrongun - Electrons, emitted by the heated filament, E as shown in Fig. 11,

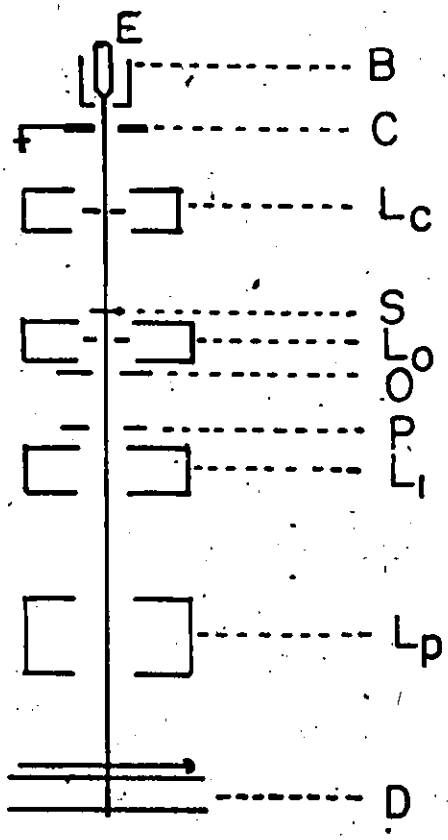

Fig. 11.
Schematic elements of transmission electron microscope.

are accelerated to a high velocity by a negative potential at B. The instrument from C to D is grounded. The electrons can be accelerated at 25 kv, 50 kv, 75 kv, 100 kv or 125 kv. In the present investigation, the transmission electron microscope was always operated at 100 kv unless stated otherwise.

b) Condenser lens - The basic function of the condenser lens (L_c) is to provide the proper intensity of the electron beam on the specimen(S). The first condenser lens produces a demagnified image of the source and the second one images the demagnified source onto the specimen. This arrangement reduces greatly the area of illumination and the total energy flux on the specimen.

ii) Image system:

c) Objective lens - Electrons leaving the specimen are focused by the objective lens (L_o) in the image plane. It forms the primary magnification of the illuminated portion of the specimen, and also determines the resolving power, the image contrast and the aberration of the electron microscope.

d) Objective aperture - The objective aperture (o) is located at the 2nd focal plane of the objective lens. Its role is to provide contrast in a microscope image and the selection of a medium quality dark field micrograph by stopping electrons scattered above a certain angle with little risk of being hit by the non-scattered beam.

e) The Selecting aperture - This aperture (p) limits the field of view of the specimen and thereby enables a "selected" area diffraction pattern to be taken.

f) Intermediate and Projector Lenses - The intermediate (L_1) and projector lenses (L_p) are used to produce the objective image of relatively large area with rays of relatively small aperture on the screen.

iii) Image Recording System:

The image recording system usually consists of a fluorescent screen and a photographic chamber where photographic negatives of the specimen images can be taken.

A more detailed description of electron microscope can be found in a number of texts [87-91].

3. Bright and Dark Field Microscopy

Quantitatively speaking, contrast in the electron microscopy image arise primarily from differential loss of electrons by scattering at individual object points. The variation in thickness of the specimen produces corresponding gradation in intensity of the transmitted electron beams, so that hills and valleys on the original surface are made to appear as regimes of dark and light contrast on the fluorescent screen.

A bright field image results if mainly the unscattered electron beam is used for the image formation. A dark field image is produced by intercepting the transmitted electron beam and allowing only scattered electrons to reach the image plane. This may be accomplished by either tilting the condenser lens or shifting the objective aperture, as shown in Fig. 12.

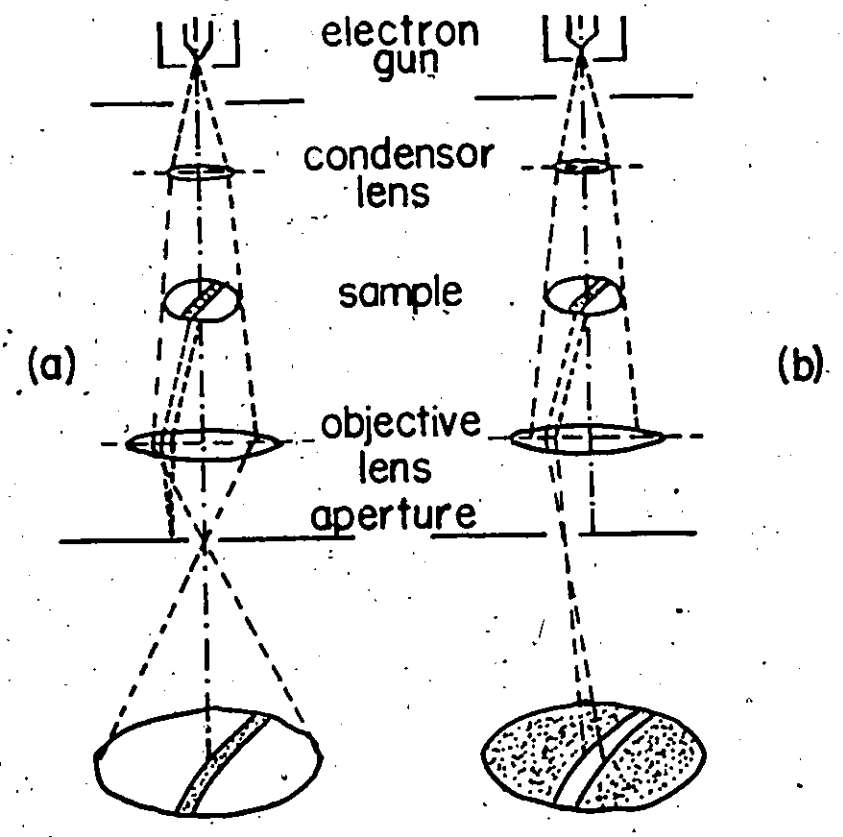

Fig. 12. Schematic of (a) bright field, (b) dark field image formation.

Combined usage of dark field and bright field techniques enable one to identify crystal defects, such as dislocation, twins, stacking faults, etc.

Two theories are widely used to describe the intensities observed in electron diffraction by crystals. The "Kinematic theory" first developed by Hirsch et.al. [92], treat the crystal potential as constant and is therefore valid only for sufficiently small crystals.

The theory assumes that electron is scattered only once and that there is no interaction between the incident and scattered beams. The only boundary condition is that intensity and wavelength are conserved. For imperfect crystals, the theory predicts that dislocations should appear as dark lines on bright field micrographs, and that the contrast should be reversed in dark field micrographs. For large crystals, one has to take into account the multiple scattering of the incident wave, which requires the so-called "dynamical theory" [93,94]. The dynamical theory takes its name from the original X-ray treatment by Ewald [95] and treats the propagation of the electron waves through the crystals in terms of wave mechanics. Two significant and commonly observed consequences of the dynamical behaviour are extinction fringes and bend contours seen in electron images of crystals.

4. Electron Diffraction

The change from image to diffraction pattern is accomplished through the strength of the intermediate lens. In normal microscope operation, the image plane of the objective and that of the intermediate lens are conjugate foci and an enlarged image of the object is produced. If the focal length of the intermediate lens is decreased until the objective back focal plane is conjugate to the intermediate lens image plane, the diffraction pattern appears at the intermediate image plane.

The fundamental principle of electron diffraction is analogous to that of X-ray diffraction. The condition for diffraction is usually

expressed by Bragg's law which states that:

$$(66) \quad n\lambda = 2d \sin \varphi$$

when n is an integer (the order of reflection), d is the spacings between atomic planes and φ, the Bragg angle is measured between ray and plane. λ is the wavelength of the incident electron.

Experimentally, d-values can be obtained using a calibrated camera constant $L\lambda$ by means of the simple relation:

$$(67) \quad d = \frac{2L\lambda}{D}$$

where D is the diameter of the Debye-Scherrer ring, or twice the distance from the center of a pattern to a spot, and L is the effective specimen-to-plate distance. From the d-values so obtained, an identification may be made by comparing with tabulated list of d-values of known structures, such as the ASTM X-ray standard card file. A standard Aluminum film was used to calibrate the camera constant $L\lambda$.

If the electron diffraction pattern consists of only a few broad rings, the material is essentially amorphous. If there are continuous rings, as in a Debye-Scherrer pattern, the material is polycrystalline with random orientation. If the rings are spotty or grainy, the crystallite size is probably greater than one fifteenth of the selected area aperture. If the pattern consists of a systematic array of spots, the specimen is most probably single-crystalline. Missing rings and ring intensities which vary around the ring circumference in a symmetrical manner indicates a texturized material. If Kikuchi

lines are present, the specimen exhibits a high degree of perfection and and is relatively thick. Various diffraction anomolies have been discussed in detail by Pinsber [96].

(III) Measurements of Electrical Properties

1. Resistivity

A variety of approaches to the measurement of high resistivity have been suggested [97-100]. Such measurements are usually carried out on a bar shaped sample. In case of a flat, irregular sample, thin films for instance, van der Pauw's four probe method [101,102] offers a useful alternative. The van der Pauw technique, in its most general form, requires four contacts located anywhere on the periphery of a uniformly thick sample of arbitrary shape, two separate resistance measurements, the use of a theoretical curve and a calculation to arrive at a value for the reistivity. In order to obtain meaningful results, four conditions have to be satisfied. They are:

i) the contacts should be situated on the periphery of the sample,

ii) the contact should be small in comparison to the area of the sample,

iii) the sample should be homogeneous and free of holes, and

iv) the sample should be of constant thickness.

When these four conditions are met, it has been shown [101,102] that the resistivity, ρ, of the sample is given by:

$$(68)\quad \rho = \frac{\pi d}{\ln 2}\,\frac{(R_{AB,CD} + R_{BC,DA})}{2}\,f\left(\frac{R_{AB,CD}}{R_{BC,DA}}\right)$$

where d is the thickness of the sample, f is a dimensionless quantity dependent only upon the ratio of $R_{AB,CD}$ and $R_{BC,DA}$, as shown in Fig. 13. The resistances $R_{AB,CD}$ and $R_{BC,DA}$ are defined as:

$$(69)\quad R_{AB,CD} = \frac{V_D - V_C}{I_{AB}} \qquad \text{and}$$

$$(70)\quad R_{BC,DA} = \frac{V_A - V_D}{I_{BC}}$$

respectively. I_{AB} indicates the current enters at contact A and leaves at contact B. The derivation of equation (68) is given in Appendix B.

In the present experiments, the first and the last conditions were not exactly met, however, van der Pauw [101] had discussed and gave expressions for the relative errors involved. The errors were found to be negligible.

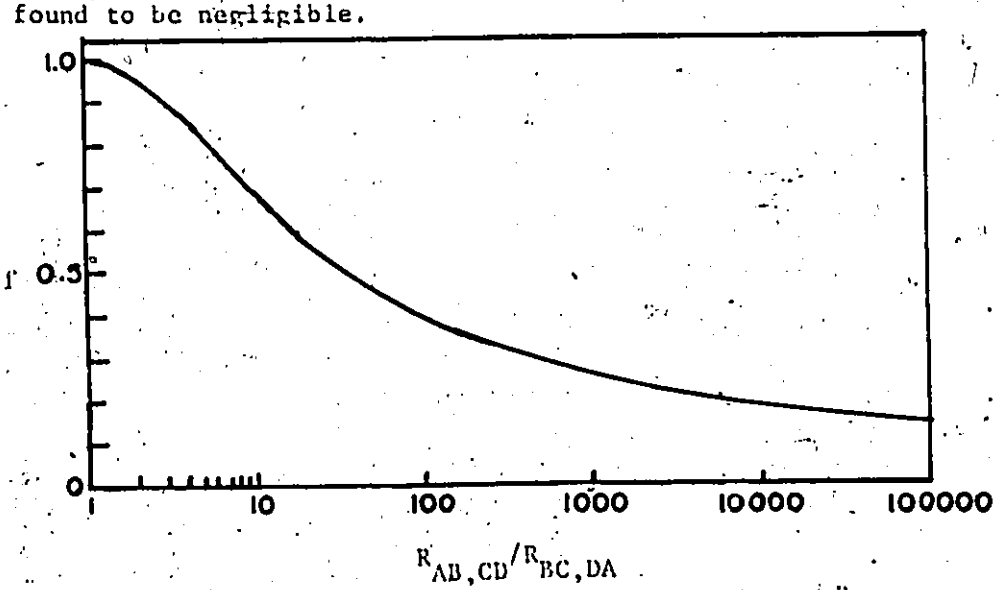

Fig. 13. Graphical representtion of the function $f\left(\frac{R_{AB,CD}}{R_{BC,DA}}\right)$ in equation (68).

It is necessary with a van der Pauw system to measure across different pairs of contacts in order to correct for the geometrical asymmetry, which requires interchanging current and voltage contacts to the sample. Next, to minimize the thermal potential across the sample, it is further necessary to reverse the polarity of the current. Hence, each resistance defined by equation (69) or (70) was obtained by averaging four measurements. The four configurations for resistance $R_{AB,CD}$ are shown in Fig. 14.

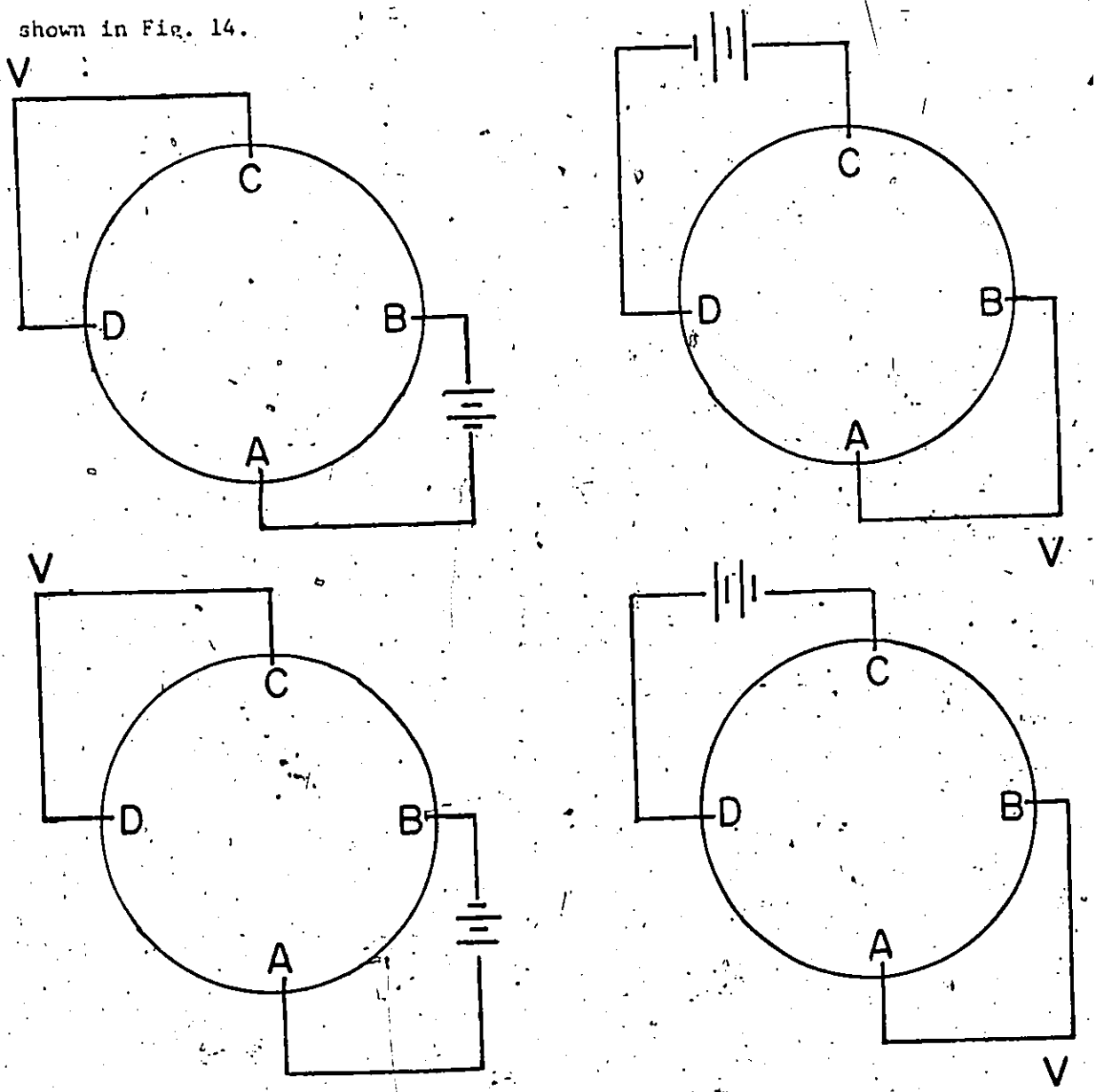

Fig. 14. The four configurations of resistance $R_{AB,CD}$ (or $R_{BC,DA}$) of the van der Pauw's method.

If sample contacts A, B, and C are appropriately switched, a single electrometer only is required to obtain the necessary data. A schematic circuit diagram for such a purpose is shown in Fig. 15. A Keithley 6 10 CR electrometer operated in normal mode was used to

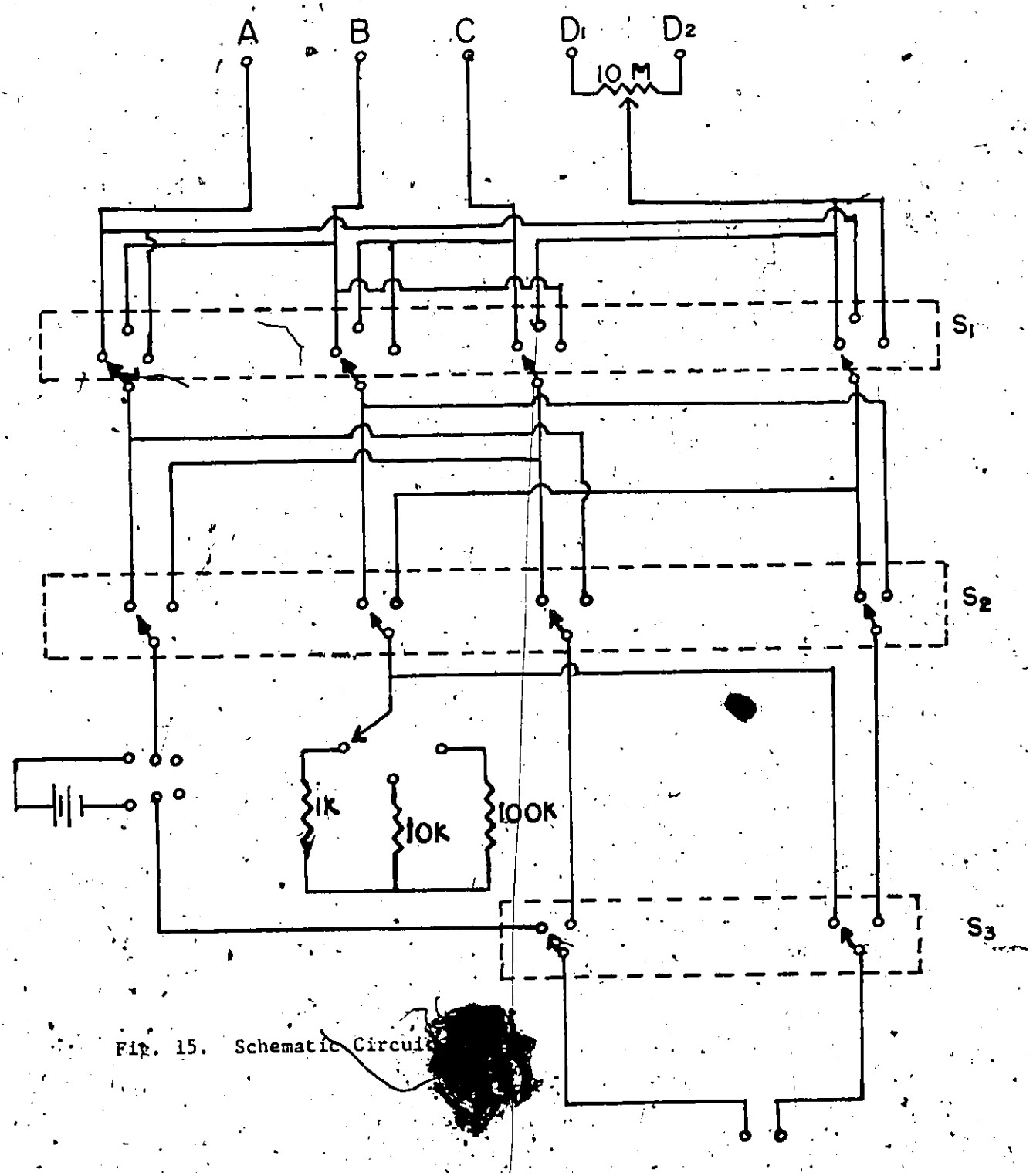

Fig. 15. Schematic Circuit

record all the measurements. The current was supplied by a 12.6 v mercury battery.

Fig. 16 illustrates a detailed view of the sample cell used in the present studies. The sample (1) is placed in a brass bar (2) which is connected to a liquid nitrogen dewar (3). A Teflon cover (4) with spring loaded electrode contacts (5) can be pressed onto the sample by the actions of the screws (6). This pressure arrangement ensures good contact even if the sample surface is not perfectly flat. After the sample has been loaded, the whole assembly can be fitted into a copper can (7) and sealed with O-rings (8). An inert gas can be admitted into the sample chamber through inlet (9). For measurements below room temperature, liquid nitrogen can enter the dewar through the inlets (10). For measurements above room temperature, the brass bar is heated electrically by connecting a power supply to the contacts (11) which are connected to Ni-Cr heating wires (12) wound around a piece of mica (13) attached to the back of the brass bar. The temperature of the sample is determined by two copper-constantant thermocouples (14) making contacts with the substrate. The electrode contacts and the liquid nitrogen dewar were made of stainless steel.

2. Hall Effect

According to van der Pauw [101,102], the Hall coefficient can be determined by measuring the change of the resistance $R_{AC,DB}$ when a magnetic field is applied perpendicular to the sample and is given by

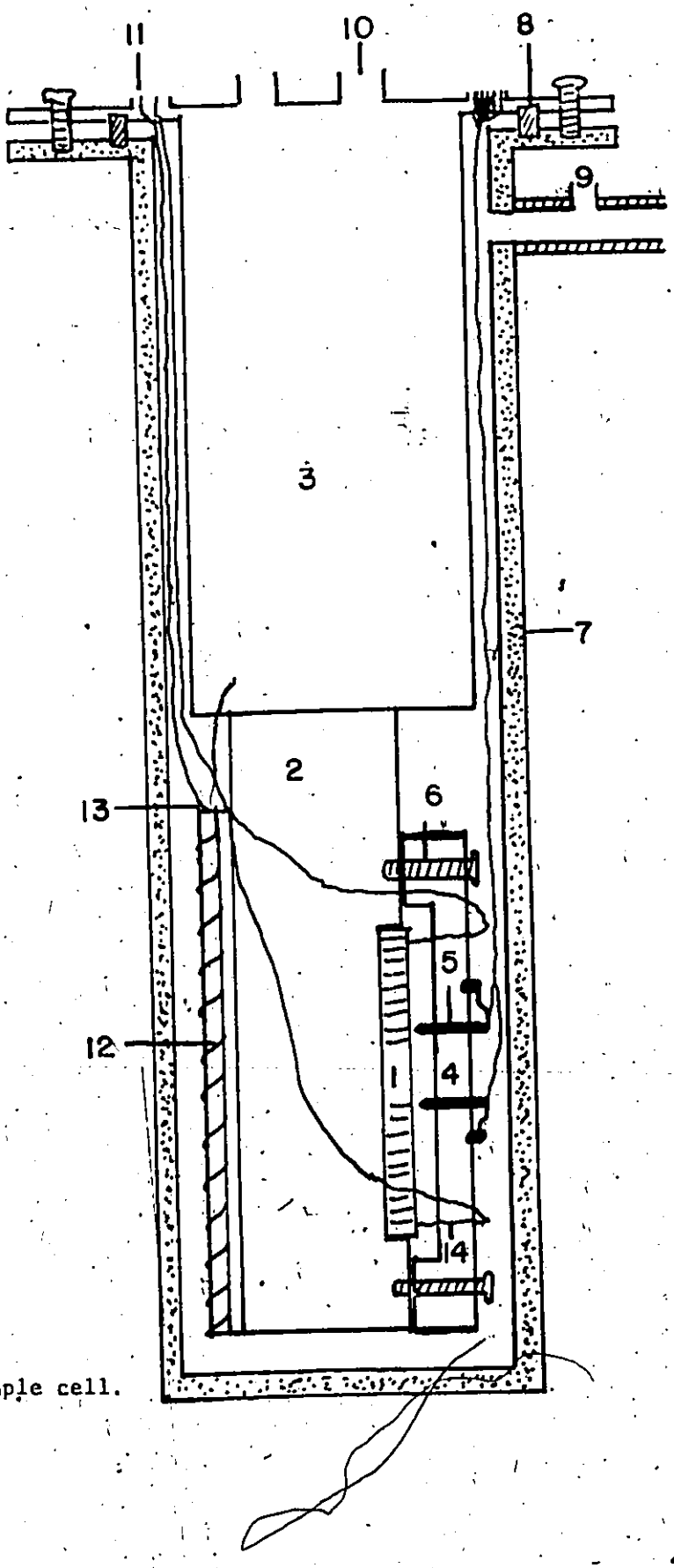

Fig. 16. Sample cell.

$$(71)\quad R_H = \frac{d}{B}\,\Delta R_{AC,DB}$$

where B is the applied magnetic field in gauss, and $\Delta R_{AC,DB}$ the change of the resistance $R_{AC,DB}$ due to the magnetic field.

The validity of equation (71) depends on the distribution of the current stream-line not changing when the magnetic field is applied. It has been shown [101] that this is true when the last two conditions (see page 51) are satisfied.

The Hall mobility μ_H in square centimeters per volt-second is given by [103]

$$(72)\quad \mu_H = 10^8 \frac{d}{B}\,\Delta R_{AC,DB}$$

$$= 10^8 \frac{R_{AC,DB}}{B}\left(\frac{R_{AB,CD} + R_{BC,DA}}{2}\right)^{-1} f^{-1}\left(\frac{R_{AB,CD}}{R_{BC,DA}}\right)\frac{\ln 2}{\pi}$$

Figure 17 illustrates schematically a sample connection used for Hall effect measurement. Before the magnetic field is applied, it is advisable to adjust the zero field voltage between B and D to as small a value as possible, since the actual Hall voltage is small. This is simply achieved by adjusting the 10 MΩ resistor which connects electrodes D_1 and D_2. Measurements were repeated with reversed current and reversed field, thus $\Delta R_{AC,DB}$ is the mean value of four measurements on $\Delta R_{AC,DB}$.

Knowing the polarity of the magnetic field, the direction of the current and the Hall voltage, the algebraic sign of the charge carriers

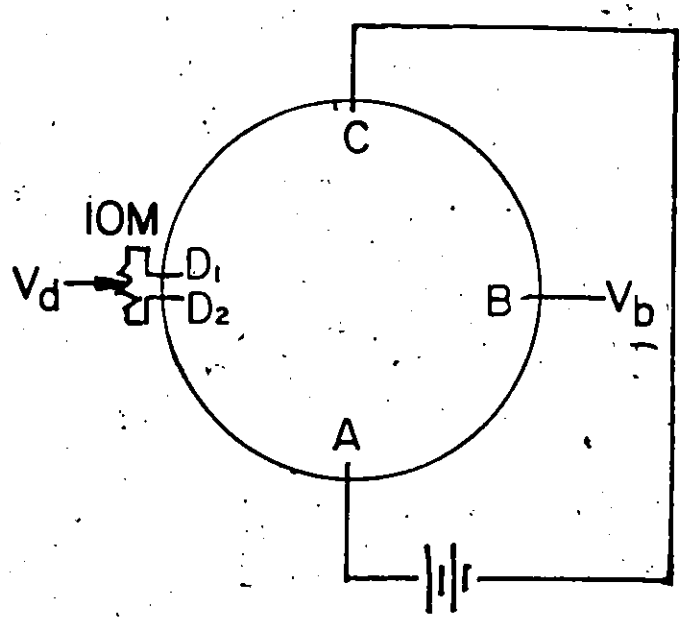

Fig. 17. Configuration for Hall effect measurement

and, hence, of the Hall coefficient, is determined.

A Keithley 180 nonovoltmeter was used to measure the Hall voltage.

3. Temperature

The temperature of the sample is measured by two copper-constantant thermocouples. The use of two thermocouples enables us to measure the temperature gradient across the film. A Hewlett-Packard 419 A DC Null Voltmeter was used to measure the thermocouple voltage.

With the present setup, only a point-by-point plot of resistivity vs temperature is obtained. To ensure adequate temperature

stability during measurements, the ratio of the resistance defined by equations (69) and (70) was examined point-by-point. If this ratio remains unchanged, the temperature variation during measurement can be kept to within 1°C [103].

Heat treatment of the sample was carried out as follows: - The sample was placed in the sample cell. The cell was first evacuated to about 10^{-5} torr pressure and then heated from room temperature to about 450°K with a constant heating rate of about 1°K/min. During the annealing process, the resistivities and temperatures of the sample were recorded every 10-15 minutes.

4. Temperature Coefficient of Resistivity

To measure the temperature coefficient of resistivity, the sample was first heated to 450°K as described previously, cooled down to room temperature and reheated to about 450°K. The resistivities vs temperatures taken during the second annealing cycle were used to calculate the temperature coefficient of resistivity.

CHAPTER 3

EXPERIMENTAL RESULTS

(I) Structure of Pretreated Surfaces

1. Sensitized/Catalyzed Surfaces

In Fig. 18, we present the electron micrographs of sensitized/catalyzed Formvar surfaces. Figure 18(a) is the electron micrograph of a Formvar surface after a one minute immersion in conventional sensitizer solution followed by a half minute distilled water rinse. Figure 18(b) is the Formvar surface after a one minute immersion in an improved presentitizer solution (aged $SnCl_4$) followed by the conventional treatment as that used in Fig. 18(a). Figure 18(c) represents the electron micrograph of a Formvar surface after a two minute immersion in Shipley's 9F catalyst solution followed by a one minute distilled water rinse. Figure 19 gives the electron diffraction patterns corresponding to the electron micrographs in Fig. 18.

The product on the sensitized surface appears to consist of particles of approximately 20 Å in diameter, agglomerated into dense clumps an order of magnitude or so larger.

The product of the improved sensitization reveals a denser and more uniform distribution of particles and clusters.

The product on the catalyzed surface appears to be uniformly distributed and shows less tendency to form clusters.

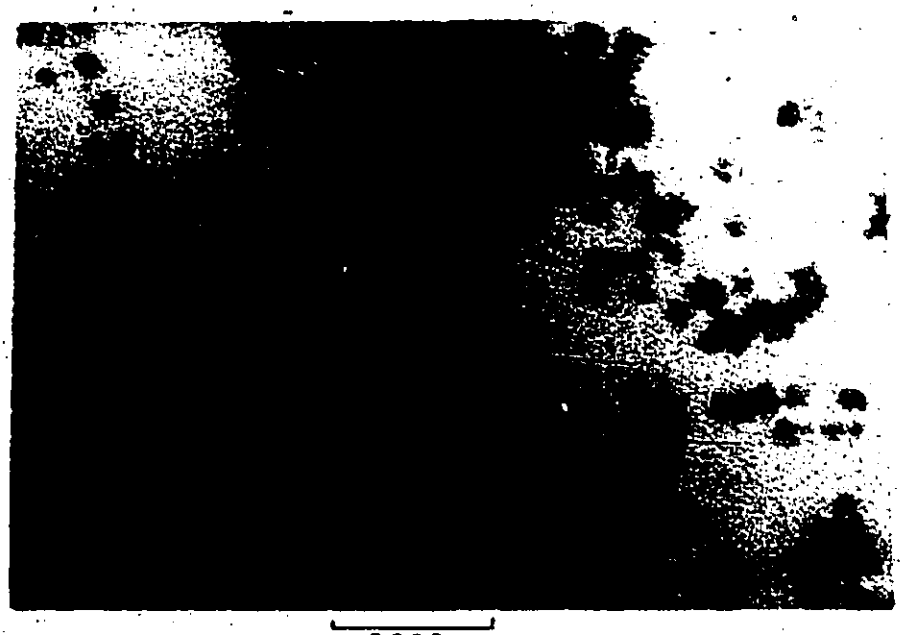

Fig.18(a) Electron micrograph of conventional sensitizer sensitized Formvar surface.

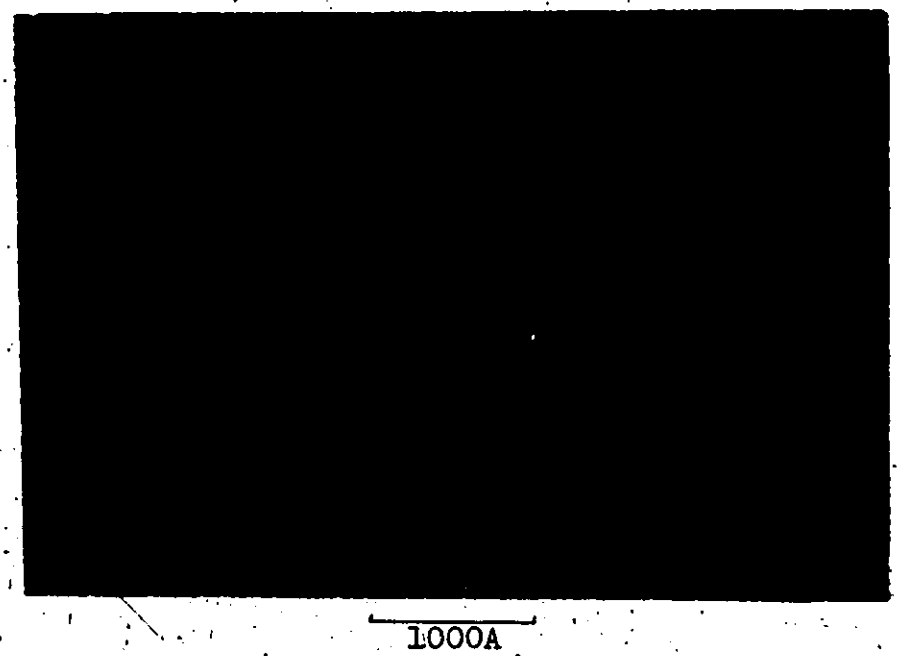

Fig.18(b) Electron micrograph of improved sensitizer sensitized Formvar surface.

Fig.18(c) Electron micrograph of catalyzed Formvar surface.

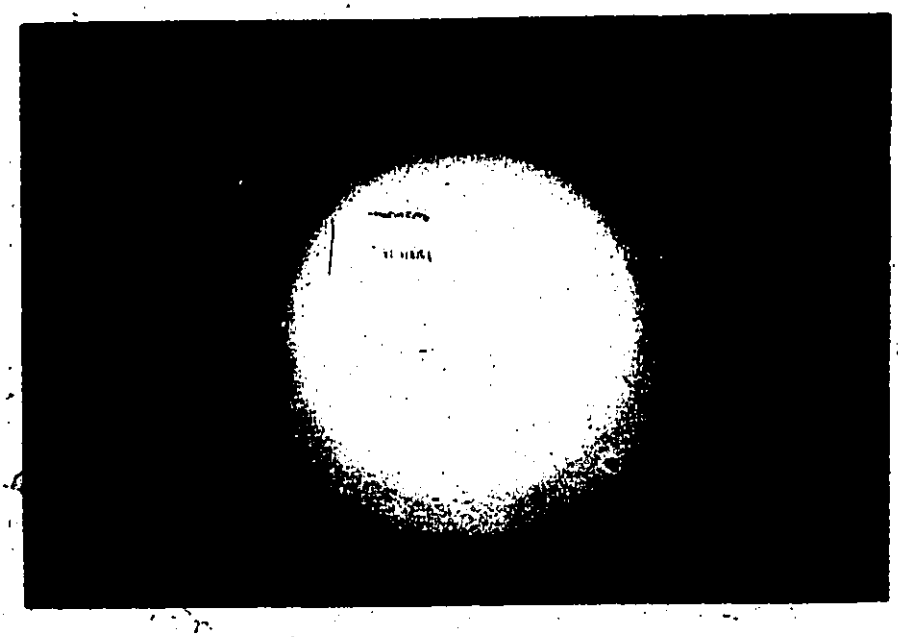

Fig.19(a) Electron diffraction pattern corresponding to Fig.18(a)

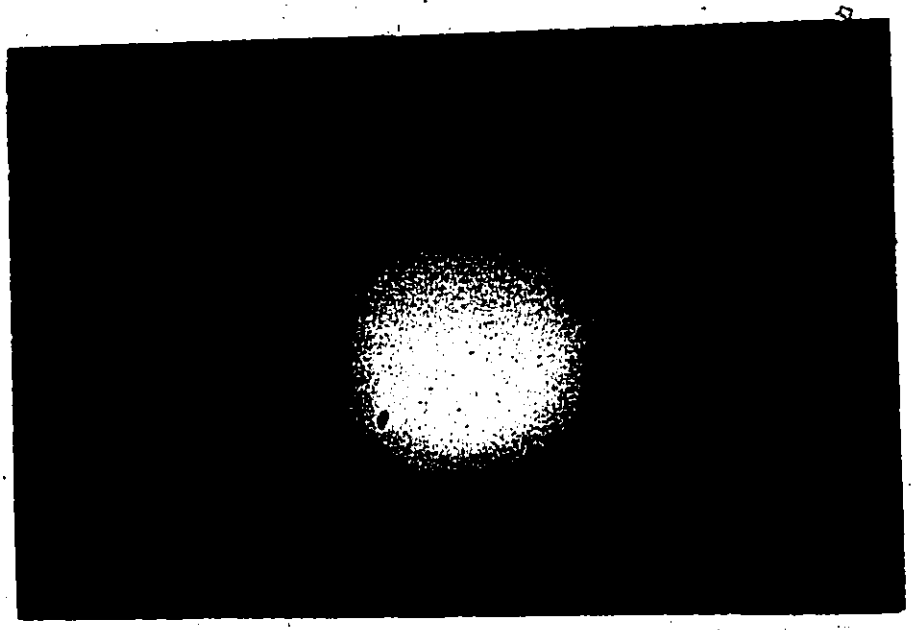

Fig.19(b) Electron diffraction pattern corresponding to Fig.18(b).

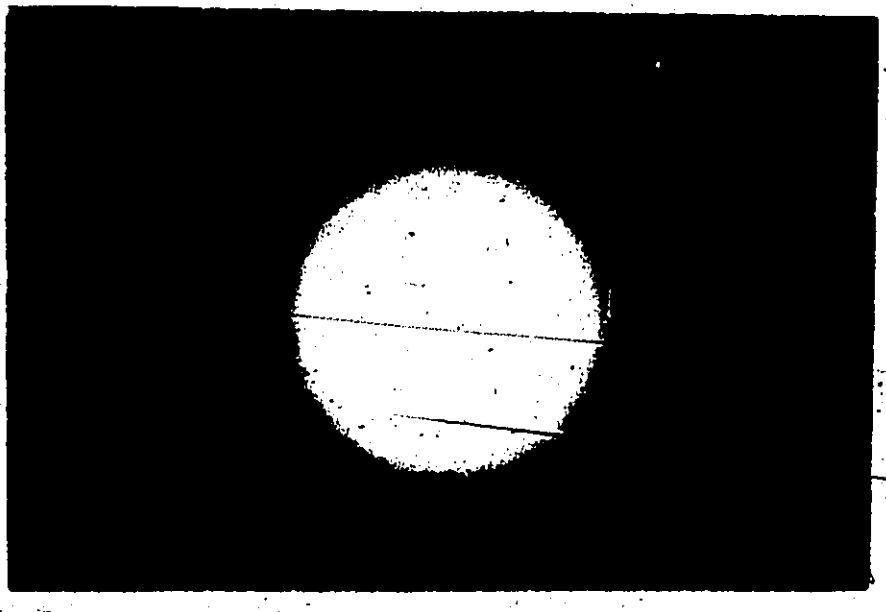

Fig.19(c) Electron diffraction pattern corresponding to Fig.18(c).

The particle density in the case of conventional sensitizer has been estimated to be 10^{11} particles/cm^2; in comparison, the particle density from improved sensitizer or catalytic solution is about 10^{12} particles/cm^2, an order of magnitude larger.

Preliminary analysis of the electron diffraction patterns reveals some very interesting results. From Fig. 19(a), (see Table V) we may conclude that the product on the conventional sensitizer surface is most probably hydrated stannic oxide. The product of the improved sensitization, however, is difficult to attribute to any crystalline structure. It may be a polymeric substance. From 19(c), we note that the product on the catalyzed surface is amorphous in character.

Table V presents the derived d-spacing for the surface formed as a result of treatment with conventional and the improved sensitizers.

TABLE V

d-spacings (Å) for Sensitized Surfaces

Conventional (Fig. 19(a))	Improved (Fig. 19(b))
3,155 (S)	3.255 (S)
1.969 (S)	3.025 (W)
1.652 (S)	2.142 (W)
1.356 (W)	2.065 (W)
1.095 (d)	1.678 (S)
	1.424 (W)
	1.142 (d)

S,W and d refer to strong, weak and diffuse respectively.

2. Activated/Accelerated Surfaces

In Fig. 20, we present the electron micrographs of sensitized/catalyzed and activated/accelerated Formvar surfaces. Fig. 20(a) is the electron micrograph of a Formvar surface after a one minute immersion in each of the conventional sensitizing and activating solutions followed by a half minute distilled water rinse after each step. Fig. 20(b) is the Formvar surface pretreated in the same way as that in Fig. 20(a) except for a one minute immersion in the improved presensitizer solution prior to the conventional sensitizer solution. Fig. 20(c) is the electron micrograph of a Formvar surface after a two minute immersion in each of the Shipley's 9F catalyst and 19F accelerator solutions followed by a one minute distilled water rinse after each step. In Fig. 21 we present the electron diffraction patterns corresponding to the electron micrographs of Fig. 20.

The product on the conventional sensitized and activated surface appears to consist of particles of approximately 50 Å in diameter and distributed more randomly than the product on the sensitized surface.

The product of the improved sensitization reveals a denser and more uniformly distributed particles. Some tendency for cluster formation still remains.

The product of the catalyzation appears to have a tendency for cluster formation. In contrast to the cluster formation in conventional sensitizer, in this system, the cluster seem to form in a worm-like fashion.

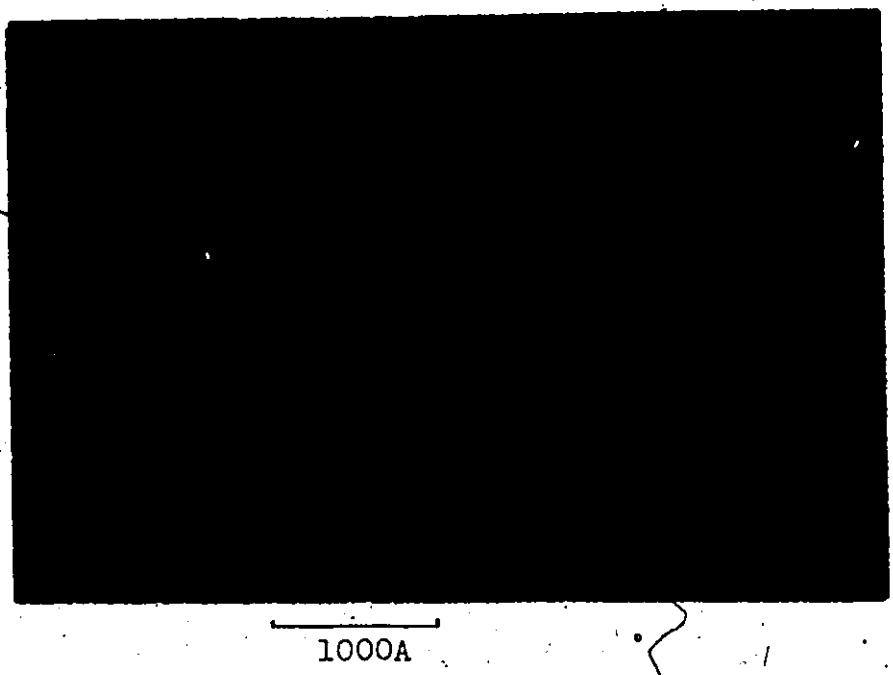

Fig.20(a) Electron micrograph of conventional sensitizer sensitized and activated Formvar surface.

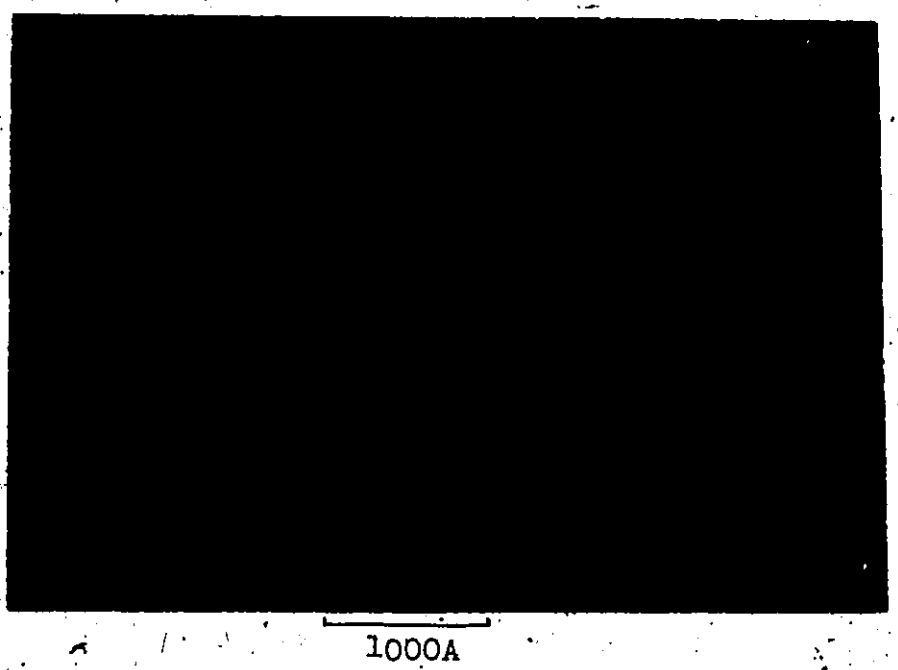

Fig.20(b) Electron micrograph of improved sensitizer sensitized and activated Formvar surface.

Fig. 20(c) Electron micrograph of catalyzed and accelerated Formvar surface.

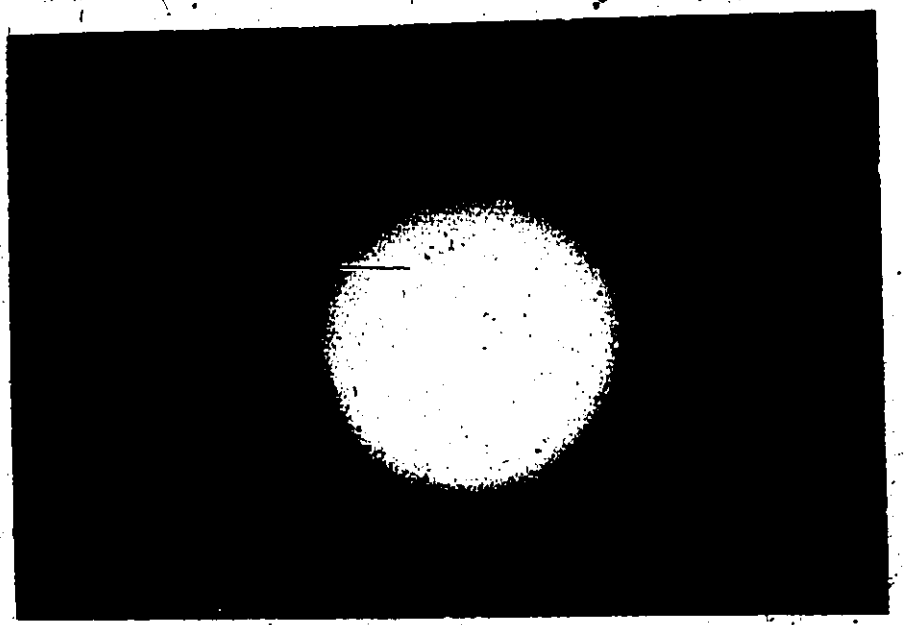

Fig.21(a) Electron diffraction pattern corresopnding to Fig.20(a).

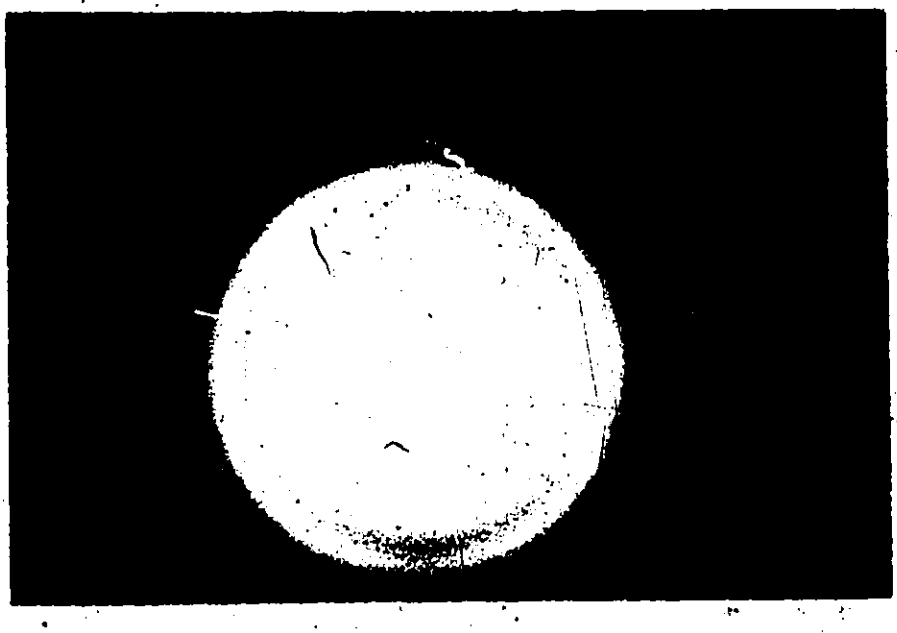

Fig.21(b) Electron diffraction pattern corresponding to Fig.20(b).

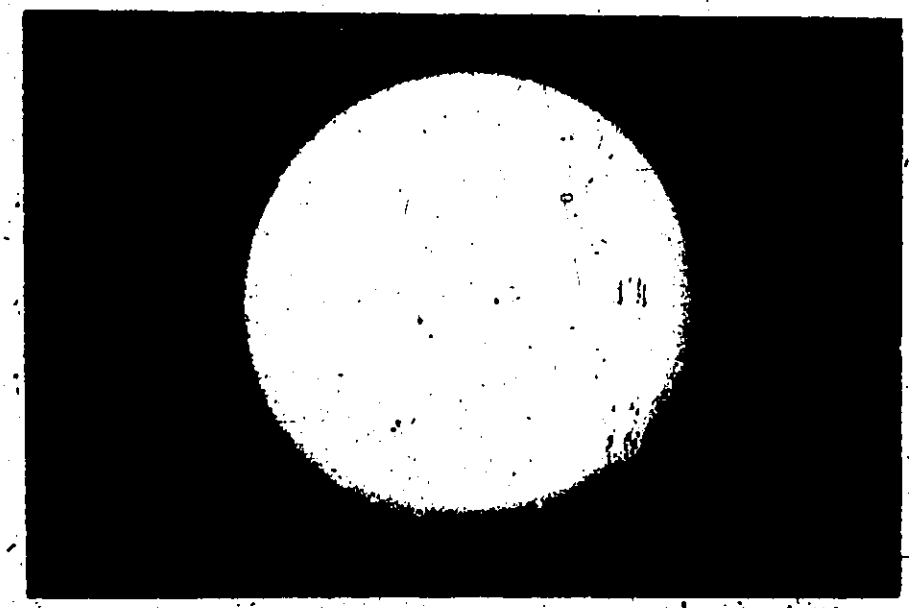

Fig.21(c) Electron diffraction pattern corresponding to Fig.20(c).

From the diffraction patterns in Fig. 21(a) and (b), we conclude that the product after the conventional and the improved sensitizer treatment are amorphous in character. The electron diffraction pattern in Fig. 21(c), however, can easily be indexed as a f.c.c. material with lattice parameters closely matching those of Pd_3Sn [105].

Table VI summarizes the derived parameters corresponding to Fig. 21(c) together with the derived parameters of Pd_3Sn from literature.

TABLE VI

Lattice Parameters (Å) Corresponding to Fig. 21(c)

h	k	l	Experimental Values	Derived from Ref. [105]
1	1	1	2.288	2.295
2	0	0	2.010	1.985
2	2	0	1.400	1.404
3	1	1	1.207	1.198
2	2	2	1.150	1.147
3	3	1	0.903	0.912

Pd_3Sn: f.c.c. with $a_o = 3.97$ [105].

3. Effect of u.v. Light Irradiation

Fig. 22 shows the effect of ultra violet irradiation on the (a) sensitized, and (b) sensitized and activated Formvar surfaces.

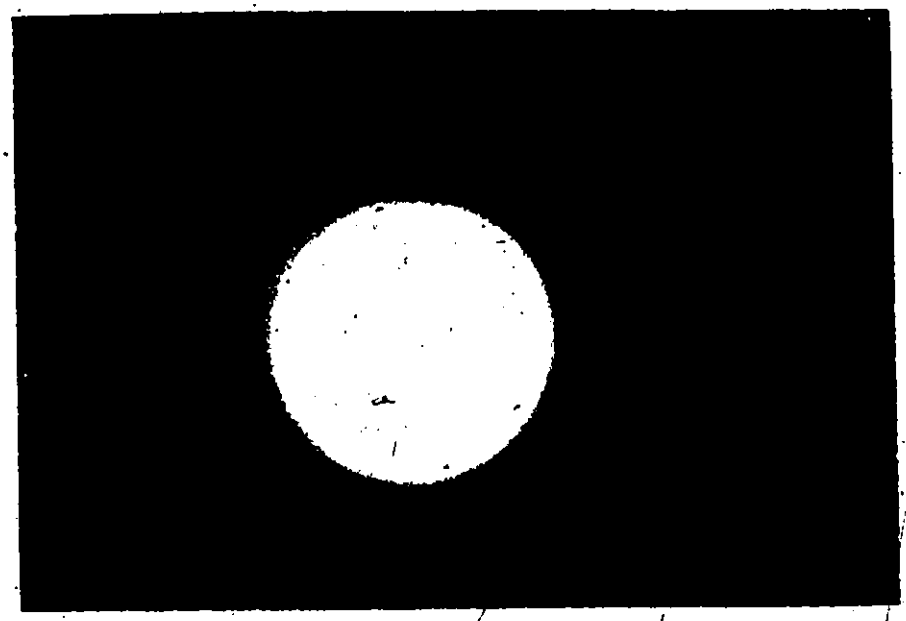

Fig. 22(a) Electron diffraction pattern of a sensitized Formvar surface after 50 min. U.V. irradiation

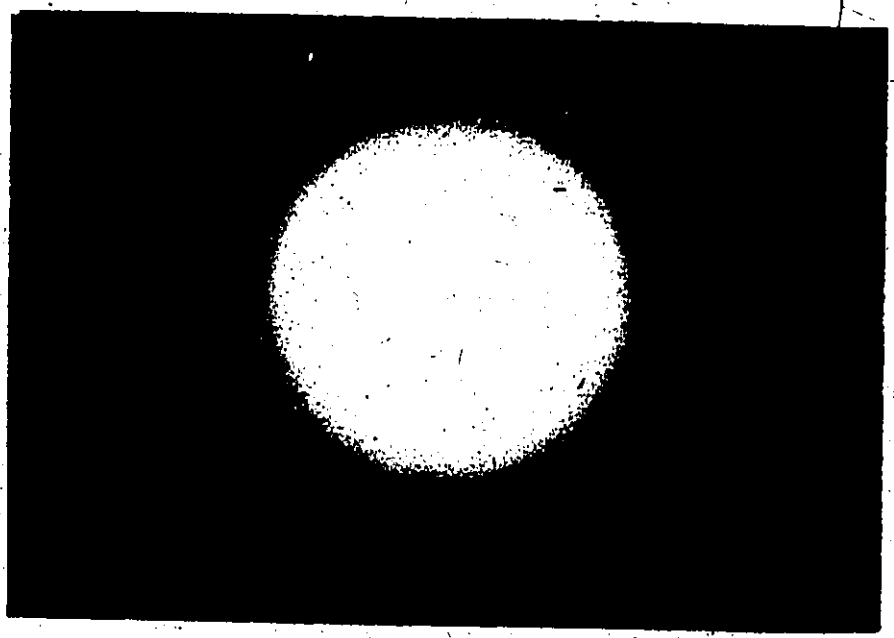

Fig. 22(b) Electron diffraction pattern of a sensitized and activated Formvar surface after 50 min. U.V. irradiation.

The electron diffraction pattern obtained after 50 minutes of u.v. illumination are shown for each case. We have found that the u.v. treatment is effective at both stages in inhibiting the deposition of nickel and cobalt. In the case of copper, however, u.v. light is effective only after the sensitization.

(II) Structure of Electroless Thin Metal Films

1. Electroless Ni-P Films

In Fig. 23, we present the electron micrographs of Ni-P films deposited on Formvar coated glass from an acidic bath with pH = 5.3. Fig. 23(a) is the Ni-P film deposited on conventional sensitizer treated surfaces. Fig. 23(b) is the same except for a surface pretreated by improved sensitizers. Fig. 23(c) is the Ni-P film deposited on Shipley's catalytic solution treated surface. The deposition time is indicated in the figure caption. In Fig. 24, we present the electron diffraction patterns corresponding to Fig. 23.

The Ni-P islands are seen to be almost spherical in shape and separated from one another by a "channel" of width in the order of a few Å. The diffraction patterns feature two broad diffuse rings characteristic of an amorphous material.

In Fig. 25, we present the electron micrographs of Ni-P films deposited on Formvar coated glass from different alkaline baths. The pH value of the different alkaline baths corresponding to the figures are (a) pH = 8.5; (b) pH = 10.5 and (c) pH = 10.5. The pretreatment

Fig.23(a) Electron micrograph of electroless Ni-P deposited from an acidic bath pH=5.3 using conventional sensitizer. Deposition time = 8 min..

Fig.23(b) Electron micrograph of electroless Ni-P deposited from an acidic bath pH=5.3 using improved sensitizer. Deposition time = 3 min..

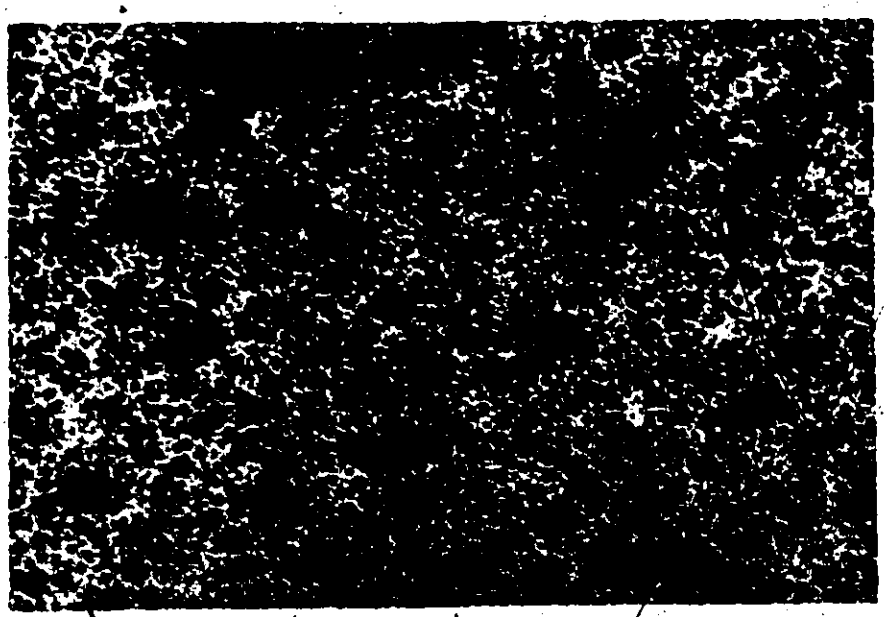

Fig.23(c) Electron micrograph of electroless Ni-P deposited from an acidic bath pH=5.3 using Shipley's catalytic solution. Deposition time = 1.5 min..

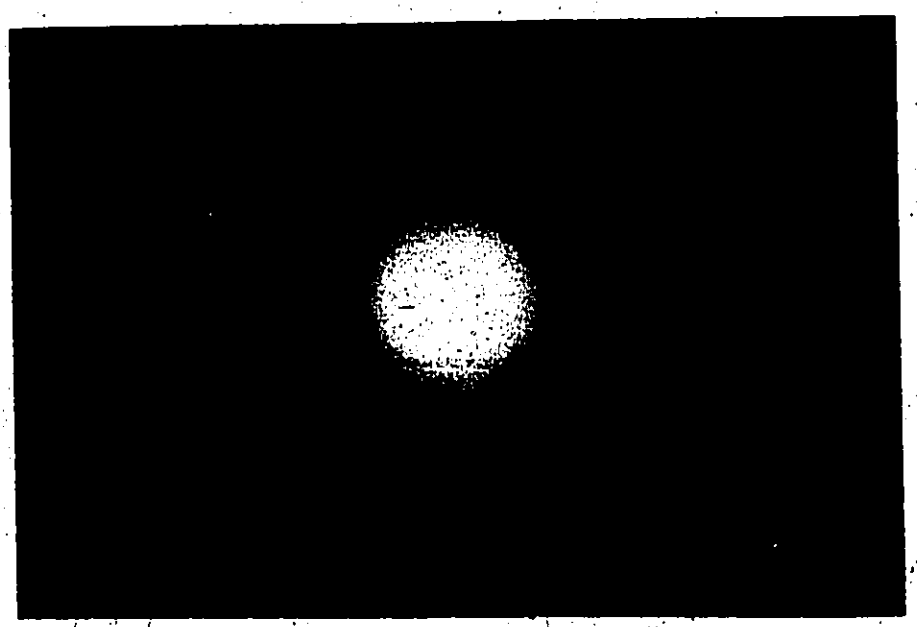

Fig.24(a) Electron diffraction pattern corresponding to Fig.23(a).

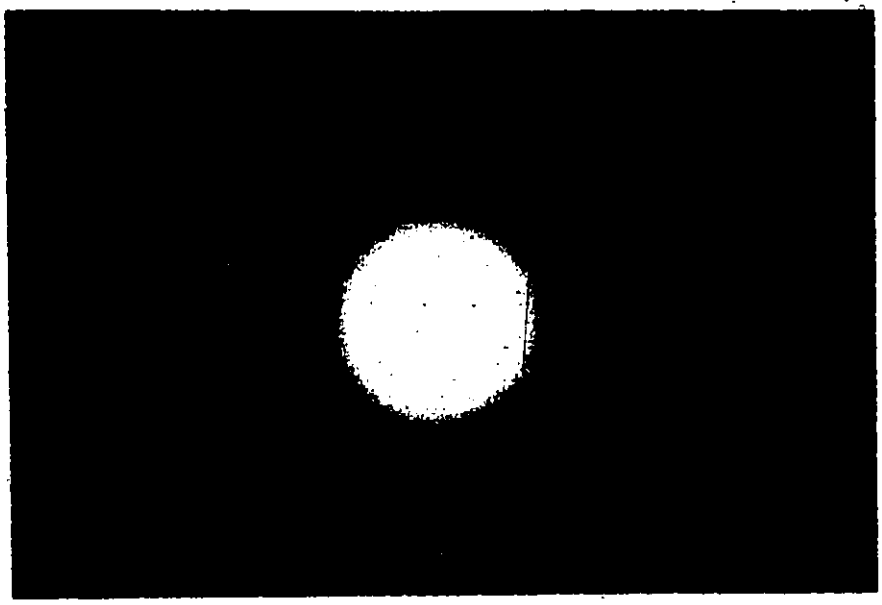

Fig.24(b) Electron diffraction pattern corresponding to Fig.23(b)..

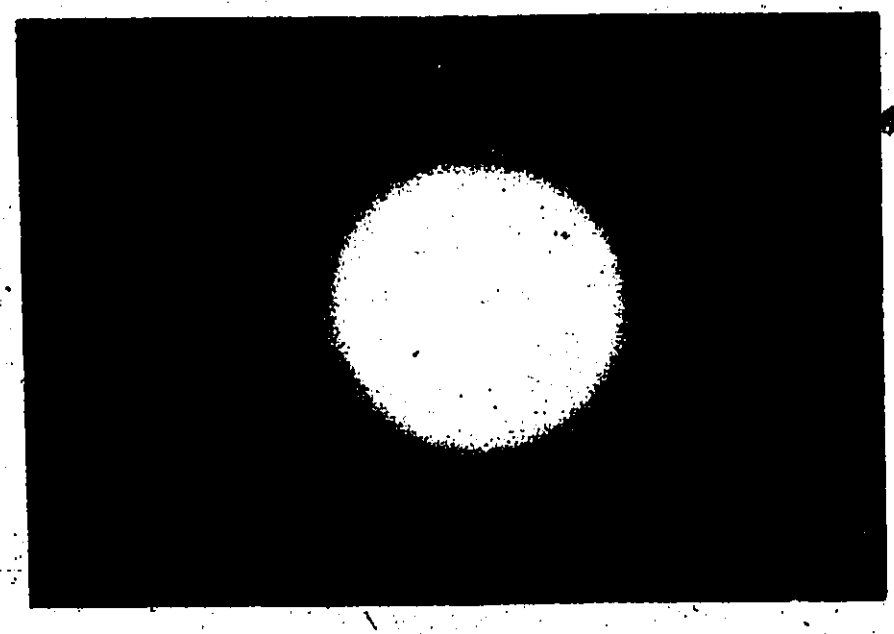

Fig.24(c) Electron diffraction pattern corresponding to Fig.23(c).

solutions corresponding to the figures are (a) conventional sensitizer, (b) conventional sensitizer and (c) Shipley's catalytic solutions. The deposition time is indicated in the figure captions. In Fig. 26, we present the electron diffraction patterns corresponding to Fig. 25.

Here we noted that the alkaline deposited Ni-P islands are irregular in shape. Of particular interest is the Ni-P products on the catalytic solutions treated surface. Here the worm-like growth pattern is quite evident.

The diffraction patterns demonstrate a change of degree of crystallinity as the pH value is increased, (see Figs. 25(a) and (b)). The crystalline structure is easily indexed as a f.c.c. material with lattice parameters matching closely that of nickel.

Unlike the Ni-P films deposited from an acidic bath, here we also noted that the effect of the Shipley's catalytic solution results in the formation of larger microcrystallite size as demonstrated by the spotty ring diffraction pattern in Fig. 26(c).

Table VII summarizes the derived d-spacings corresponding to Fig. 26(b) and (c) together with the theoretical values of nickel.

TABLE VII

Lattice Parameters in (Å) Corresponding to Fig. 26(b) and (c)

h	k	l	Experimental values	Theoretical values
1	1	1	2.050	2.034
2	0	0	1.780	1.762
2	2	0	1.262	1.246
3	1	1	1.072	1.062
2	2	2	1.025	1.017
6	0	0	0.890	0.881
3	3	1	0.815	0.808

*Ni = f.c.c. with a_o = 3.523 [AXTM 4-850]

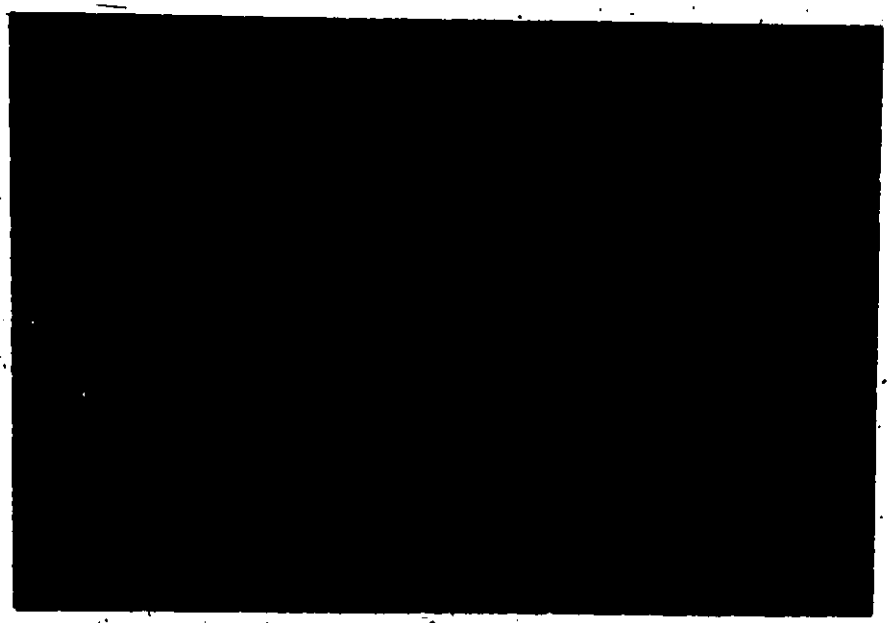

Fig.25(a) Electron micrograph of electroless Ni-P deposited from bath pH=8.5 using conventional sensitizer. Deposition time = 4 min..

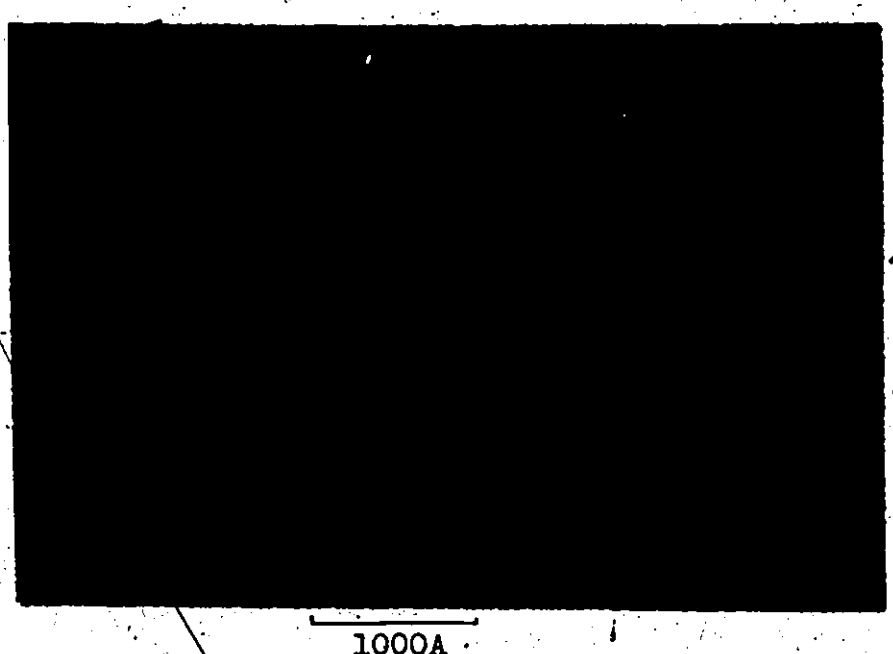

Fig.25(b) Electron micrograph of electroless Ni-P deposited from bath pH=10.5 using conventional sensitizer. Deposition time = 2.5 min..

1000A

Fig.25(c) Electron micrograph of electroless Ni-P deposited from bath pH=10.5 using Shipley's catalytic solution. Deposition time = 45 sec..

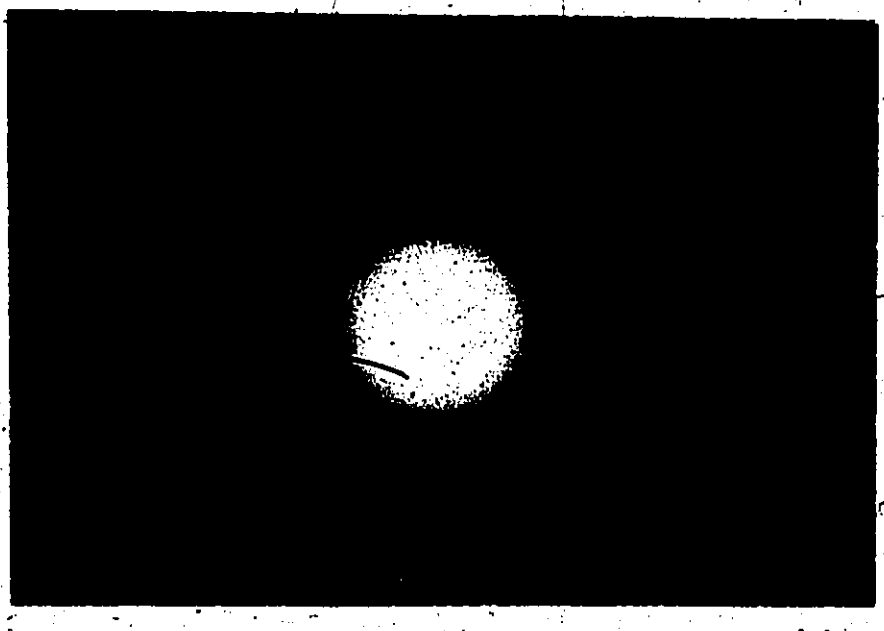

Fig.26(a) Electron diffraction pattern corresponding to Fig.25(a).

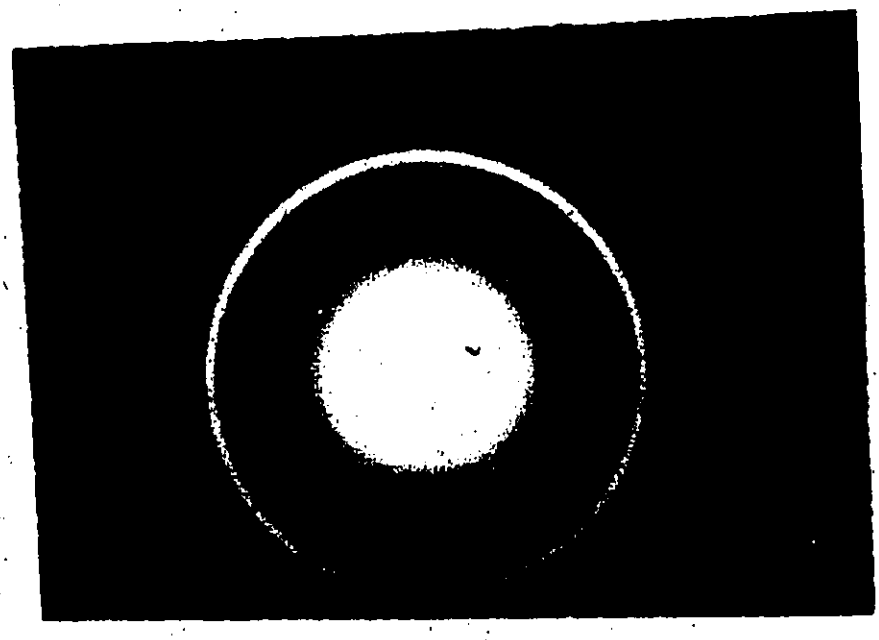

Fig.26(b) Electron diffraction pattern corresponding to Fig.25(b).

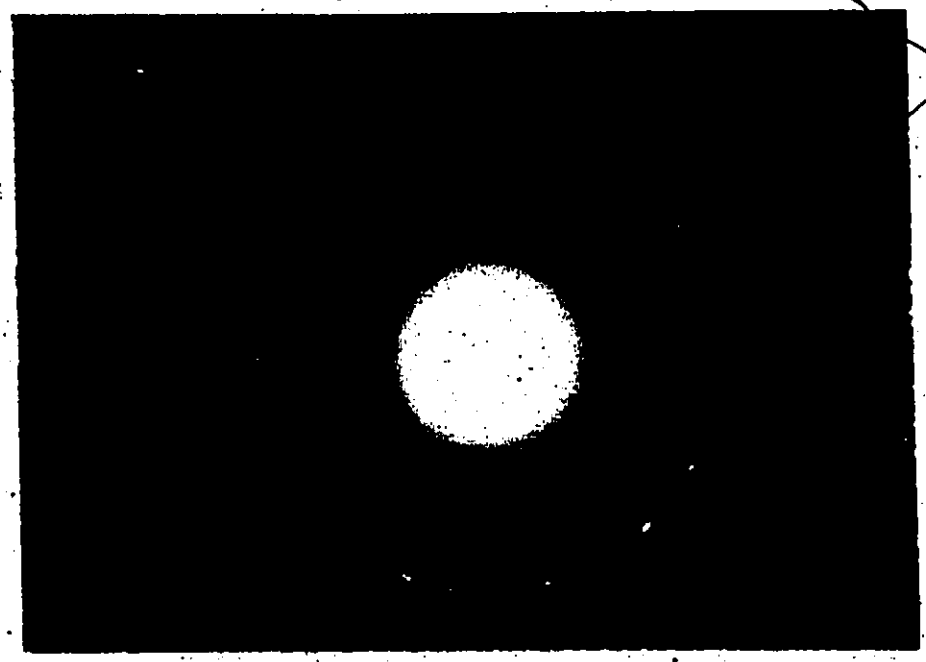

Fig.26(c) Electron diffraction pattern corresponding to Fig.25(c).

In Fig. 27, we present the dark field electron micrographs taken at the first diffraction ring (111) of Ni-P films deposited on Formvar coated glass. Fig. 27(a) is the Ni-P film deposited using Shipley's catalytic solution from an acidic bath with pH = 5.3. Fig. 27(b) is the same except from an alkaline bath of pH = 8.5. The aim of presenting these dark field electron micrographs will be made clear later in the discussion.

2. Electroless Ni-Co-P Films

In Fig. 28, we present the electron micrographs of Ni-Co-P films (65% Ni) deposited from different alkaline baths. Shipley's catalytic solution was used to activate the Formvar surface. The pH values of the baths corresponding to the figures are (a) pH = 8, (b) pH = 10. In Fig. 29, we present the electron diffraction patterns corresponding to Fig. 28.

The product of Ni-Co-P films are remarkably similar in morphology to the products of Ni-P. The Ni-Co-P islands are also almost spherical in shape. Here again, we observed that the change of pH values induce a change of degree of crystallinity. The diffraction patterns of Fig. 29 clearly demonstrate this point. Also, the diffraction pattern of Fig. 29(b) can be indexed as f.c.c. nickel.

Table VIII summarizes the derived lattice parameters corresponding to Fig. 29(b) together with the theoretical values of nickel.

The results presented here are generally true regardless of the specific pretreatment solution used.

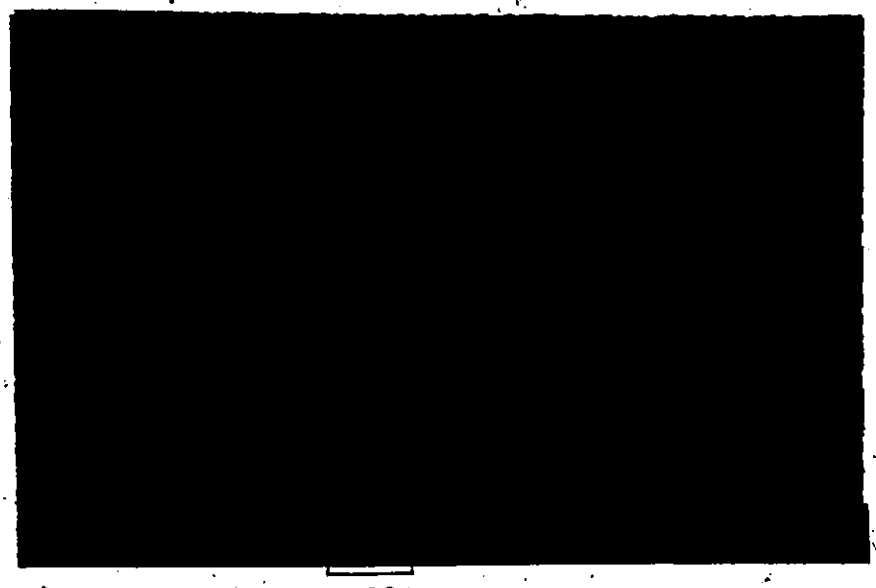

1000A

(a)

Deposition time = 1 min.

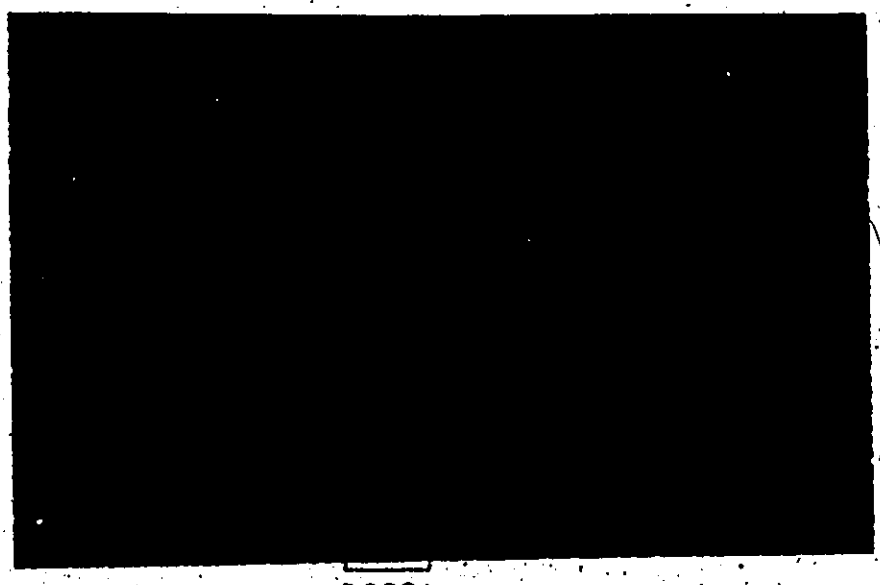

1000A

(b)

Deposition time = $\frac{1}{4}$ min.

Fig.27 Dark field electron micrographs taken at the first diffraction peak of electroless Ni-P deposoted from (a) acidic bath pH=5.3, (b) alkaline bath pH=8.5, using Shipley's catalytic solution.

(a)

Deposition time = 1.5 min.

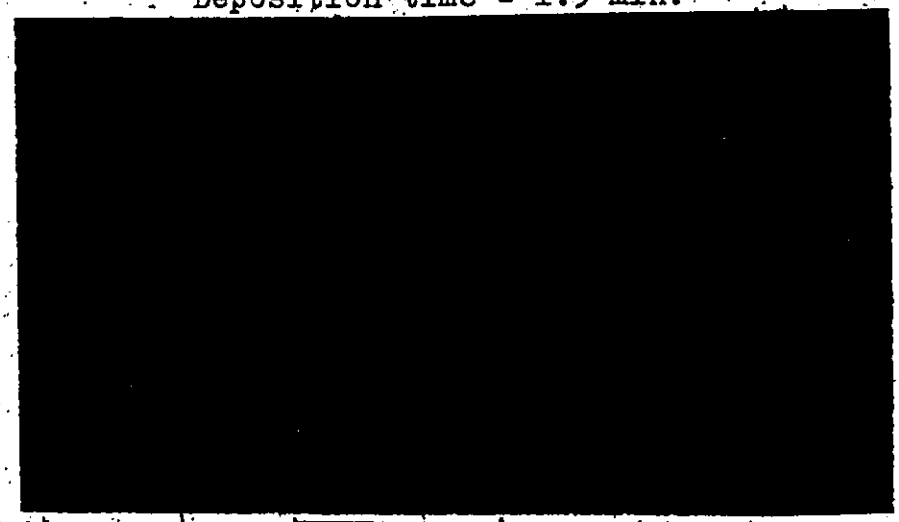

(b)

Deposition time = 1 min.

Fig.28 Electron micrographs of electroless Ni-Co-P (65% Ni) deposited from alkaline baths: (a) pH=8, (b) pH=10, using Shipley's catalytic solution.

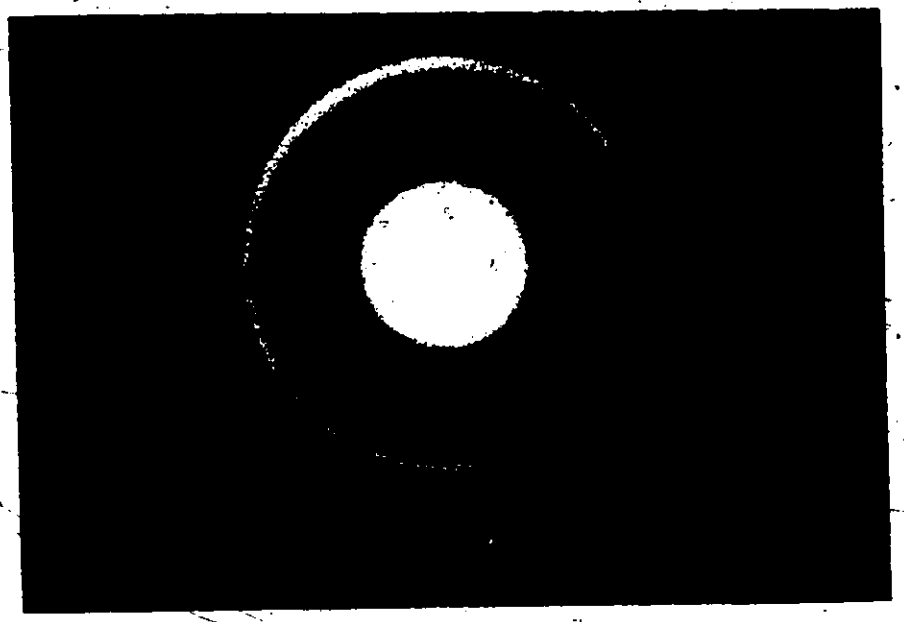

(a)

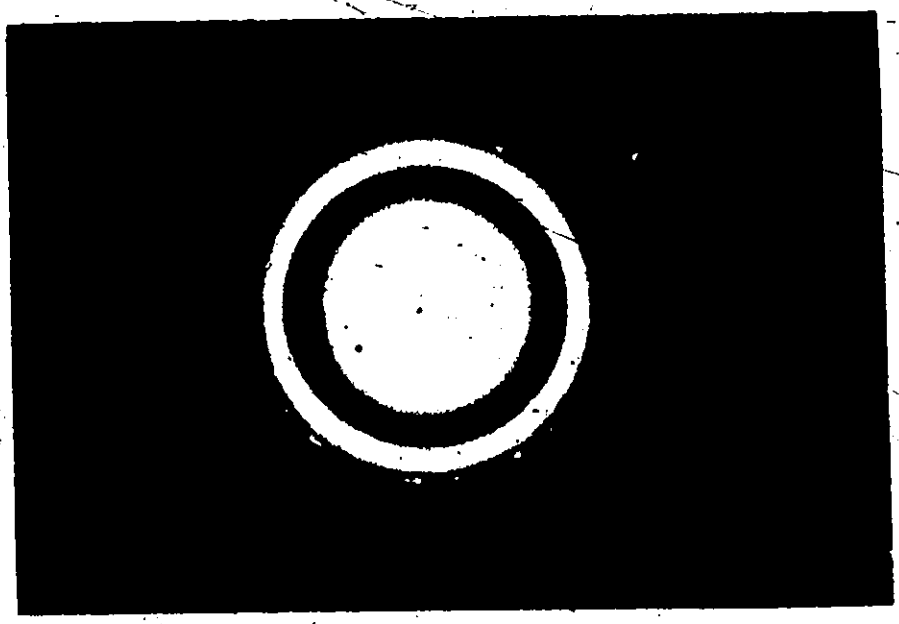

(b)

Fig.29 Electron diffraction patterns corresponding to (a) Fig.28(a), and (b) Fig.28(b), respectively.

TABLE VIII

Lattice Parameter in (Å) Corresponding to Fig. 29(b)

h	k	l	Experimental values	Theoretical values
1	1	1	2.032	2.036
2	0	0	1.758	1.762
2	2	0	1.260	1.246
3	1	1	1.075	1.062
2	2	2	1.021	1.017
4	0	0	0.880	0.881
3	3	1	0.810	0.808

3. Electroless Co-P Films

In Fig. 30, we present the electron micrographs of Co-P films deposited from different alkaline baths. The pH values of the different baths corresponding to the figures are (a) pH = 8, (b) pH = 9.5, (c) pH = 10.5. The concentration of sodium hypophosphite is 25 gm/litre. In order to show the effect of hypophosphite concentration, Fig. 30(d) presents the electron micrographs of Co-P deposited from an alkaline bath with pH = 9.5 and the concentration of sodium hypophosphite is 40 gm/litre, except Fig. 30(d) which was pretreated with Shipley's catalytic solution, conventional sensitizers were used to pretreat the Formvar surfaces. In Fig. 31, we present the electron diffraction patterns corresponding to Fig. 30.

1000A

Fig. 30 (a)

1000A

Fig. 30 (b)

Fig. 30 (c)

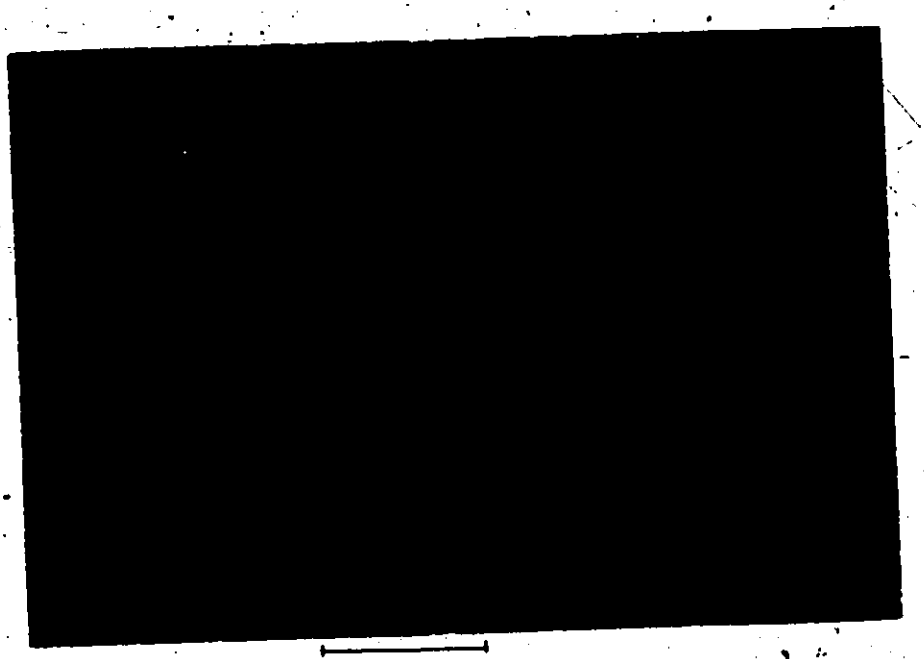

Fig. 30 (d)

Fig.30 Electron micrographs of electroless Co-P deposited from (a) pH=8, (b) pH=9.5, (c) pH=10.5 with "hypophosphite"=25 gm/liter using conventional sensitizer and (d)pH=9.5 with "hypophosphite"=40 gm/liter using Shipley's catalytic solution.

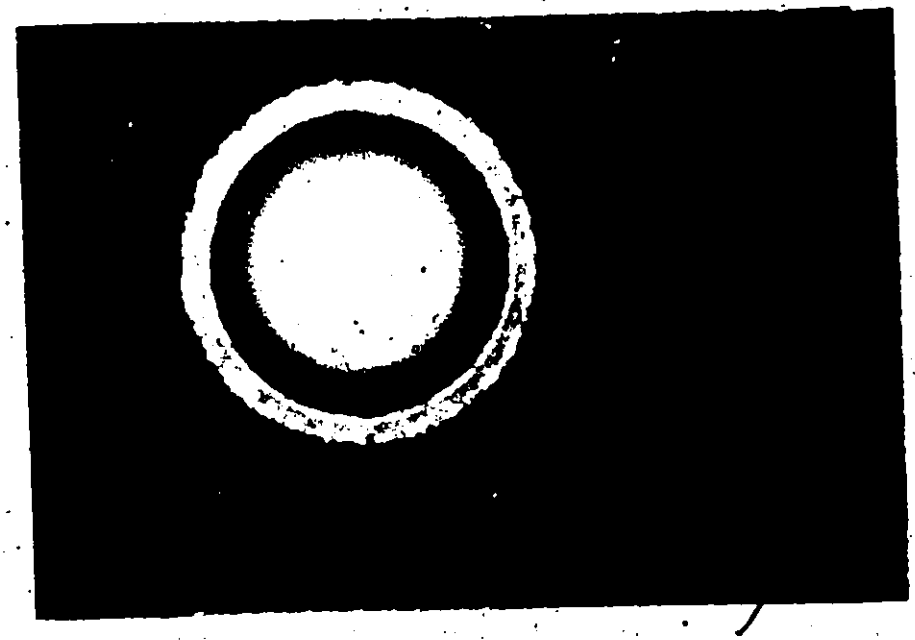

Fig.31(a)

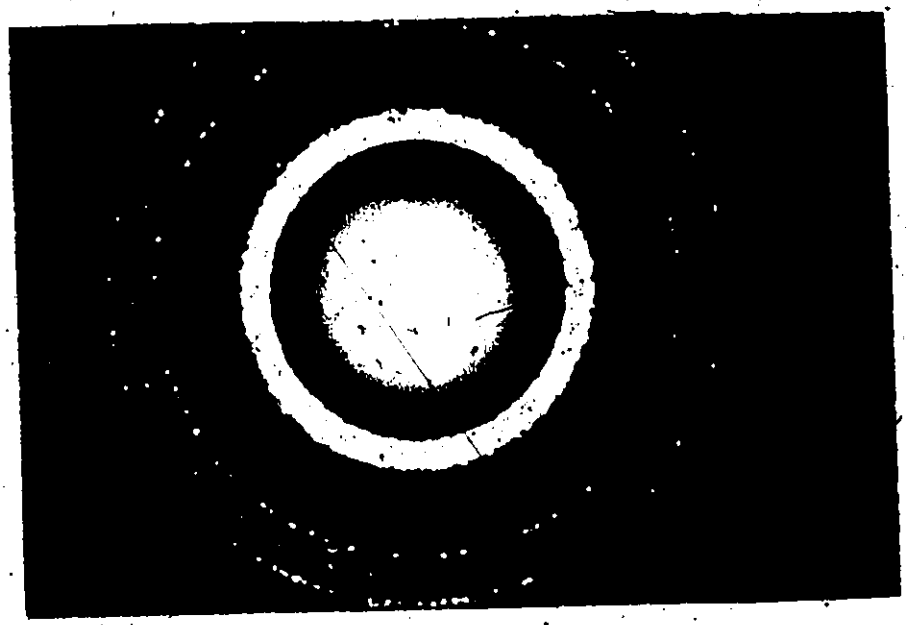

Fig.31(b)

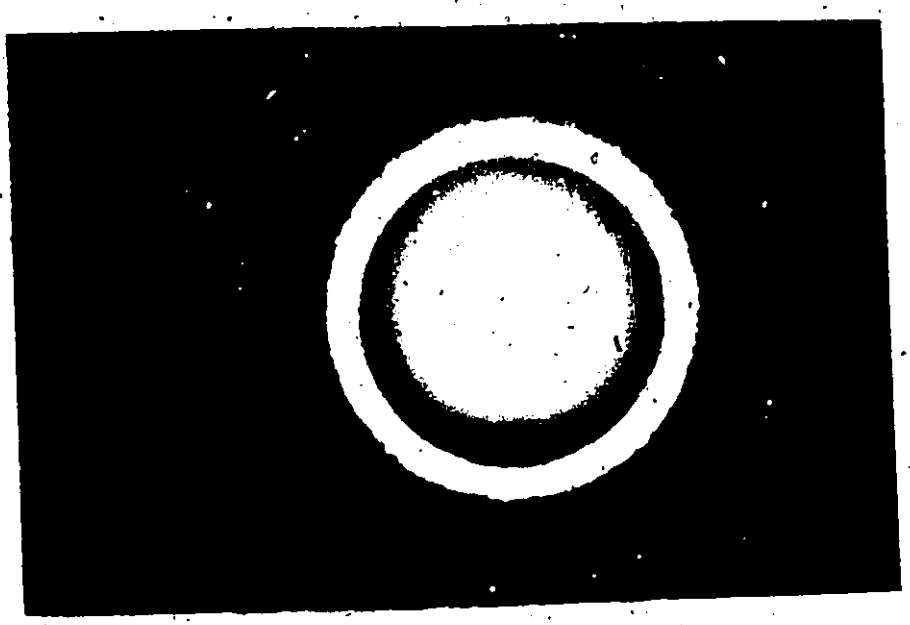

Fig.31(c)

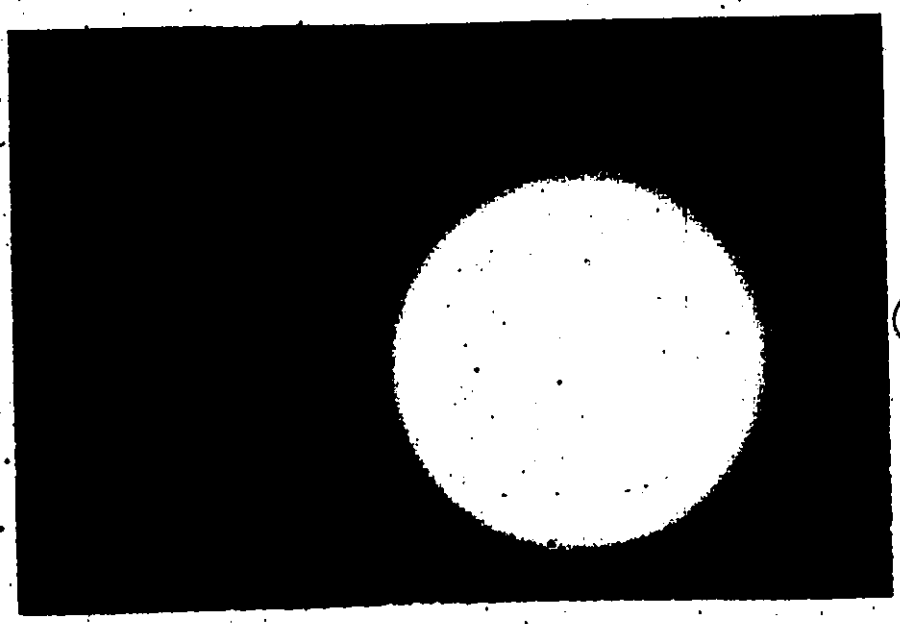

Fig.31(d)

Fig.31 Electron diffraction patterns corresponding to Fig.30 respectively.

Essentially, no dramatic changes can be observed by comparing the electron micrographs presented in Fig. 30. The islands of Co-P are irregular in shape and groups of fringes are evident. However, the Co-P products on the catalyzed surface are much smaller in size and no groups of fringes were observed. The electron diffraction patterns can be indexed as a mixture of h.c.p. and f.c.c. cobalt phases.

Table IX summarizes the lattice parameters derived from Fig.31(a-c). The last column presents the lattice parameters derived from a typical vacuum evaporated cobalt electron diffraction pattern presented in Fig. 32.

4. Heat Treated Electroless Thin Metal Films

No structure changes can be observed for any electroless thin metal films, i.e. Ni-P, Ni-Co-P and Co-P, when heated in a vacuum of about 10^{-5} Torr from room temperature to about 450°K.

In Figure 33, we present a typical heat treated Co-P film corresponding to Fig. 30(b). The only observable change is the disappearance of the groups of fringes which might be an indication of the annihiliation of microcrystallites.

(II) Electrical Properties and Hall Effects of Electroless Thin Metal Films

1. Sheet Resistivity

In Figures 34 and 35, we present the sheet resistivity (ρ/d).

TABLE IX. Lattice Parameters in (Å) corresponding to Fig. 31 and Fig. 32

Experimental Value	Theoretical Values* h.c.p. (h k.l)	f.c.c. (h k l)	Experimental Value**
2.523			
2.146	2.165 (01.0)		2.152
2.061	2.023 (00.2)	2.048 (111)	2.030
1.902	1.910 (01.1)		1.896
1.783		1.775 (200)	
1.518	1.480 (01.2)		1.479
1.259	1.252 (11.0)	1.255 (220)	1.247
1.150	1.149 (01.3)		1.147
1.078	1.083 (02.0)	1.071 (311)	
1.062	1.066 (11.2)		1.066

* α-Co: h.c.p. with a_o = 2.507, c_o = 4.070 [AXTM 5-727]

β-Co: f.c.c. with a_o = 3.548

** Corresponds to vacuum evaporated Co films

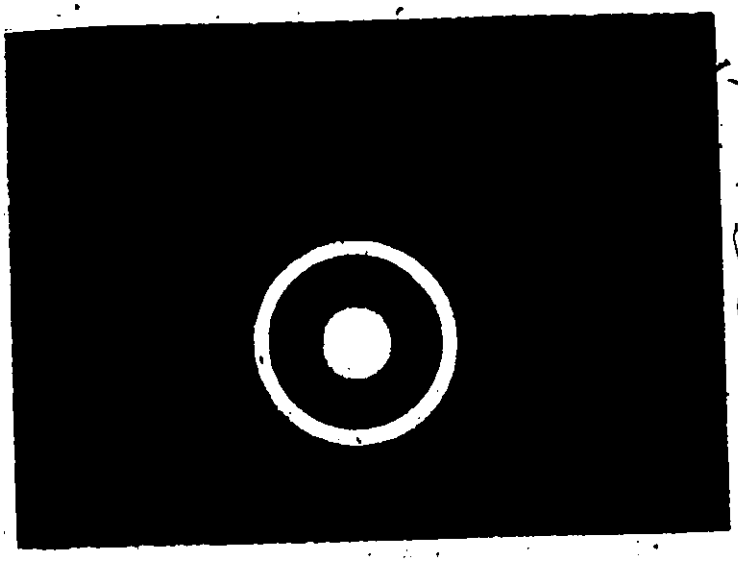

Fig.32 Electron diffraction pattern of a vacuum deposited cobalt film.

Fig.33 Electron micrograph of a heat-treated Co-P film corresponding to Fig.30(b).

vs deposition time of thin metal films deposited electrolessly as indicated in the figure captions. The same sheet resistivity vs deposition time, plotted on the double logarithmic scale and presented in Figs. 36 and 37 have three clear rectilinear regions. In general, the sheet resistivity decreases with increasing deposition time.

In Fig. 38, we present the normalized resistivity at room temperature $\rho(T)/\rho(RT)$ vs annealing temperature. These curves are typical of electroless thin metal films as indicated in the figure captions. On inspection of Fig. 38, we note that the irreversible change of normalized resistivity occurs at a much lower temperature for Co-P and Ni-Co-P films than for Ni-P films. In general, the irreversible change in the resistivity was found to be independent of the pH values of the metalization baths, and of the sodium hypophosphite concentration in the case of Co-P films, i.e. independent of the amount of the co-deposited phosphorus. Furthermore, there is little change as to the shape of the curves with respect to the film thickness.

In Fig. 39, we present a typical curve of normalized resistance $R(T)/R(RT)$ vs annealing temperature of Co-P film up to about 800°K. This experiment was taken in order to find the effect of structure changes upon the resistance, hence the sheet resistivity. The solid arrow in the figure indicates the temperature at which α-Co changes to β-Co in the bulk sample, and the broken arrow indicates the temperature at which Co_2P appears upon heat treatment.

In all cases, it was found that the sheet resistivities measured when the samples were cooled down to room temperature, were essentially

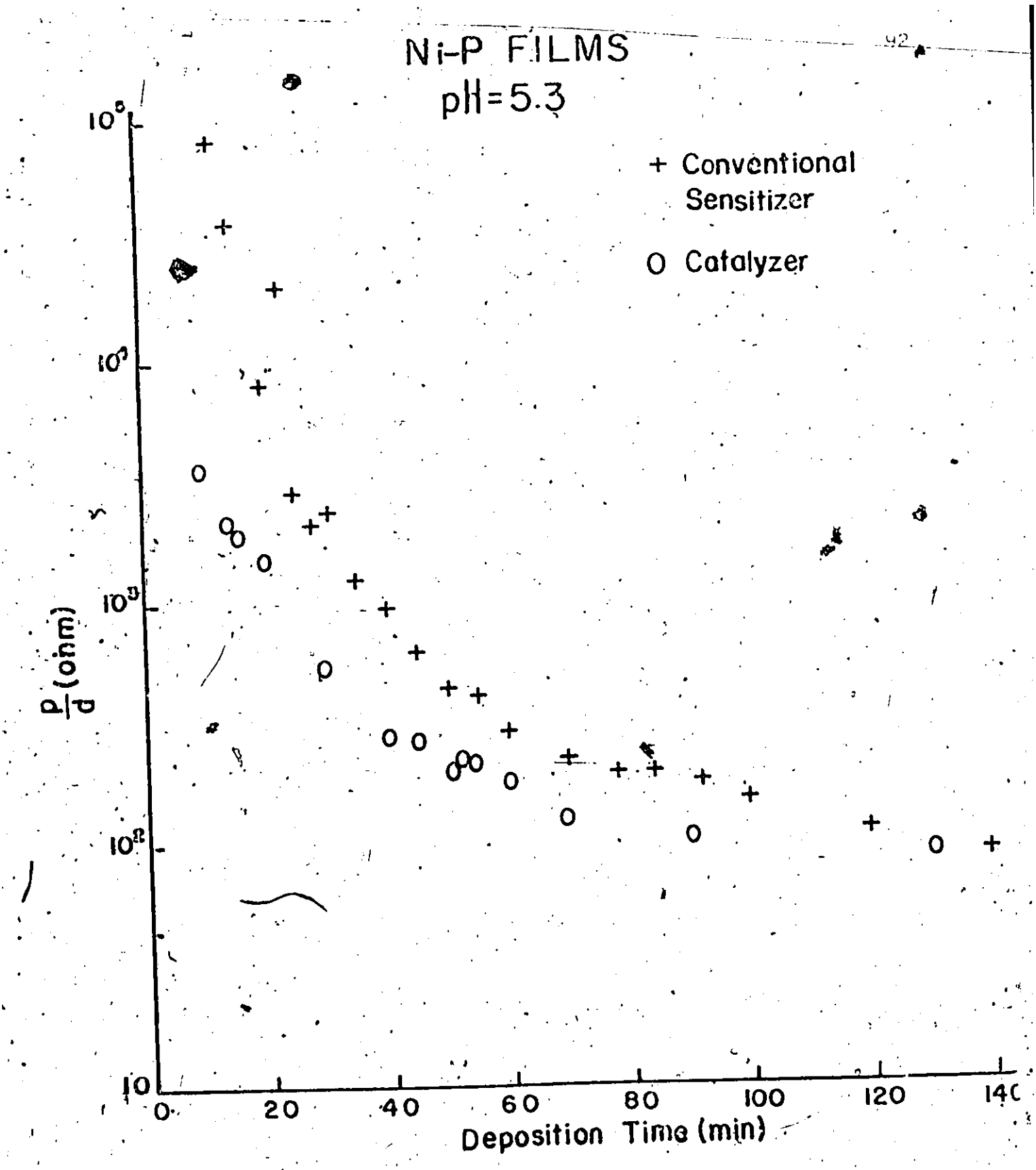

Fig. 4 Sheet resistivity vs deposition time

Ni-Co-P FILMS

(65% Ni)

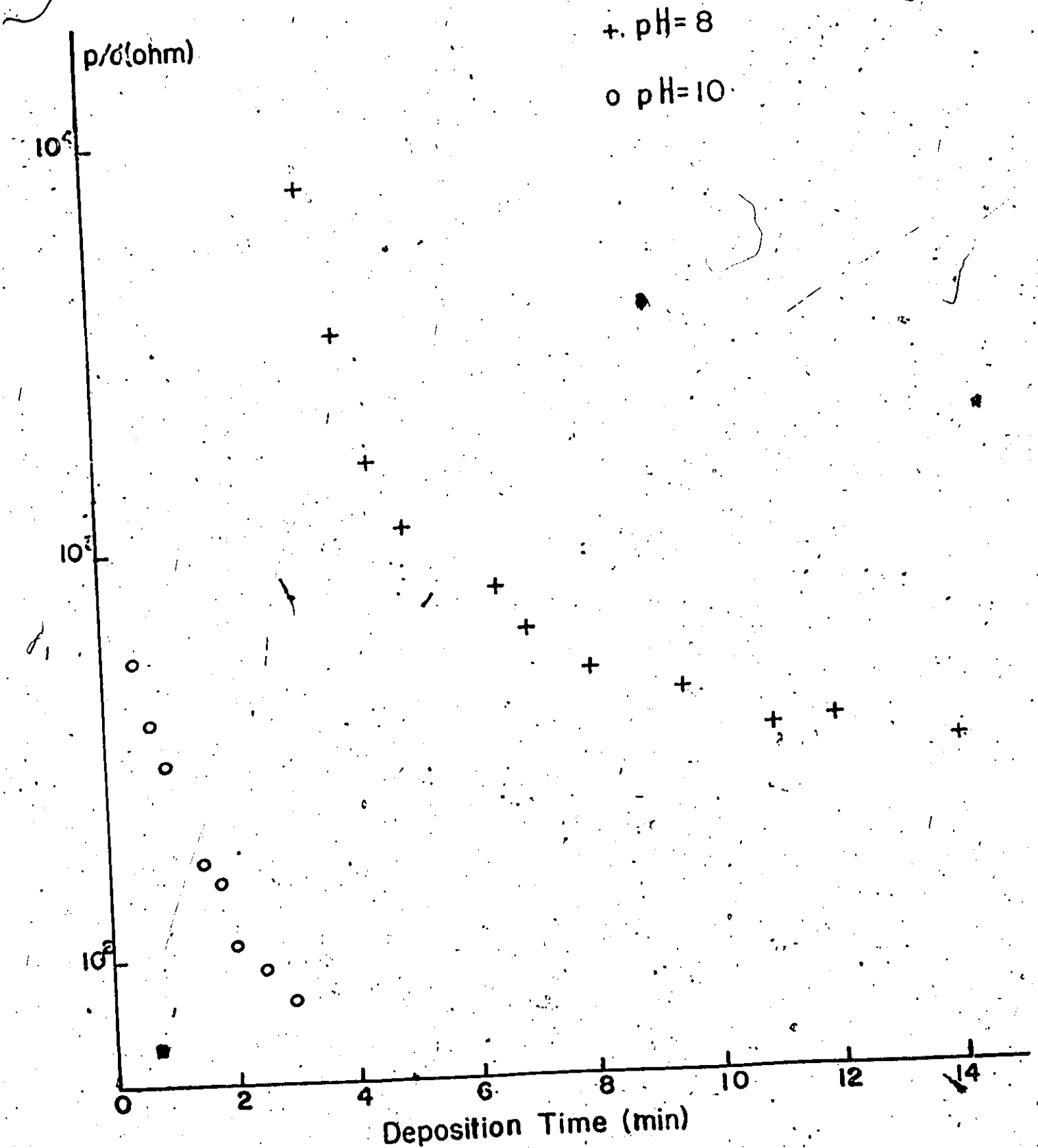

Fig. 4.25 Sheet resistivity vs deposition time

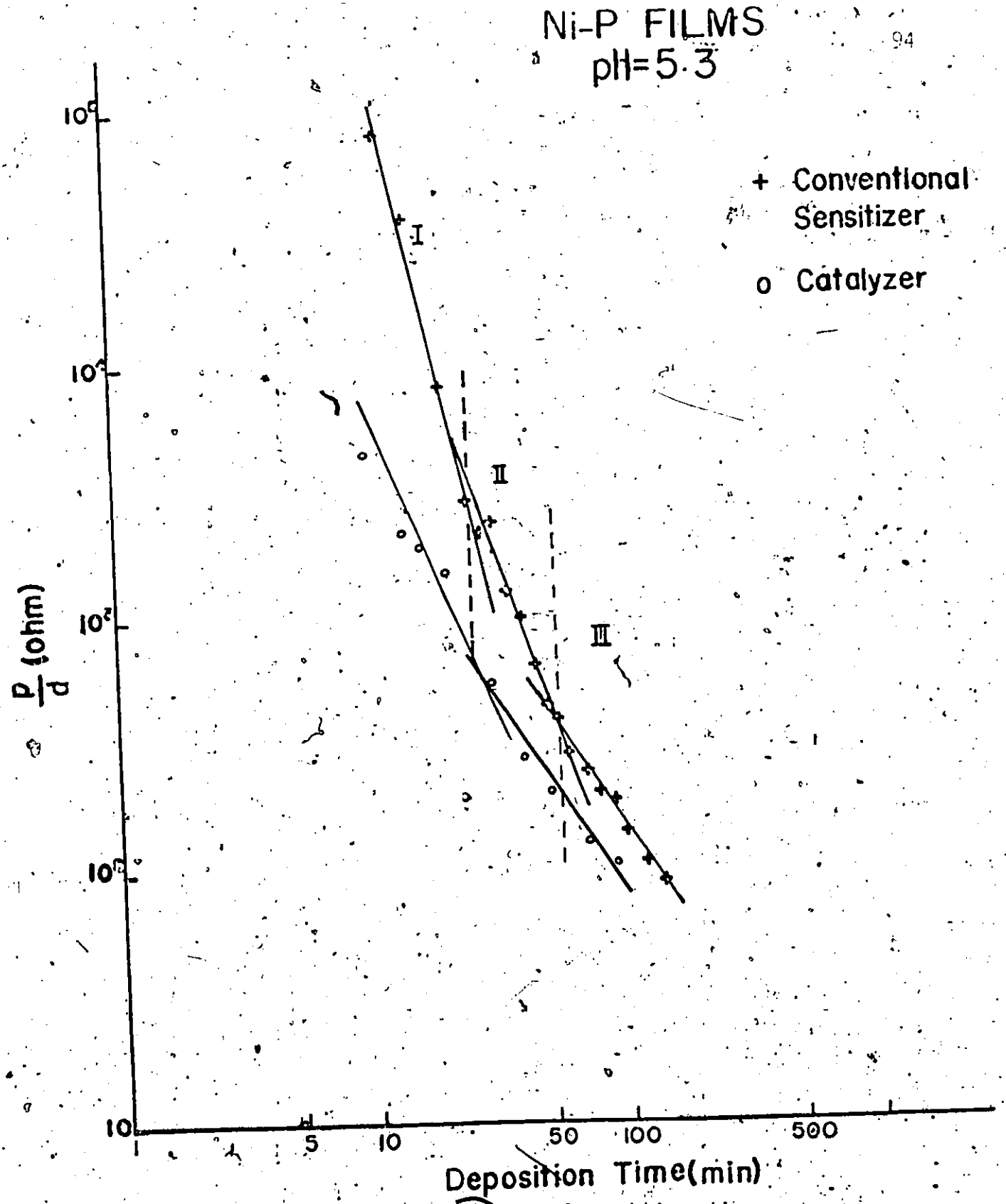

Fig. 36. sheet resistivity vs deposition time

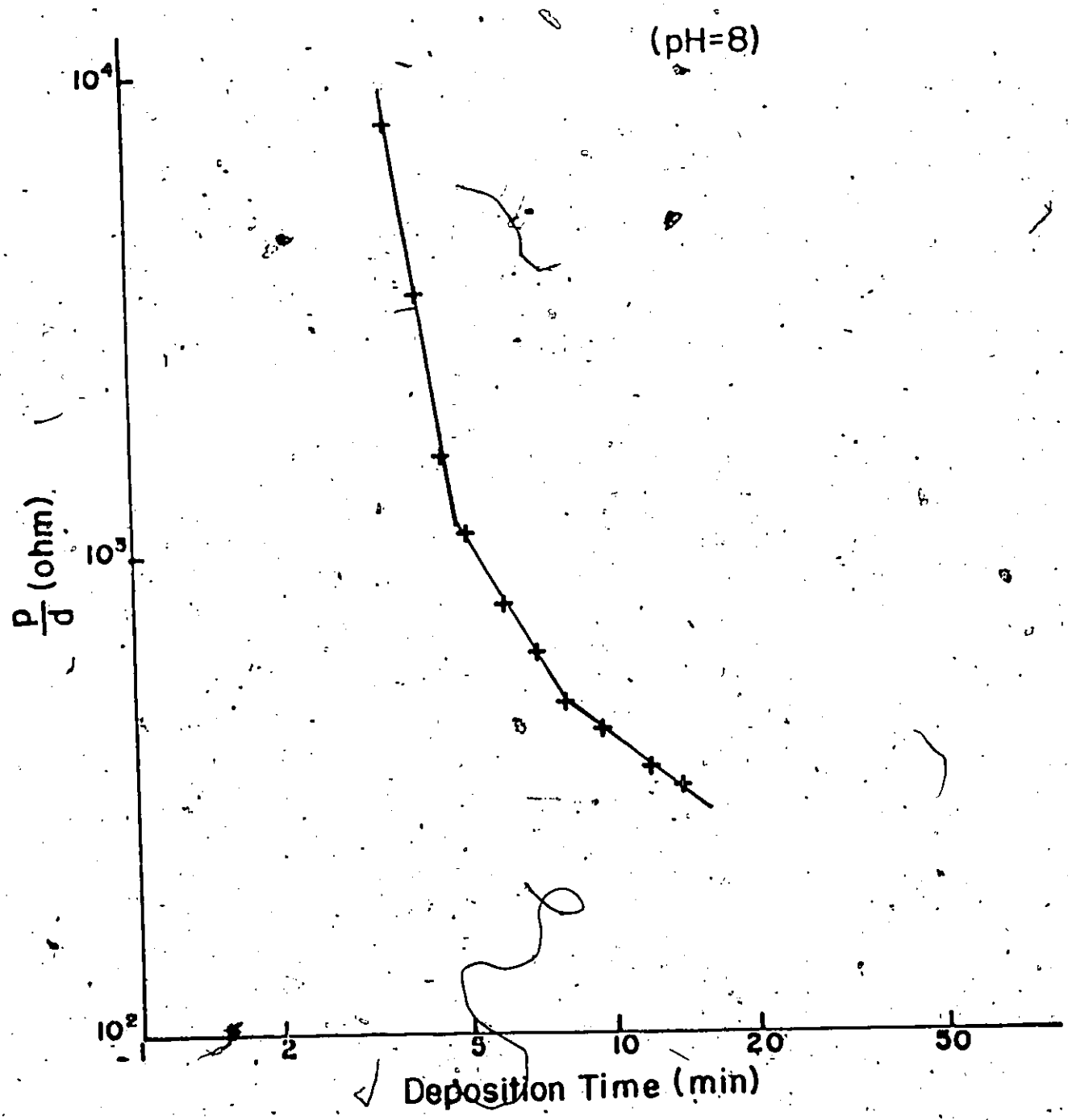

Fig. 9 Sheet resistivity vs deposition time

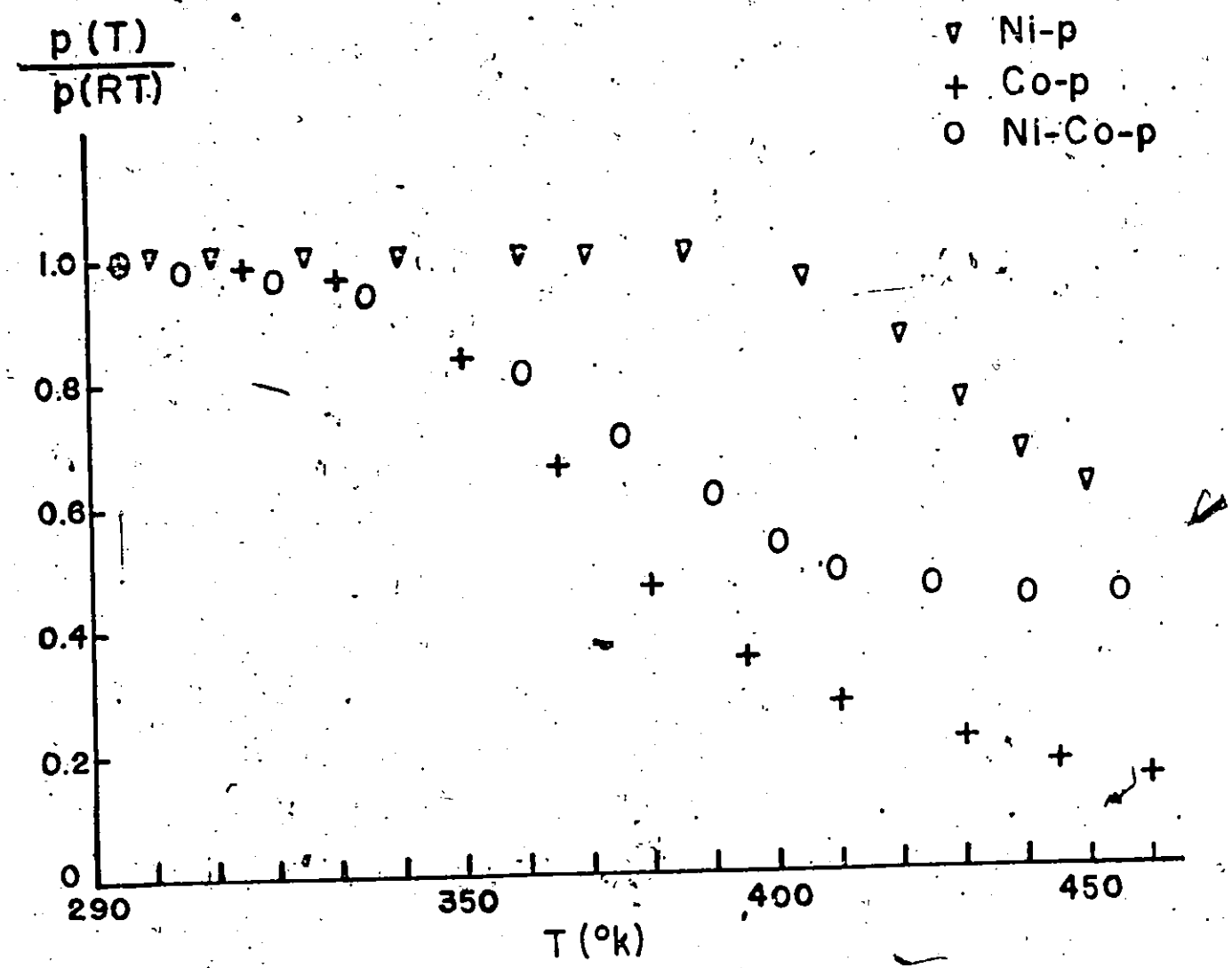

Fig.38 Normalized sheet resistivity vs temperatures

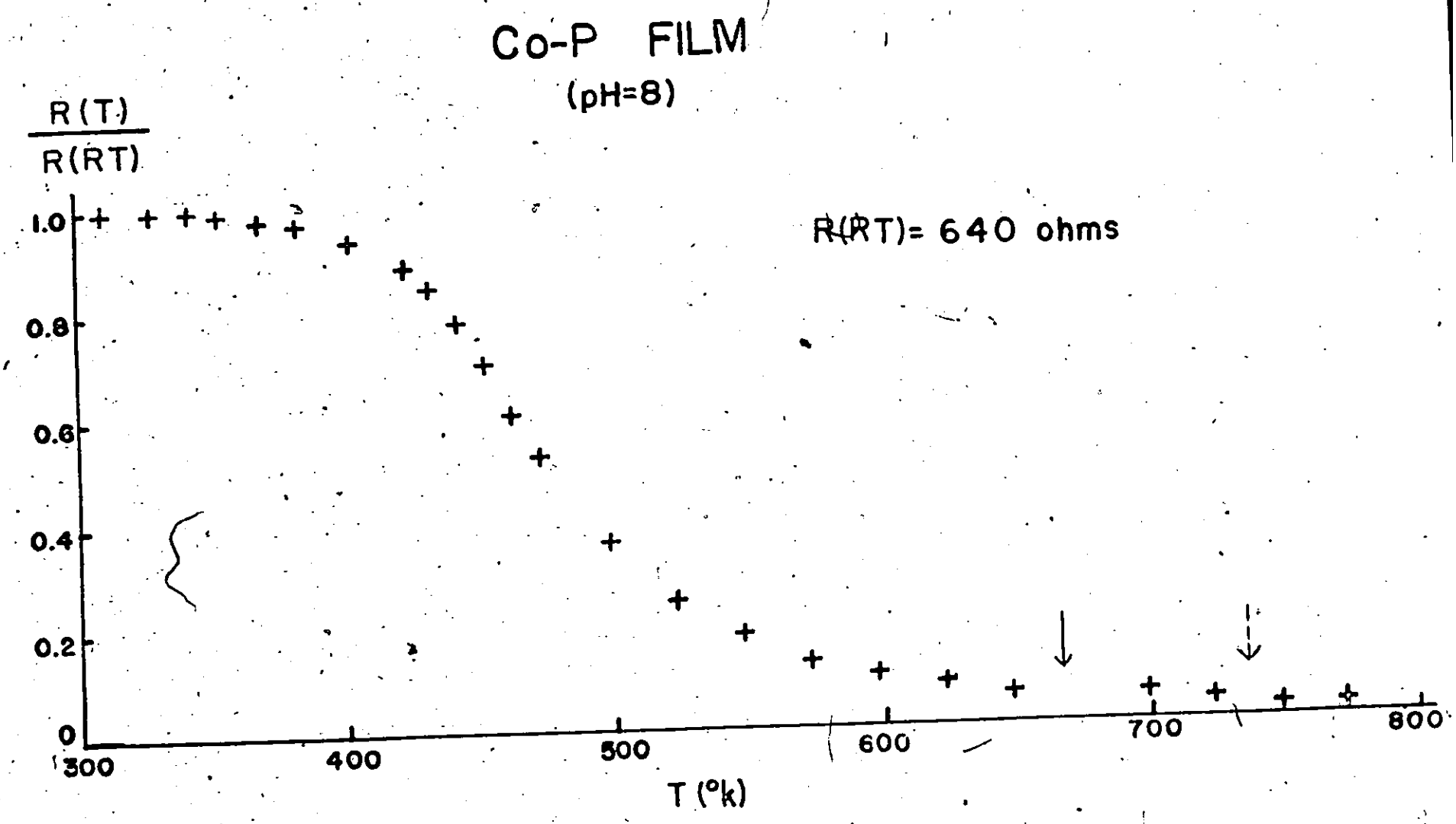

Fig.39 Normalized resistance vs temperatures curve

the same as those measured at the highest temperature attained during the annealing process, except for a small change caused by the temperature coefficient.

2. Temperature Coefficient of Resistivity

No attempt has been made to measure the T.C.R. of as-deposited electroless thin metal films because of the irreversible change in sheet resistivity upon heat treatment. However, after the heat treatment, the change in sheet resistivity upon heating is reversible. In Fig. 40, we present a typical reversible sheet resistivity vs temperature curve for heat treated Co-P films. The T.C.R. was then determined from the slope of the curve.

Table X summarizes a series of T.C.R. of Co-P films. The positive value of T.C.R. indicates that the conduction is of the metallic type.

3. Hall Effects

In Fig. 41, we present the change of Hall emf versus applied magnetic field perpendicular to the sample surface. It is obvious that the change in Hall emf is linear with respect to the applied magnetic field, hence, all the subsequent Hall effect measurements were taken at a fixed applied magnetic field of 6KG.

In Figs. 42-48, we present a plot of Hall mobility, μ_H, and Hall coefficient/thickness, $R_{H/d}$, vs sheet resistivity. Figure 42 is a

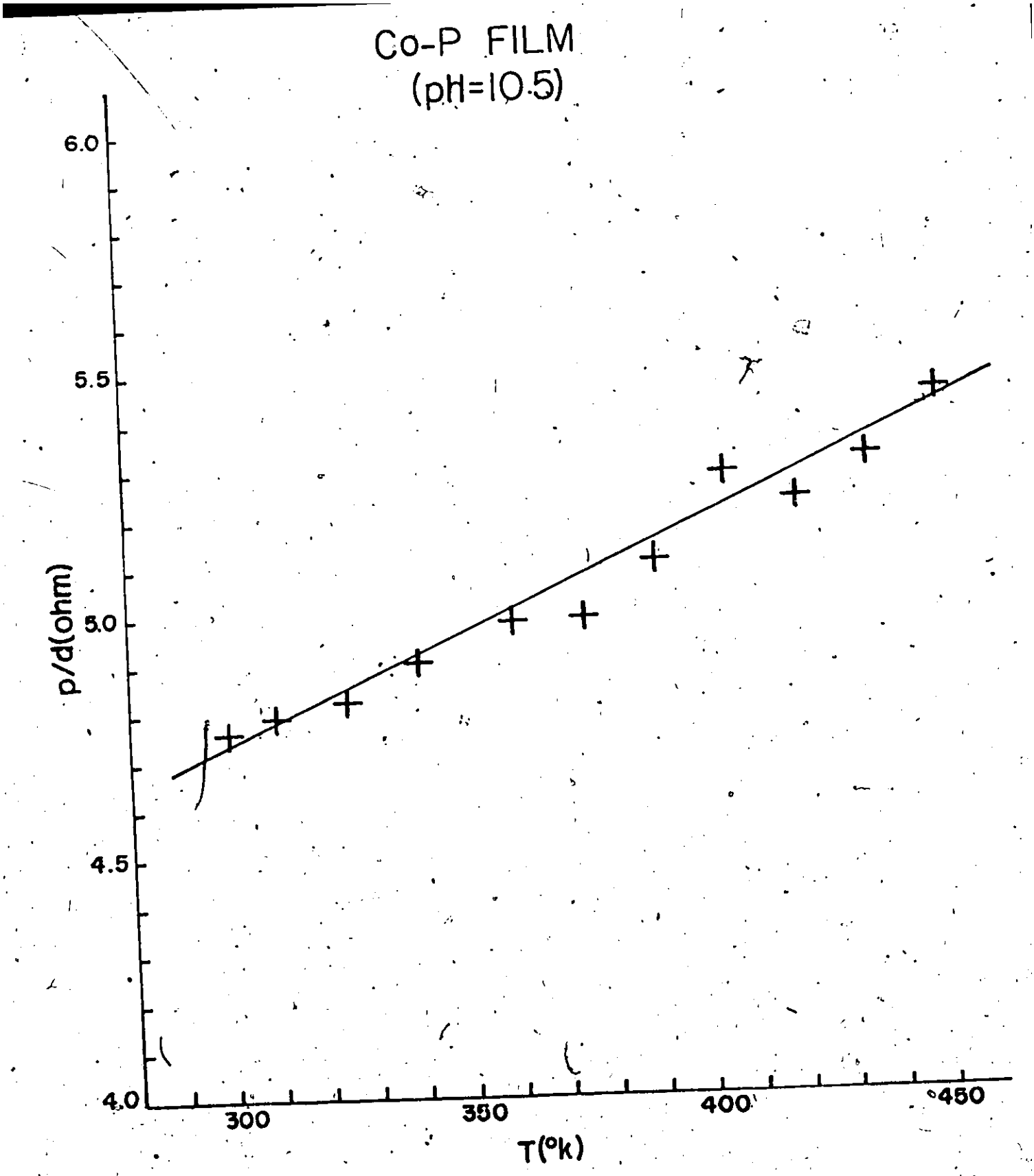

Fig.40 T.C.R. of a typical heat-treated Co-P film

plot of μ_H and R_H/d vs sheet resistivity for as-deposited Ni-Co-P films deposited from an alkaline bath with pH = 8.

TABLE X

T. C. R. of Electroless Co-P Films

pH	hypo. conc.	$\frac{\rho}{d}$ (ohms)	$\alpha = \frac{1}{\rho}\frac{d\rho}{dT}(^\circ K^{-1})$
8.0	25	2275.0	2.91×10^{-3}
8.0	40	96.5	3.65×10^{-3}
9.5	25	16.2	2.37×10^{-3}
9.5	40	85.0	1.87×10^{-3}
10.5	25	250.0	3.64×10^{-3}
10.5	40	68.5	1.98×10^{-3}

The μ_H and R_H/d vs sheet resistivity of as-deposited Ni-Co-P films deposited from an alkaline bath with pH = 10 is given in Fig. 43. Fig. 44 is that of the heat treated Ni-Co-P films corresponding to Fig. 42. Figs. 45 and 46 show the μ_H and R_H/d vs sheet resistivity for as-deposited Co-P films. The pH value of the metalizing bath is indicated in the figure caption. Figs. 47 and 48 are that of the heat treated Co-P films corresponding to Figs. 45 and 46 respectively.

In general, the Hall mobility was found to increase with decreasing sheet resistivity, hence with increasing film thickness. The Hall coefficient/thickness, on the other hand, appears to decrease with decreasing sheet resistivity.

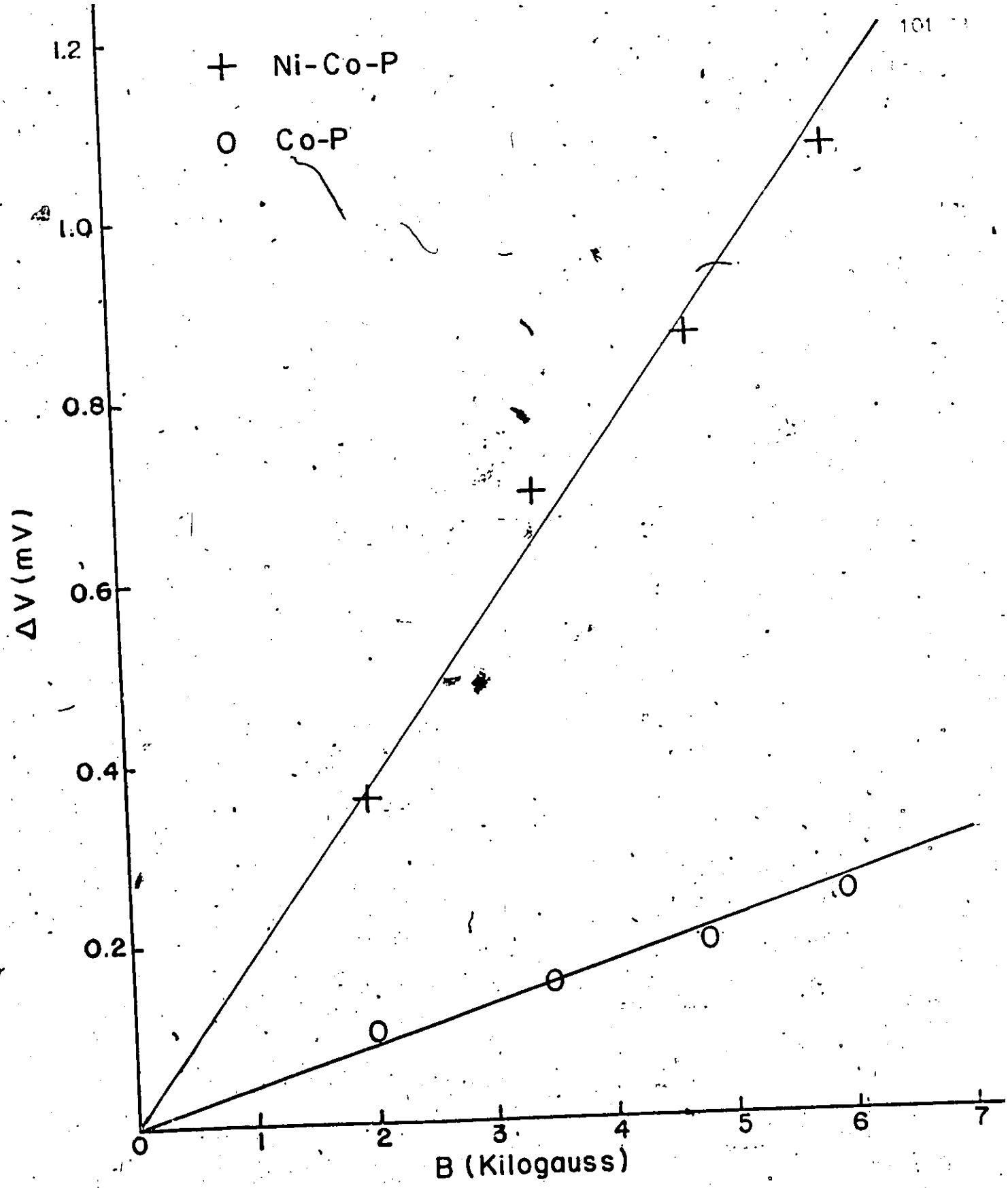

Fig. 41 Hall emf vs applied magnetic field

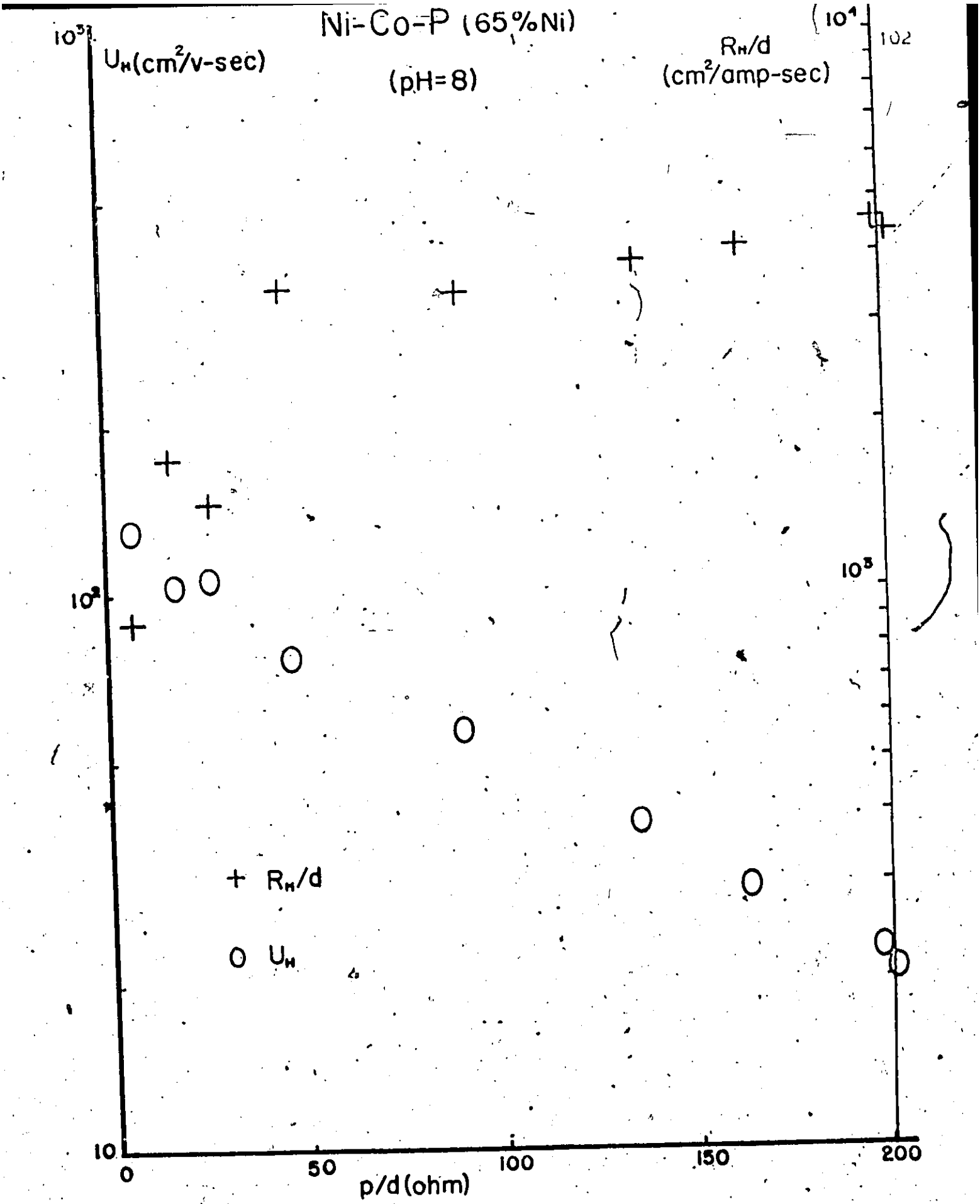

Fig.42 Hall mobility and Hall coefficient/thickness vs sheet resistivity for as-deposited Ni-Co-P

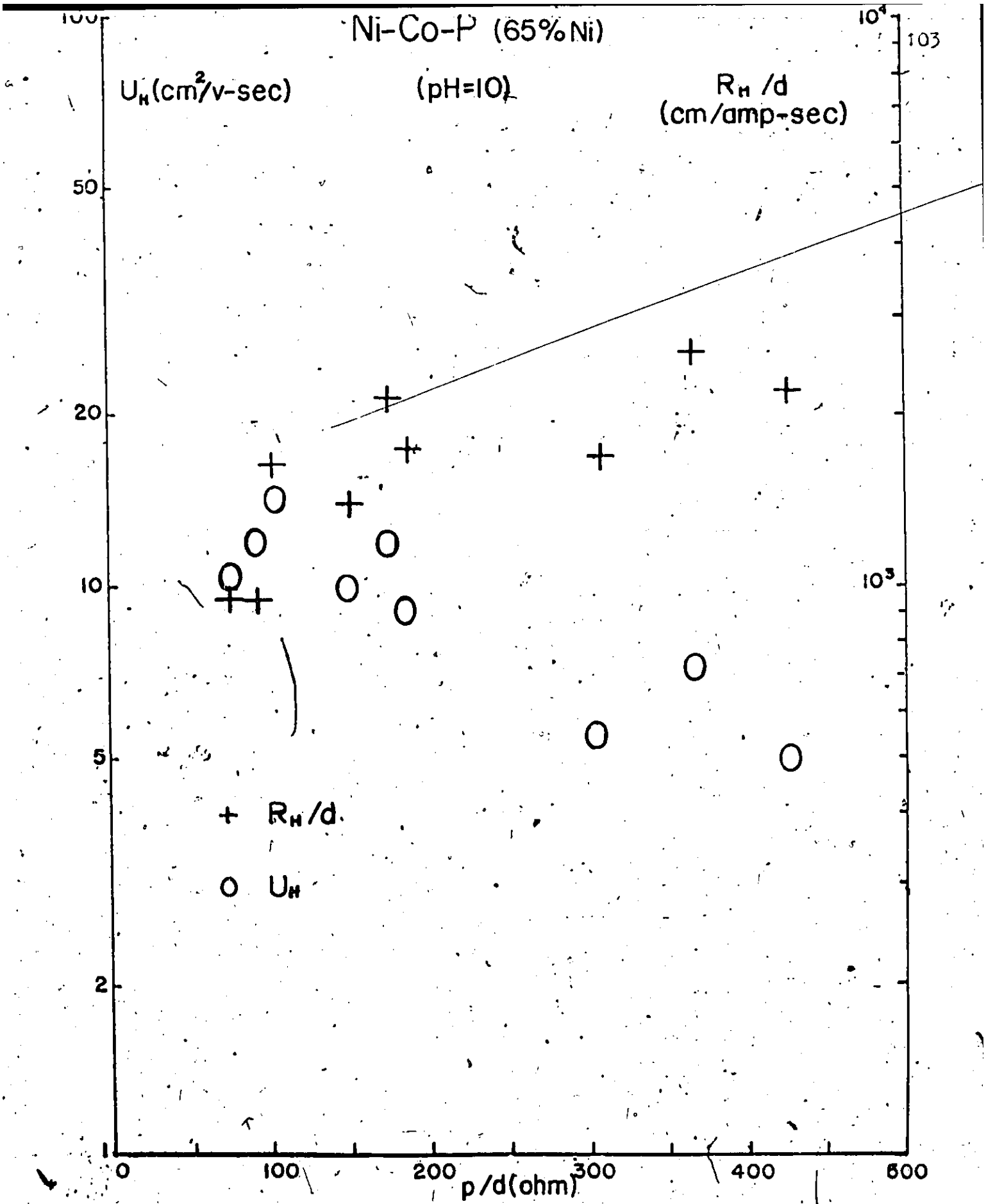

Fig.43. Hall mobility and Hall coefficient/thickness vs sheet resistivity for as-deposited Ni-Co-P

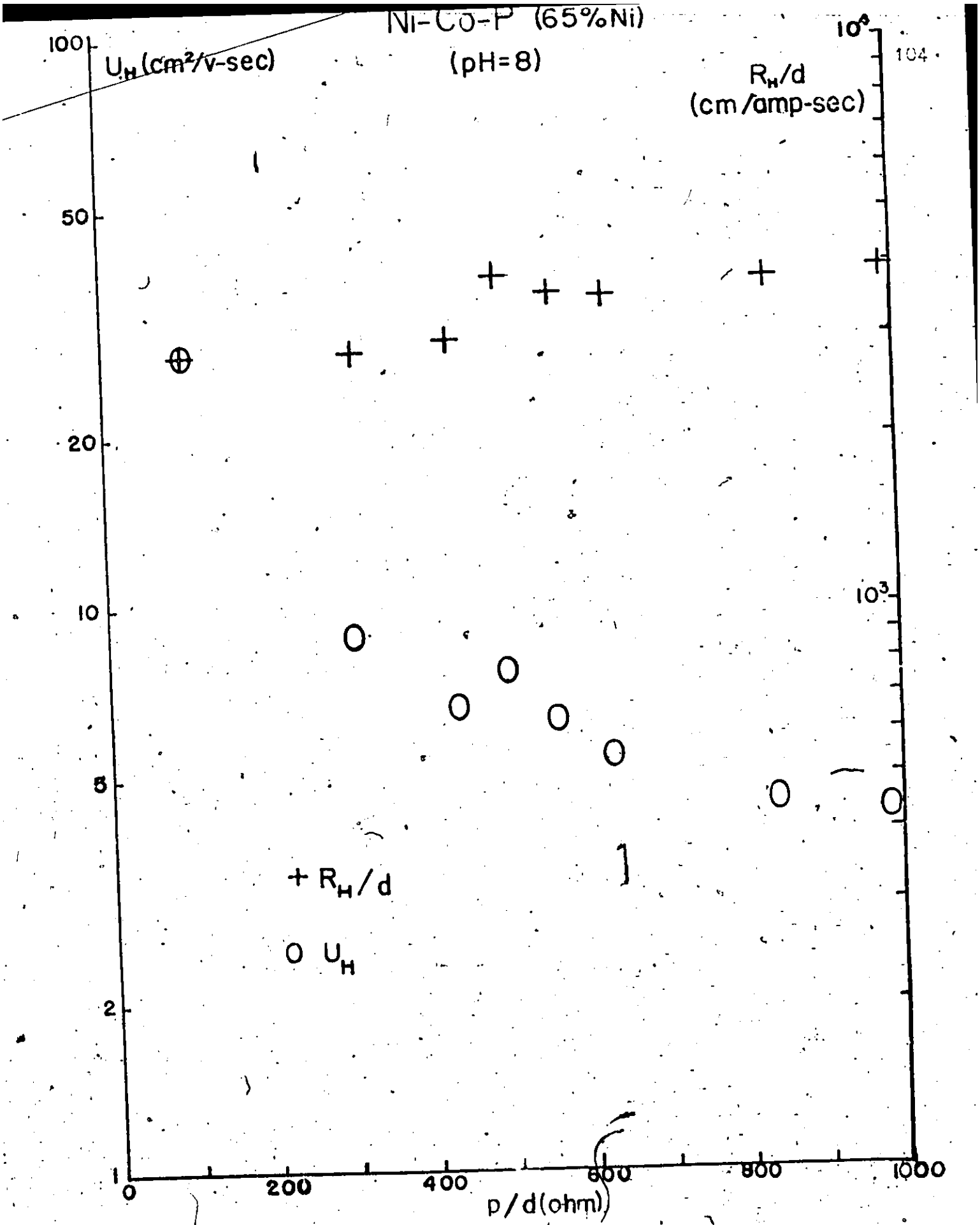

Fig. 44 Hall mobility and Hall coefficient/thickness vs sheet resistivity for heat-treated Ni-Co-P

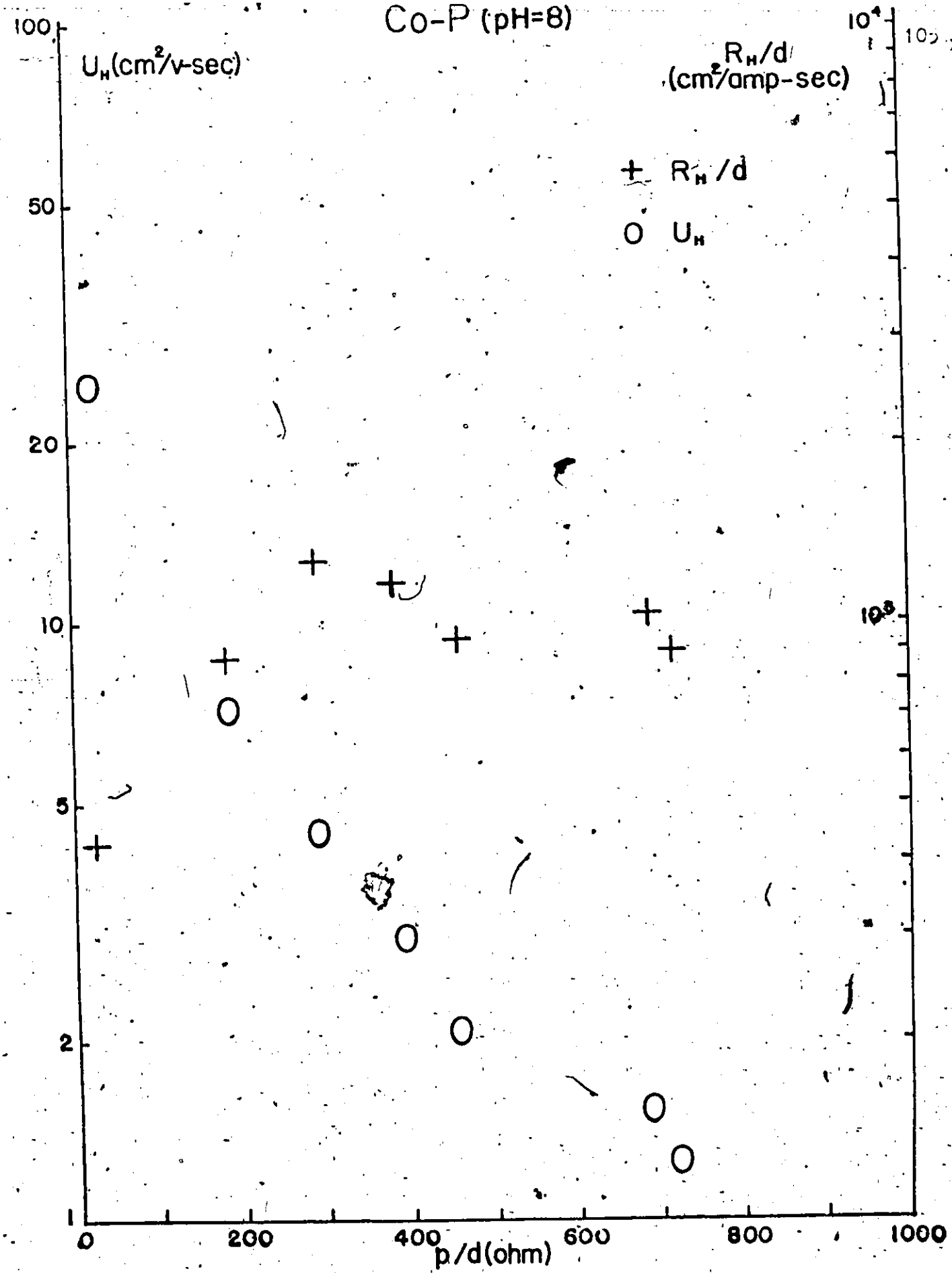

Fig.45 Hall mobility and Hall coefficient/thickness vs sheet resistivity for as-deposited Co-P

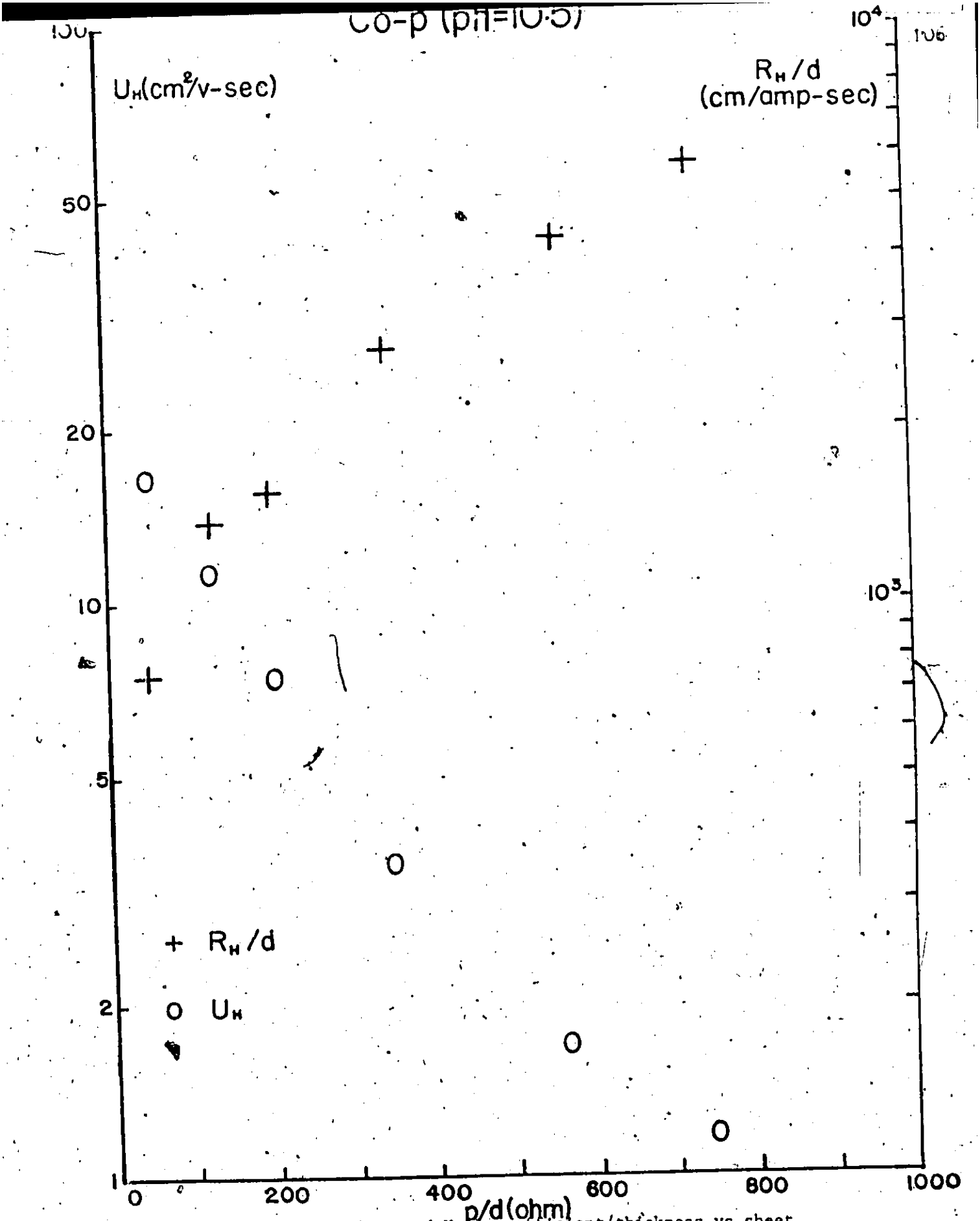

Fig. 46. Hall mobility and Hall coefficient/thickness vs sheet resistivity for as-deposited Co-P

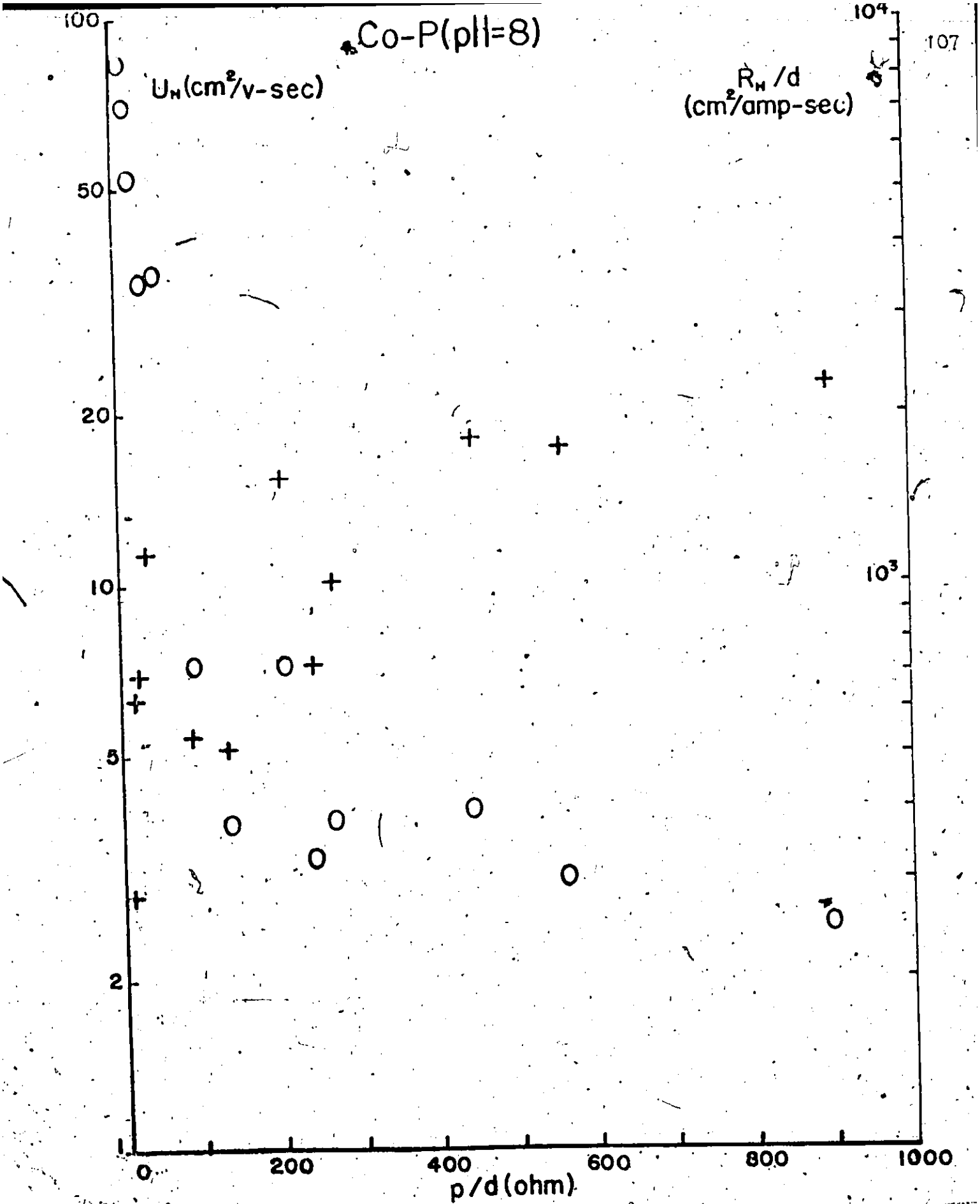

Fig.47 Hall mobility and Hall coefficient/thickness vs sheet resistivity for heat-treated Co-P

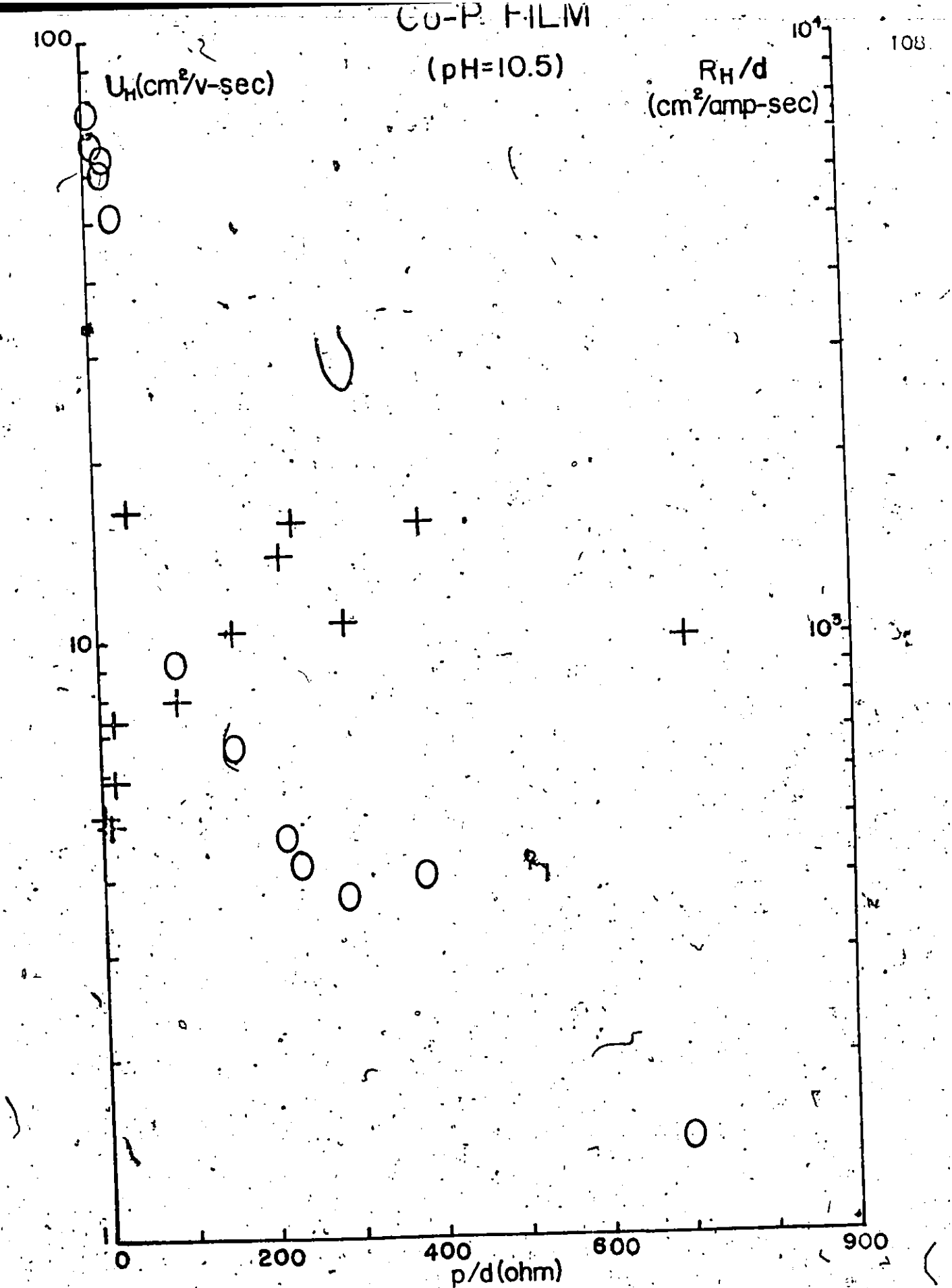

Fig. 48. Hall mobility and Hall coefficient/thickness vs sheet resistivity for heat-treated Co-P

In all cases, the value of Hall mobility can reach a maximum value of more than two times the bulk cobalt value in annealed films with sheet resistivity of about 10 ohms per square, and decrease to a very low value of about 2 cm^2/v-sec in films with sheet resisitivity larger than 500 ohms per square.

Except Fig. 46, no appreciable variation in the Hall coefficient/thickness was found for films with sheet resistivity larger than 200 ohms per square. Below that, the Hall coefficient/thickness decreases rather rapidly with decreasing sheet resistivity. Also, in this region, films with smaller sheet resistivity exhibit a large variation in the values of R_H/d. This is best demonstrated in annealed Co-P films presented in Figs. 47 and 48.

It should be mentioned that the charge carriers in Ni-P films were found to be electrons, while those in Ni-Co-P and Co-P films are holes.

In addition, we summarize in Table XI the values of sheet resistivity and Hall effect of a typical Ni-Co-P film measured under different conditions, and in Table XII the effect of evacuation upon the sheet resistivity of electroless thin metal films. Table XIII summarizes the Hall effect of cobalt films together with the values of bulk cobalt from the literature.

TABLE XI

Typical Sheet Resistivity and Hall Effect of Electroless Ni-Co-P (65% Ni) Measured under Various Conditions

	ρ/d (ohm)	$\frac{R_H}{d}$ (cm^2/amp-sec)	μ_H (cm^2/V-sec)
in Air at RT	100	2.82×10^{-3}	28.2
in vacuum at RT	66	3.21×10^{-3}	48.6
after heat treatment in vacuum	46	3.52×10^{-3}	76.5
after heat treatment in air	46	3.52×10^{-3}	76.5

TABLE XII

Effect of Evacuation upon Sheet Resistivity of Electroless Metal Films

Electroless Metal Films	$\frac{\rho}{d}$ (ohm) in air	$\frac{\rho}{d}$ (ohm) in a vacuum of about 10-5	% decrease in $\frac{\rho}{d}$
Ni-P	70	70	0%
Ni-P	21	20.6	1.9%
Ni-P	7.7	7.2	6.5%
Ni-Co-P	276	225	7.6%
Ni-Co-P	100	66	34%
Ni-Co-P	54	32.4	60%
Co-P	151	95	37%
Co-P	93.1	54	42%
Co-P	27.3	15	45%
Co-P	2.8	1.4	50%

TABLE XIII

Hall Effects of Bulk Cobalt, Cobalt Films and Electroless Co-P Films

Films	Hall coefficient (cm^2/amp-sec)	Hall mobility (cm^2/v-sec)
Bulk [147]	24×10^{-5}	38.4
Co-film [145]+	$R_1 = 6 \times 10^{-4}$	50
	$R_o = -1.4 \times 10^{-6}$	1.2
Co-P (fresh) film*+	21×10^{-4}	25
Co-P (annealed) film*+	30×10^{-4}	80
Evaporated Co film*+	27×10^{-4}	32.9

*present work.

+film thickness about 500 Å

CHAPTER 4

INTERPRETATION OF EXPERIMENTAL RESULTS AND DISCUSSIONS

(I) Structure of Pretreated Surface

1. Conventional Sensitizers

In this section we shall include the effect of u.v. irradiation on the pretreated surfaces in addition to the structures of the pretreated surfaces.

(A) Structure

The conventional sensitizer system has been studied to some extent by various authors [3-8, 20, 21, 23]. There is, however, a seeming lack of agreement among their results. Some [5,7] found that the product after the activation step is f.c.c. palladium, while others found that it is either amorphous [8] or a tin-palladium complex [23]. The results of this work will show that the lack of agreement might probably be due to the different substrates that have been used.

In the present studies, the product of the sensitization process appears to consist of particles of approximately 20 Å diameter agglomerated into dense clumps an order of magnitude or so larger. The clumps themselves are randomly distributed on the surface in agreement with some previous observations [5,7]. The activated surface shows particles of about 50 Å in size, some tendency for cluster for-

mation is evident. It has been presumed [5,7,20] that the product after the activation step is a deposit of fine grained metallic palladium in support of the redox reaction mechanism [2,4,5,20,21]. To this extent, one might expect however a more distinctive pattern from the sensitized and activated surface since a palladium layer would be expected, in accordance with Bravais' law, to form with the closed packed planes [111] parallel to the substrate surface. Such is not the case in the present work, as can be seen in the diffraction pattern of Fig. 21(b) which is amorphous in character.

The electron diffraction pattern for the sensitized surface seems to be characteristic of hydrated stannous oxide (SnO_2) in consistence with the model proposed by Cohen et al [2]. It is, however, rather difficult to attribute the diffuse electron diffraction pattern of the sensitized and activated surface to any one symmetry or chemical compound.

It should be noted that three major experimental difficulties are inherent in the quantitative interpretation of the electron diffraction patterns in this instance.

(i) the amount of material present on the surface is very small, and consequently, the intensity of the patterns is rather low,

(ii) the size of the "crystallites" present is small, giving a pattern with broad rings, and

(iii) there is also the possibility of dehydration of the "hydrous Sn polymer" by the vacuum and/or irradiation of the electron beam in the electron microscope.

(B) The effect of u.v. irradiation on the preteated surfaces

Ultraviolet irradiation has been assumed [2] to inhibit the

metal growth by simply oxidizing the Sn^{+2} to Sn^{+4} prior to the activation bath, hence preventing the formation of a palladium layer. Working with Ni and Co, we have found that u.v. light is effective in inhibiting the electroless deposition even if it is applied after activation. This, we shall show, renders the model of Cohen et al [2] rather incomplete. Based on the results presented in Fig. 22, we believe that an explanation of the influence of u.v. light must also include crystalline structure changes. As a result of those changes electroless deposition becomes impossible. While more experimental work is needed before a complete model can be drawn, one can argue in the following qualitative way.

The effect of irradiation on the diffraction patterns of both the sensitized and activated layer is to increase the degree of crystallization. This is evident by comparing the diffraction patterns of Fig. 19(a) with Fig. 22(a) and Fig. 21(a) with Fig. 22(b). This is a consistent trend which was observed in many samples prepared under various conditions. In the case of the sensitized layer, this may well be associated with the oxidation of a divalent tin compound to form SnO_2, and it is also clear that the degree of crystallinity is also increased by the irradiation. The situation is similar for the activated layer. It is harder to envisage a chemical change in metallic palladium resulting from irradiation, although, it is tempting to suggest an oxidation to a divalent state by anology with the oxidation of the tin compound. In any event, again a higher degree of crystallization definitely results from the irradiation.

Based on the results presented above, we can conclude that the redox reaction between tin II and palladium II is not a prerequisite for the successful results of electroless plating. The substrate used also plays a significant role in the chemistry of the catalyzation process.

Recently, it has been found [104] that under certain conditions, copper deposition can also be inhibited by u.v. irradiation after activation. Furthermore, positive or negative images of the photomask can be selectively deposited according to whether the u.v. irradiation is applied before or after the activation rinse step.

2. Improved Sensitizers

The improved sensitizer system has been developed recently by Feldstein and co-workers [22, 24-28] to achieve a better electroless plating performance on hydrophobic surfaces. Visual examination of thin metal films deposited on a hydrophobic surface also shows a greater degree of uniformity in comparison to films deposited using conventional sensitizer.

Specifically, the improved sensitizer is obtained through the incorporation of aged stannic chloric solutions. It is believed [27] that a colloidal component of tin IV is formed during the aging process. As a result, the aged stannic chloride provides a new path for the adsorption of stannous ion on the hydrophobic surface. It has also been found that [24,26], the aged stannic chloride solution may

either be added to conventional sensitizer or used in a separate step prior to the immersion in conventional tin sensitizer. In either case, the same results were obtained by examining the uniformity of metallic coverage, by measuring the resulting surface through contact angle measurements, and by monitoring the concentration of active components on the substrate surface employing radio chemical adsorption technique.

In the present study, a series of electron micrographs are used to demonstrate the distribution of the active catalytic sites, and the nucleation and growth of the electroless deposits on Formvar surfaces activated using improved sensitizers.

Comparison of Fig. 18(a) and (b) reveals a denser and a more uniform distribution of particles and clusters. The density of particles resulting from the improved procedure is about 10^{12} particles/cm^2, an order of magnitude larger than that from conventional tin sensitizer. The same result can also be obtained if 10 c.c./ℓ isopropyl alcohol is added to the conventional tin sensitizer [6]. In the latter, it is believed that the addition of isopropyl alcohol improves the wetting performance of the Formvar surface.

Identical electron micrographic results were obtained using the improved procedure whether the aged stannic chloride component was used prior to the conventional sensitizer or mixed along with it. This result, i.e. that one may use the aged stannic chloride prior to, or together with the conventional tin sensitizer, is consistent

also with previous observations[22,24,27]. It is also consistent with the model proposed [28] to account for sensitization. In addition, it has also been observed that when dilute conventional sensitizer solutions were aged at room temperature for a week, they serve as effective sensitizing baths, rendering results similar to Fig. 18(b).

Although the basic particles of Fig. 18(b) are about 20 Å in diameter, it should be apparent that the improved sensitizer medium results in a decreased tendency for cluster formation. In fact, the clusters formed through the conventional approach are a few times larger in comparison with those obtained using the improved procedure. The results of Fig. 18(b) were independent of the tin II concentrations used.

The surface product obtained by the improved method exhibits a diffraction pattern markedly different from that obtained using conventional tin sensitizer. While it is difficult to attribute the diffraction pattern to any crystalline structure, it may well be argued that the chemical species responsible for this pattern is a polymeric substance of the type [27,29].

$$(HO)_3\text{-}Sn[OSn\text{-}(OH)_2]_n\text{-}OH$$

or

$$(HO)_2\text{-}Sn\text{-}[O_2Sn]_n\text{-}(OH)_2$$

where n is an integer reflecting the extent of polymerization. Such a material is believed to be formed in a slow transformation of an

α-stannic acid to a β-stannic acid during the aging process due to a water elimination reaction.

The product of the improved procedure at the conclusion of the activation step also exhibits a denser distribution in comparison with the conventional tin sensitizer. Some tendency for clustering is evident. Here, too, the diffraction pattern is characteristic of an amorphous material.

From the present results, it is clear that the visual observation of more homogeneous metallic distribution is attributed to a more homogeneous distribution of sensitizer component on a microscopic scale. It also results in a finer and denser metallic end product (see below, also ref. 18; Figs. 3 and 4).

3. Catalytic Solutions

In the current investigation, it was decided to examine the dielectric surface at the different stages of pretreatment, including the early stages of nucleation and growth. This investigation was especially intended to provide further insight into various debated aspects of this system. Specifically:

(i) the makeup of the solution, whether it is a palladium colloidal or rather a tin II and Pd II ionic complex,

(ii) the role of the accelerator solution, and its chemical nature, and

(iii) the chemical nature of the catalytic surface prior to plating.

From Figs. 18(c) and 20(c), it should be apparent that the distribution of active component(s) is rather homogeneous. Inspection of Fig. 18(c) shows a density of active sites of approximately 10^{12} centers/cm^2. These centers are composed of particles of approximately 20 Å in size. Comparison of the particle distribution to Fig. 18(a) shows a marked difference, however, comparison of this distribution to Fig. 18(b) shows a familiar similarity.

The diffraction pattern of Fig. 19(c), however, shows a marked difference from that of Fig. 19(a) and (b). Here, the product after the catalyzing stage is amorphous in character. No attempt has been made to identify this product. Others[34] believed to be a tin II and Pd II ionic complex rather than a palladium colloid. This point would be made clear when the function of the accelerator solution and its chemical nature is studied. This result, i.e. that the product after the post catalyst rinse is a tin II and Pd II complex is also consistent with Rantell and Holtzman's [34] findings.

After the post-acceleration rinse, see Fig. 20(c), a tendency for cluster formation is evident. By contrast to the cluster formation in conventional sensitizer or improved sensitizer, in the current system, the clusters seem to form in a worm-like fashion. This tendency seems to be preserved as well in the early stages of the metallic end product as seen in Fig. 25(c) [also ref. 6, Fig. 1c].

The electron diffraction pattern of Fig. 21(c) shows that the product after the acceleration step is crystallized. This product can

be easily indexed as f.c.c. with lattice parameters closely matching those of Pd_3Sn (see Table VI). It should be noted that Pd_3Sn is the only Pd-Sn compound known to crystallize in f.c.c. form [105].

Comparison of the current experimental results to those derived from the literature [105] for Pd_3Sn, offers a convincing proof that the noted deviation of the order of one percent could be best accounted for by the size of the crystallites present affecting the definition of the diffraction rings. The present finding is also in good agreement with conclusions made by Cohen et al [32] using Mössbauer spectroscopy. These conclusions, however, are not in agreement with recent results by Rantell and Holtzman [34]. In their work, it was concluded that metallic palladium is present at the conclusion of the acceleration step, suggesting a redox reaction between Sn II and Pd II. This lack of agreement was initially conceived as being due to possible difference in experimental techniques.

Rantell et al used etched ABS as substrate, while we have used Formvar deposited on glass. Secondly, the chemical composition of both the catalyzer and the accelerator solutions was different.

In order to verify the results, the following additional experiment was therefore carried out. Samples were prepared using all four possible combinations of the Shipley's 9F and 19F and Rantell's solutions. Essentially identical results were obtained, although the distribution of particles in the deposit is affected by the nature of the accelerator, its chemical composition is not. No evidence of metallic palladium can be observed. It is possible that the deposits

obtained with Rantell's solution contain insufficient amount of palladium to be observable by electron diffraction. It is also conceivable that the chemical nature of the substrate plays a role in the Sn II and Pd II interaction.

Finally, we should note that no metallic deposit can be obtained on glass when pretreated by catalytic solutions and that best plating results on surfaces other than glass were obtained whenever Pd_3Sn is present on the pretreated surface [36].

(II) Structures of Electroless Metal Films

1. Electroless Ni-P Films

Ni-P alloy can be deposited in the form of thin films by electrodeposition [106,107], vapour quenching [108] and electroless deposition [1].

Under certain preparation conditions, electrodeposited Ni-P films can be amorphous in character [106]. The analysis of such amorphous structure using radial distribution functions (rdf) reveals that amorphous Ni-P deposits have a better defined short-range order than that observed in liquid noble metals above their melting point, and that a dense random packing of equal size hard spheres would be an appropriate structure model.

Because of their practical applications, Ni-P films deposited electrolessly have been the subject of numerous investigations [6, 108, 115].

Goldstein et al [109] deposited films having phosphous content ranging from 7 to 10 w/o on base metals at 80°C. Harton and Schlesinger [6] deposited films having 16 w/o phosphorus from an acidic bath with pH = 5.3 on Formvar at room temperature. In both cases it was concluded that the structure of as-deposited Ni-P is "liquid-like". By this one means a metastable solid solution of phosphorus in nickel system. The same conclusion has been reached by Zielilki et al [110], Albert et al [108] and Moiseev [114]. On the other hand, Dixmier et al. [112,113], with phosphorus content ranging from 7-10 w/o have concluded that the structure of as-deposited Ni-P is a heavily faulted f.c.c.-h.c.p. two phased crystal with the phosphorus atoms included interstitially in the h.c.p. nickel layer. Graham et al [114] and Kotel'nikov et al [115] have reported that the as-deposited Ni-P from an alkaline bath can be either amorphous or crystalline in structure. The broadening of the diffraction rings of an amorphous Ni-P deposite is most probably due to the decrease in crystal size of the deposit. The result of this work shows that the structure of as-deposited Ni-P film is dependent on the pH value of the metalization bath.

In the present investigation, we have been able to deposit Ni-P films from different pretreatment solutions. The aim of this process is to find if the structure of as-deposited Ni-P will be affected by the pretreatment solutions.

Comparison of Fig. 23 reveals no marked change in morphology of the Ni-P deposits, except that the Ni-P islands are much smaller

in size if activated using catalytic solutions. The Ni-P islands are almost spherical in shape, separated by "channels". It is difficult to identify the materials that compose the "channel", however, it may be argued that it is composed of hydrogen and/or phosphorus. Unlike the growth mechanism in vacuum deposited metal films [44], no evidence of coalescence growth has ever been observed. Instead, the Ni-P islands are first formed on the nucleation sites and grow in size until they touch one another in agreement with previous results [6].

The diffraction patterns of Fig. (24) feature two broad rings corresponding to interplanar separation of $d_1 = 2.078$ Å and $d_2 = 1.198$ Å, respectively. The displacement of the first ring relative to the center of the Ni(111) peak (with $d_{111} = 2.035$ Å) indicates that the differences of the rings in the pattern is due not only to a high degree of dispersion of Ni-P deposite but also to the changes in its structure. Note that the difference between d_1 and d_{111} amounts to over 2%, well above the experimental error of 1% in accuracy. Since only a change in distance between atoms and coordination number will alter the peak of the diffracted electron beam, it is thus concluded the structure of as-deposited Ni-P from an acidic bath is "liquid-like" in agreement with the results of Marton and Schlesinger [6].

It should be mentioned that materials termed amorphous can have one of many possible structures. There exist two limiting cases: (i) the microcrystallite with a grain size of the order of one to two unit cells [116], and (ii) continuous random models [117, 118] which are "liquid-like".

It can also be argued that, if the Ni-P islands in films are single crystals, but are small to cause proper diffraction pattern, then the dark field micrograph taken at the first broad ring would reveal numerous diffraction spots. If, however, the islands are amorphous, no diffraction spots would be observed. The dark field micrograph of Fig. 27(a) confirms the latter case.

Next, "passing" from Fig. 25(a) to 25(c), the phosphorus content in the electroless Ni-P film decreases. This is due to the fact that the amount of phosphorus incorporated into the film increases as the pH of the metalizing bath decreases (see equation 12). Here, we noted also that the higher the pH value of the bath, the faster is the rate of deposition. While the electron micrographs reveal no marked changes, the diffraction patterns in Fig. 26 clearly demonstrate a change of degree of crystallinity as the pH value is increased. In order to ensure that the change in crystallinity is due to the change of pH value, thus the phosphorus content, and is not due to the change of deposition rate, we further investigated Ni-P films deposited from low pH baths at elevated temperature. It was found that even though the deposition rate is increased by an order, the microstructure is not affected. By assuming the as-deposited Ni-P films to be a solid solution of phosphorus in a very fine polycrystalline nickel system, it is not unreasonable to expect that decreasing the phosphorus content should result in an increase in the average size of crystallites. This is not immediately observable by comparing the electron micrographs in Fig. 25, the electron diffraction patterns in Fig. 26 dem-

onstrate this point clearly. Also, the dark field micrograph of Fig. 27(b) indicates that the Ni-P films deposited from low pH value alkaline bath are amorphous in the sense of microcrystallites. Finally, assuming in Fig. 25(b) a f.c.c. symmetry, the lattice constant thus calculated (see Table VII) for the Ni-P films is a_o = 3.554 Å. While this number can be considered somewhat too large (ordinary nickel has a lattice constant of a_o = 3.523 Å), it might be an indication of a "strained" f.c.c. lattice [108].

By comparing the electron micrographs of Figs. (23) and (25), we note that the islands in Ni-P deposited from an alkaline bath are no longer spherical in shape, and the "channels" that separate the islands are less obvious. The latter is best demonstrated in Fig. 25 (c). This is believed to be due to a change of the degree of the crystallinity. The worm-like growth pattern of Fig. 25(c) is, as mentioned previously, inherited from the catalytic pretreatment steps. Nonetheless, a worm-like growth pattern has been observed [119,120] previously for vacuum deposited nickel films on a single crystal rock salt substrate at elevated temperature, and for electroless Co-P films on Formvar at elevated temperature [8]. This was attributed to the magnetic force, which, present between existing relatively large aggregates, spontaneously magnetizes the newly forming crystallites. At the present stage of knowledge, it is difficult to give an appropriate explanation to the worm-like growth pattern in our case, and further work on the chemistry of the catalytic solutions is required to clarify this point.

2. Electroless Ni-Co-P Films

A few research reports only have been published in connection with the Ni-Co-P thin film system. Vacuum evaporated Co-Ni films have been found [121] to be h.c.p. with a (111) fibre structure occuring at the film surface. On the other hand, electroless Ni-Co-P films have been reported to have a f.c.c. structure for low cobalt concentration and a h.c.p. structure for high cobalt concentration [122].

The present investigation will show that, like Ni-P deposits, the structure of electroless Ni-Co-P films is mainly determined by the pH value of the metalization bath.

The electron micrographs of Fig. 28 show that the Ni-Co-P deposit is similar in morphology to that of the Ni-P deposit. The islands are almost spherical in shape and separated by "channels". The diffraction patterns of Fig. 29 demonstrate, again, the influence of the change of pH value in the metalizing solution. The decrease in phosphorus content appears to result in a larger average size of the crystallites, hence a greater degree of crystallinity. The crystalline structure can be easily indexed to be a f.c.c. structure having the same lattice constant of nickel (see Table VIII). This finding is not surprising as it is known that nickel can form a complete series of solid solution with f.c.c. cobalt.

Also, it has been found [123] that the structure of mixed Ni-Co-P with 90% cobalt changes from the h.c.p. phase to the f.c.c.

phase as the pH value of the metalization bath is increased. As a result, we have concluded that in the case of low cobalt concentration, the Ni-Co-P films have an amorphous structure at low pH and have a f.c.c. structure at high pH; on the other hand, in the case of high cobalt concentration the Ni-Co-P films have a h.c.p. structure at low pH but a f.c.c. structure at high pH. It is difficult to compare the present work with the result obtained by Korenev [122] since in his work, the pH value of the metalization bath and the Ni/Co ratio in the deposit are not known. However, the composition of solution given might suggest a low pH metalization bath.

Based on the above results, one can argue that the co-deposited phosphorus atoms occupy the lattice of nickel atoms, hence as the phosphous content is increased, the nickel crystallographic structure is disturbed from its f.c.c. structure to a "liquid-like" phase.

The above results are generally true regardless of the specific sensitizing pretreatment baths used.

3. Electroless Co-P Films

Electrodeposited Co-P films can be either crystalline[124, 125] or amorphous [126, 127] depending on the conditions of preparation. The crystalline Co-P deposit has been found to be predominantly h.c.p. in structure with its c-axis perpendicular to the basal planes. The f.c.c. phase only exists when deposited at room temperature and low pH of the metalization bath. As the pH value is increased, the structure changes from f.c.c. to h.c.p. with the intermediate stage consisting

of both phases.

Recently, radial distribution function analysis by Cargill [126] has shown that the arrangement of atoms in the electrodeposited amorphous Co-P alloys is similar to the dense random packing of hard spheres, [117, 118].

On the other hand, most investigators [9,11-16] reported that the electroless Co-P films are predominantly h.c.p. with a preferred orientation of the c-axis. Films with phosphorus content less than 2 W/o, on the average, exhibit a normal orientation of the c-axis to the substrate; those with a higher phosphorus content generally have their c-axis parallel to the substrate. Others [16,128] reported that when deposited from a pH value in excess of 8.2, the Co-P films assume an amorphous structure.

In the present work, the effect of changing the pH of the metalizing bath is not immediately obvious by examining the series of electron micrographs and diffraction patterns presented in Figs. (30) and (31). Unlike the Ni-P films deposited from an acidic bath and the Ni-Co-P films, the islands of Co-P films are not spherical in shape, but a tendency to be isolated one from another by a series of "channels" is evident. Within each island, subcrystallite fine structure is revealed by the existence of groups of fringes which sometimes extend across a whole grain. Dark field electron micrographs indicate that these fringes are definitely caused by diffraction contrast, or of the type associated with thickness variations; and are not merely

artifacts. This is different than for electroless copper films, where twin faults have been confirmed [129]. Using replica techniques, Sallo et al [130] also concluded that electrodeposited Co-P films were heavily faulted with individual grains consisting of a series of platelets. Nonetheless, we also agree about the role of the co-deposited phosphorus as a "growth inhibitor" [9] both for cobalt and nickel. This is best demonstrated by the existence of "channels" which might very well be composed of phosphorus which, being insoluble in cobalt, would therefore have been expelled to the island boundaries. The observed high fault densities can also be connected to the co-deposited phosphorus, however, the mechanism by which phosphorus causes the faults is not yet known.

The diffraction pattern can be indexed as a mixture of h.c.p. and f.c.c. phases (see Table IX). For comparison, we also list in the table the lattice parameters derived from the diffraction pattern, Fig. 32, of a vacuum deposited cobalt film.

In principle, it should be possible to distinguish between f.c.c. and h.c.p. on the basis of the strength of the (200) diffraction ring, but it is difficult to give an unambiguous assignment to the rings in Fig. (31). Our assumption, however, is that to begin with, the Co-P films constitute a mixture of f.c.c. and h.c.p. phases. Increasing the pH or decreasing the phosphorus content tips the ratio more toward the f.c.c. phase.

Frieze et al [9] have studied the morphology of thin Co-P films in some detail. The film thickness range covered by their experiments in 500 - 20,000 Å, while we are interested here in much thinner samples.

In addition, the resolution of our micrographs is at least ten times better than theirs. As we see from our work, the influence of phosphorus content will show at much lower thickness than 1000 Å, and an alternative explanation for the difference between Fig. (30), might be the change in fibre axis from (0001) to $(10\bar{1}0)$. This will, of course, explain also the lack of changes in passing from Fig. (31a) to (31c). The difficulty in accepting this approach lies in the fact that in very thin films like ours, one would expect the initial deposition on the activated surface to have its basal plane of the hexagonal lattice predominantly parallel to the substrate. Only thicker samples would be expected to have their fibre axis orientation depend on the phosphorus content [9]. This difficulty returns us to the first suggestion of a mixed h.c.p. - f.c.c. phases.

Unusual lace-like growth pattern of electroless Co-P films deposited on Formvar substrates using conventional sensitizer has been reported [8]. In the present study, and among many others, no such growth pattern has ever been observed. During the early stages of growths, electroless Co-P is most probably amorphous [3] and the extent of crystallization and the size of the individual crystallites increase with deposition time.

Electroless Co-P films deposited on surfaces prepared with the catalytic solution do not show any subcrystallite fine structures. This is most probably due to the smaller size of individual crystallites. This point is also demonstrated clearly in the diffraction patterns.

From the above discussion, we note that the addition of phosphorus to cobalt appears to have a much greater effect on the appearance of the deposite but much less effect on the crystallinity than it is added to nickel. This is associated with the insolubility of phosphorus in cobalt.

4. Heat Treated Electroless Metal Films

Several electroless thin metal films deposited on Formvar surfaces were annealed in a vacuum of about 10^{-5} Torr from room temperature to about 450°K to examine their behaviour with regard to heat-treatment, especially to the possible changes in film structure.

Electroless Ni-P, upon heat-treatment, is known [131,132] to transform at about 325°C to a more stable two-phase system consisting of f.c.c. nickel and tetragonal Ni_3P. Electroless Co-P, on the other hand, will transform to an equilibrium two-phase structure consisting of f.c.c. cobalt and orthorhombic Co_2P at about 465°C [133].

Electrodeposited Co-P was reported [134] to transform from non-crystalline to crystalline at a much lower temperature, about 300°C.

In the present work, structure changes under the electron microscope were not yet observed in the temperature range of room temperature to 450°K. Comparison of Fig. 33 and Fig. 30, however, offers a convincing proof that upon heat-treatment, the electroless Co-P deposits lose their subcrystallite fine structure as can be seen

by the disappearence of groups of fringes. That this is so can be argued qualitatively in the following way. As the annealing temperature increases, a part of the phosphorus boundary combines with only a part of cobalt at the island contact with the insultator medium. This reduces the fault densities, and finally, as the annealing temperature reaches about 465°C, gives Co_2P.

The present results are in good agreement with the results of Pai et al [132]. They also suggested that in the temperature range of 300°-450°K, heat treatment of the Ni-P samples causes practically no change in the structure.

(III) Electrical Properties of Electroless Metal Films

1. Sheet Resistivity (ρ/d)

The small size effect in the electrical properties of thin metal films have been studied widely [44,51,52]. Most investigators studied the size effect in vacuum deposited thin metal films, since size effect parameters are easier to reproduce and control in those films. Little has been reported in the literature on the electrical properties of electrolessly deposited thin metal films. Marton et al [132,135,136] have studied the electrical properties of Ni-P films deposited from an acidic bath to some extent. Upon annealing, a certain type of irreversible change in the resistivity of Ni-P films was observed. This they attributed to the transformation of a single phase

structure to a two-phase structure of f.c.c. Ni and tetragonal Ni_3P. A similar type of irreversible change in the resistivity has also been reported for bismuth [137], Cu-Ag [138] and Cu [139] films.

In the present study, a similar irreversible change in the sheet resistivity (ρ/d) has been observed for electroless Ni-P, Ni-Co-P and Co-P films upon annealing in vacuum in the temperature ranges of 290°-450°K. In this temperature range, no structural changes can be observed. Based on some experimental evidence, we claim that the irreversible change in the sheet resitivity is due to the desorption of gases and, to some extent, the annihilation of microcrystallites.

The thickness dependence of the sheet resistivity of Ni-P and Ni-Co-P films are shown in Figs. 34-37 . Here, the deposition time is taken as a measure of thickness. This is so because, according to Marton and Schlesinger [6], the mass thickness of Ni-P deposits is linearly proportional to the deposition time, at least within the regions of discontinuous and of continuous films. (See Fig. 7 of ref. 6). The present results of thickness-dependent sheet resitivity of Ni-P and Ni-Co-P films are much larger than those predicted by the Fuchs-Sondheimer theory, but they are in good agreement with previous findings [135]. This can be seen in the following table.

Note that the thickness of the Ni-P product were also measured by the Tolansky method. The percentage deviation in the measured and the calculated thickness was about 20%, however, the uncertainty in the measured thickness is about the same, hence, no measured thickness was included in the table.

TABLE XIV

Estimated Resistivity of Ni-P Films

Deposition time (min)	Thickness[1] (Å)	ρ (μΩcm)[2]	ρ (μΩcm)[3]
65	∿ 1000	3×10^3	2×10^3
50	∿ 700	4×10^3	3×10^3
35	∿ 500	1.5×10^4	2×10^4
20	∿ 200	4×10^4	2×10^5

(1) Calculated from equation (2) of ref. 6 using C = 15 Å/min. and $\alpha = 10/\mu^2$

(2) Present work .

(3) Marton and Schlesinger [135].

The large sheet resistivity indicates that scattering mechanisms other than the diffuse scattering by the film surface are responsible: It is also difficult to explain the high sheet resitivity of these films with a diffuse scattering mechanisms as being due to crystal faults, such as twins, stacking fault and vacancy etc., since no such crystal faults have been directly observed in these systems. If, however, we assume the electron mean free path to be around 500 Å for nickel, as suggested by Crittenden et al [140], it is then obvious from the electron micrographs (see Figs. 23 and 28) that electron scattering

at island boundaries should play a major rule since the average island size is of this order. On the other hand, it is known from electron microscopy studies that electroless metal films have pores. This is also confirmed by the study of the film density which increases with increasing film thickness (see Fig. 7 of ref. 135). Thus, an initial increased porosity should result in a higher sheet resistivity. This is best demonstrated in Figs. 37 and 38 in which three clear rectilinear regions are shown. This behavior, we believe, is determined wholly by those structural changes which occur during the growth of the electroless metal films. Initially, the film sheet resistivity decreases rapidly from a value which is governed practically by the substrate resistivity to a value determined by a random distribution of islands (region I); in the second region, the film sheet resistivity is due to the network of porous films; and finally, the increase in the film thickness resulted in a much slower decrease in film sheet resistivity (region III). It can be argued quantitatively that in region I where the film is discontinuous in structure, the conduction mechanism is substrate-assisted tunneling, as suggested by Hill [71-73]. This is so because, as discussed in Chapter 1, section IV, the substrate-assisted tunneling mechanism is most applicable to the case of large island size and small interisland separations.

In addition, we believe that the adsorbed gases also contribute to some extent to the observed high sheet resistivity. This is best seen in Table XII, where the sheet resistivity of electroless Ni-P, Ni-Co-P and Co-P films are shown to decrease to as much as 50%

of its original value after being kept in a vacuum of about 10^{-5} Torr overnight. It should be noted that the percentage decrease of sheet resistivity of Ni-P is less signficant and that the smaller the sheet resistivity, the larger is the percentage decrease. Furthermore, this kind of change in sheet resistivity is a reversible process. If we assume a partial desorption of gases after evacuation, it is not unreasonable to find that a partial desorption of gases would allow better contact between adjacent islands, hence decreases the sheet resistivity. Also, for thinner films, the effect of gas desorption is less significant because of the porosity that this kind of film has. Besides, the effect of adsorbed gases on the film surface also reduce the effective film thickness, consequently, the sheet resistivity increases.

Previously, we have concluded that the use of catalytic solutions results in a more homogeneous distribution of catalytic sites on the pretreated substrate surface, and consequently in a finer and denser island distribution of the electroless end product. Thus it is not surprising to see that the sheet resistivity of electroless Ni-P films deposited by using the catalytic solution is almost one order of magnitude smaller in the early stage of metal deposition than that obtained using conventional sensitizers (see Fig. 34). As the deposition time increases, the difference in sheet resistivities decrease and finally disappear.

By examining the sheet resistivity (normalizedat room tem-

perature) vs annealing temperature curves presented in Fig. 38, we note that the irreversible change in sheet resistivity does not occur at the same temperature for the electroless metal films. The temperature at which the sheet resistivity starts to decrease is higher for Ni-P films and it is almost the same for Ni-Co-P and Co-P films. This difference in behavior is not difficult to understand if gas desorption is considered to be the main cause of such an irreversible change in sheet resistivity. As can be seen in Table XII, the partial desorption of gases due to evacuation is less significant for Ni-P films than for Ni-Co-P and Co-P films. Based on this line of argument, it is not surprising to see that the irreversible change in sheet resistivity of Ni-P film should occur at a higher temperature.

It is known that heat treatment releases the gases trapped inside the lattice, while evacuation only releases the adsorbed gases on the surface layer, thus it is not unreasonable to argue that desorption of gases due to evacuation is a reversible process and that, on the other hand, due to annealing is an irreversible process.

It should be remembered that the decrease in sheet resistivity, in addition, may also be a result of the annihilation of grain boundaries as suggested by Pai et al [132].

Pai et al [132] also suggested that during the annealing process of electroless Ni-P films up to about 800°K, the formation of Ni_3P tends to increase the resistivity. In order to find if the formation of Co_2P would likewise increase the sheet resistivity of electroless Co-P during the annealing process, additional experiments

were done in which electroless Co-P films were annealed in vacuum from room temperature to about 800°K. The result is presented in Fig. 39. Here, it is difficult to conclude that the formation of Co_2P tends to increase the sheet resistivity, also the phase change of cobalt from h.c.p. to f.c.c. does not seem to change the sheet resistivity either. It is conceivable that the increase in sheet resitivity due to the formation of Co_2P is overwhelmed by the decrease in sheet resisitivity due to the annihilation of grain boundaries.

2. Temperature Coefficient of Resistivity (T.C.R.)

The T.C.R. of electroless Ni-P, Ni-Co-P and Co-P films were found to be positive, indicating a metallic conduction mechanism in those films. Values of the T.C.R. for a series of Co-P films deposited under various conditions were presented in Table X. The T.C.R. ranges between $1\text{-}3 \times 10^{-3}/°K$. It is difficult to assess the effect of co-deposited phosphorus upon the T. C. R. values. The scatter in the values of T.C.R. is attributed to the errors in film preparation. From the table, it appears that the T.C.R. of the thin films of Co-P is almost constant over a wide range of thickness. This we believe may be the effect of oxidation, since the oxidation effects tend to make island size independent of thickness, so that electrons travelling through the film see the same matrix whether they travel through the film next to the substrate-film interface or through the bulk of the film.

3. Hall Effect

It is well known that the measurement of the Hall coefficient can yield the charge carrier concentration. A study of the size effect on the Hall phenomenon can provide supplementary information on the transport parameters in thin metal films. The few studies of this nature that have been reported in the literature [141-145] have yielded some contradictory results. The Hall coefficient of thin potassium films was found to decrease with thickness much less than expected [141,142], even though the resistivity was found to be in excellent agreement with the Fuchs-Sondheimer theory. Chopra et al [143] have reported, on the other hand, that nearly bulk values for Hall coefficient and mobility were observed for single crystal films of copper, gold and silver. Darion and Colombani [144] reported that for evaporated polycrystalline Co films, R_o increased with thickness above 250 Å and R_1 decreased continuously with thickness.

Recently, Galepov [145] reported that the extraordinary (ferromagnetic) Hall coefficient R_1 and the resistivity ρ are related through the formula $R_1 = C\rho^n$ [146] with $n = 1$ for poly-crystalline cobalt films (c is a temperature-independent constant of the metal).

In the present work, Hall effect in electroless Ni-P, Co-P and Ni-Co-P films have been measured. The charge carriers were found to be electrons for Ni-P films and holes for Ni-Co-P (65% Ni) and Co-P films.

The Hall mobility, in general, increases with decreasing sheet

resisitivy, i.e. increasing film thickness. On the other hand, no appreciable variation was found for Hall coefficient/thickness (R_H/d) for sheet resistivity above 200 ohms/□; below that value the Hall coefficient/thickness appears to decrease more rapidly as the sheet resistivity decreases.

Both nickel and cobalt are known to be ferromagnetic and that single crystals of cobalt have two principal Hall coefficients of opposite sign. The one with positive sign, the extraordinary Hall coefficient R_1 is approximately two orders of magnitude larger than the other one, the ordinary Hall coefficient R_o. For nickel R_o and R_1 are negative. In principle, the two Hall coefficients can be determined separately from the slope of the straight parts of curves of Hall e.m.f. vs applied magnetic field [82] (see also Fig. 7).

In the current experiment, the low applied magnetic field used suggested that the Hall coefficient thus measured is the extraordinary Hall coefficient. In Table XIII, we note that the measured value of Hall coefficient for Co-P films is of the same order of magnitude as that of the extraordinary Hall coefficient obtained from literature [145,147].

Secondly, the Hall e.m.f. vs applied magnetic field curve for Co-P films appears to deviate from the straight line at about 8 KG. in a manner described by Pugh [82].

Below the sheet resistivity value of about 200 ohms/□, the rise in R_1 with increasing sheet resistivity can be attributed to

the adsorbed gases, and the partial oxidation of the metal films. In this region, the electroless metal films are continuous, thus the presence of adsorbed gases reduces the concentration of charge carriers in the film as the sheet resistivity increases, and consequently R_1 rises. This is also confirmed (see Table XI) by measuring the sheet resistivity and Hall effect under different conditions. The decrease in sheet resitivity due to evacuation results in the partial desorption of gases, thus increasing the concentration of charge carriers, and consequently R_1 rises. Besides this, the decrease in film thickness as the sheet resistivity increases also reduces the effective number of charge carriers, and consequently R_1 rises. The large (up to a maximum of 40%) scatter in the value of R_1 in this region can also be attributed to the large uncertainty in the distribution of adsorbed gases and/or on the fraction of cubic phase present. The value of R_1 calculated for 500 Å is about 21 x 10^{-4} cm^3/amp sec. (see Table XIII) which is in good agreement of the results of Darion and Colombani. Note that the values of R_1 (range from 12-20 x 10^{-4} cm^3/amp.sec) quoted are for 750 Å. Beyond this region, the metal films assume a partially continuous structure, the conductivity is thus limited to the effect of adjoining islands, so that the adsorbed gases do not greatly affect the concentration of charge carriers. Hence there is no rise in R_1. Also in this region, R_1 can be related to ρ by the formula $R_1 = C\rho$ in good agreement with the results of Galepov [145]. It should be noted that the cobalt films used in [145] also reveal a

patchy structure in the thickness range where the formula $R_{\square} = \rho/t$ holds. We also agree that the hole type of charge carrier is more sensitive to lattice defects [145].

Next, the results presented in Fig. 46 were obtained with Co-P films deposited on Formvar coated glass using Shipley's catalyst. From the previous discussion, it is concluded that the metal films are continuous in this range of sheet resisitivity which is determined mainly by the film thickness; the scatter in the value of $R_{\square}$ is accordingly much less due to the homogeneity of the film thickness.

The Hall mobility μ_H shows a thickness dependence which is most pronounced for annealed films. The marked thickness dependence can be explained by assuming additional scattering at the crystallite boundaries. As can be seen in Table XI, annealing of a typical Ni-Co-P film can increase the Hall mobility by a factor of almost three. This is so because of the desorption of gases and annihilation of grain boundaries upon annealing. It should also be noted that the Hall mobility of heat treated Ni-Co-P and Co-P films reaches a maximum value of more than two times the value for bulk cobalt (μ_H = 38.4 cm^2/v-sec at 290°K). As the sheet resistivity decreases, the Hall mobility decreases to a value as low as 2 cm^2/v-sec. A sound interpretation of the very low value of Hall mobility does not seem to be an easy matter. The imperfection of the lattice arising from contamination by foreign atoms does not seem to provide for such a great lowering of the mobility. If we assume the films consist of low-resistivity grains (metal islands)

separated by thin layers of high-resistivity materials (e.g., adsorbed gases or oxidized metal layer), then according to Volger [148] and others [149-152], the measured Hall coefficient does not differ very much from that of the low-resistivity grains, but the measured resistivity can be much greater than that of the low-resistivity grains. Consequently, as the resistivity increases, the Hall mobility decreases.

It is interesting to note that although electroless Ni-Co-P (65 % Ni) films have the same f.c.c. structure as Ni-P films, the behaviour of the extraordinary Hall coefficient is similar to that of Co-P films. This suggests that the ferromagnetic properties of Ni-Co-P (65 % Ni) films should be similar to those of Co-P films. In the study of the energy band structure of Ni_3P and Co_2P, Drake and Schlesinger [153,154] reported that the density of states curve of Ni_3P is very similar to that obtained for pure nickel [155], while that of Co_2P shows a larger peak at high energies than the d-peak of pure cobalt. Thus they concluded that the addition of phosphorus to cobalt appears to have a much greater effect on the electronic energy levels than when it is added to nickel.

Pure nickel in the solid state is known [29] to have an incomplete 3d band containing 9.4 electrons per atom and a partially filled 4s band containing 0.6 electrons. In the 3d band 5 of the states (down-spin) are all filled and the remaining 4.4 in the opposite direction. Thus in ferromagnetic Ni, the up-spin bands which contribute to the extraordinary Hall effect, are electronic in character. This

accounts for the negative sign of R_1 found at room temperature [156].

Purecobalt also has an incomplete 3d band and a partially filled 4s band in the solid state, containing approximately 8.3 and 0.7 electrons respectively. This provides 1.6 "heavy" holes available for current conduction.

The conductivity of transition metals due to the holes was thought [29] to be negligible in comparison with that due to the electrons owing to the large effective mass of the holes. However, studies of the Hall effect indicates that it is both reasonable and necessary to assume for the ferromagnetic materials that the "heavy" holes are itinerant and contribute to conduction [157].

It has been suggested [135] that in the electroless Ni-P films, the 3p electrons of phosphorus penetrate the 3d holes of nickel. It is also appropriate to suggest that in the electroless Co-P films, the 3p electrons of phosphorus penetrate the 3d holes of cobalt and that in the electroless Ni-Co-P films, the 3p electrons of phosphorus fill up the 3d holes of nickel, thus accounting for the similarity in extraordinary Hall coefficient between Ni-Co-P and Co-P films.

The model for the electroless Ni-P, Ni-Co-P and Co-P films is supported by the experimental findings as follows: (a) The sheet resistivity of as-deposited Ni-P, Ni-Co-P or Co-P films is much higher than that predicted by the Fuch-Sondheimer theory, (b) heat treatment reduces the sheet resistivity to about 20% of its initial value.

(c) the charge carriers are holes for Ni-Co-P and Co-P films and are electrons for Ni-P films, (d) the extraordinary Hall coefficient of Ni-Co-P (65% Ni) is of the same order as that of Co-P films with similar thickness.

The present model can also account for the experimental results that the coercivity of electroless Co-P increases with the increasing phosphorus content [121].

CHAPTER 5

Conclusions

As a result of this work, we reach quite a number of conclusions improving our understanding of the microstructure and electrical properties of electroless thin metal films. This work also provides clarifications to some debated aspects of electroless plating.

In the following table, the microstructure of deposits after each pretreatment step is summarized.

TABLE XV

Microstructure of Deposits on Formvar Substrate at Each State of Various Pretreatment Steps

Pretreatment Solution	Post Sensitizing/ Catalyzing rinse	Post activating/ Accelerating rinse
conventional sensitizers	hydrated stannous oxide (SnO_2)	amorphous
improved sensitizers	stannic polymeric material*	amorphous*
Shipley's catalytic solution	amorphous*	f.c.c. Pd_3Sn*

*Present work

Microscopically, as well as macroscopically, the adsorbed sensitizer clusters and particles using improved sensitizers and catalytic solutions, are more uniformly distributed on the Formvar surface when compared with those obtained using conventional sensitizers. The density of adsorbed centers is about 10^{12} centers/cm^2, which is approximately an order of magnitude greater than in the case of conventional sensitizers. No significant difference was observed with respect to the basic particle size. The worm-like growth pattern obtained using Shipley's catalytic solution differed markedly from the usual cluster formation observed using other pretreatment solutions. No explanation can be given to this.

Also, the seeming lack of agreement among previous results concerning the microstructure of deposits after each pretreatment step might well be conceived as being due to the different substrates used.

Examination of the electroless metal films in which deposition was interrupted during the early stage of nucleation and growth shows major differences. The improved sensitizers and the catalytic solutions show a greater degree of metallic coverage for the same immersion time in the electroless metal baths. This observation is not surprising in view of the fact that the improved sensitizers and the catalytic solutions yield a greater number of active centers which are distributed more uniformly on the surface.

U.V. irradiation has been shown to be effective in inhibiting the electroless deposition of Cu, Co and Ni if applied after conventional

sensitization, and of Co and Ni if applied after activation. The effect of u.v. irradiation is thought to induce structural changes in the sensitizing and/or activating agents, thus inhibiting the deposition. This result suggests that the redox reaction mechanism between tin II and palladium II is not a prerequisite for the successful electroless deposition using conventional sensitizers, hence rendering the redox model rather incomplete.

In case of the catalytic solution, it has been found that a stable ionic complex is formed rather than a colloid based upon elemental palladium. The role of the accelerator is to remove the divalent tin protective layer, thus exposing the active catalytic sites for subsequent electroless plating. Moreover, best plating results were obtained whenever Pd_3Sn was found present on the dielectric substrate surfaces.

The electroless metal deposits are nucleated on the products of the preplating treatments, and grow in size until they touch one another. The pretreatment solutions do not interfere with the structure of the metallic end product.

The structure of as-deposited electroless metal films depends strongly on the pH value of the metalization bath, hence on the amount of co-deposited phosphorus. The results for thin metal films of Ni-P, Ni-Co-P and Co-P are summarized in the following table.

TABLE XVI

Structure of Electroless Thin Metal Films

Films		structures low pH (high P content)	high pH (low P content)
Ni-P		amorphous	"strained" f.c.c. Ni
Ni-Co-P	low Co conc.	amorphous*	f.c.c. Ni*
	high Co conc.	h.c.p.*	f.c.c.*
Co-P		predominately* h.c.p.	Predominately* f.c.c.

*Present work

Assuming the as-deposited films to be a solid solution of phosphorus in a very fine polycrystalline system, it is not unreasonable to expect that decreasing the phosphorus content should result in an increase in the average size of crystallites.

The co-deposited phosphorus acts as a "growth inhibitor" both for cobalt and nickel. Because of this, electroless metal films tend to retain a granular structure long after substrate coverage is achieved.

Upon heating in vacuum, no structure changes can be observed in the annealing temperature ranges of 290 to 450°K, however, annihilation

of microcrystallites does take place as confirmed by the disappearance of groups of fringes. It is believed that upon annealing, a part of the phosphorus combines with only a part of cobalt and/or nickel at the particle contact, thus forming Co_2P and/or Ni_3P when the annealing temperature is high enough (well above 450°K).

The high sheet resitivity of as-deposited electroless metal films suggests that scattering mechanisms other than those due to the surface scattering are responsible. Based upon the fact that the sheet resistivity of as-deposited electroless metal films decreases by as much as 50% after being kept in vacuum, we suggest that adsorbed gases is responsible for the observed high sheet resistivity. The suggestion is also confirmed by the irreversible change in the sheet resitivity of electroless metal films upon annealing in vacuum. Since the behavior of the normalized sheet resitivity with temperature is, in general, independent of the thickness and the co-deposited phosphorus content, the irreversible change in the sheet resitivity is thus produced by the desorption of gases and the annihilation of the microcrystallites.

Hall effect measurements establish that the charge carriers for electroless Ni-P films are electrons, while those for electroless Ni-Co-P and Co-P films are holes.

The Hall coefficient measured is essentially the extraordinary Hall coefficient. Its value increases with increasing sheet resitivity, hence decreasing film thickness, however, no appreciable variation

was observed when the sheet resistivity was more than 200 ohm/□ . Also the value of the extraordinary Hall coefficient is of the same order of magnitude as that for the bulk material. The variation of the value of the extraordinary Hall coefficient is attributed to the microstructure of the electroless metal films. When the film is continuous, the extraordinary hall coefficient increases with decreasing film thickness. When the film is partially continous (network-like), the extraordinary Hall coefficient remains almost constant and that the relation $R_1 = C\rho$ holds.

Unlike the extraordinary Hall coefficient, the Hall mobility shows a marked dependence on film thickness. This is supported by the increase in Hall mobility when the film is annealed. In fact, the Hall mobility of an annealed film can be almost two times greater than that of unannealed film. Such an increase is apparently due to the decrease in resistivity of the metal film upon annealing. The very low value of Hall mobility is attributed to the inhomogeneous island structure of the electroless metal films.

APPENDIX A

Fuchs-Sondeimer Theory

Consider a metal film of thickness d in the direction of z-axis, the surfaces being the plane z = 0 and z = d as shown.

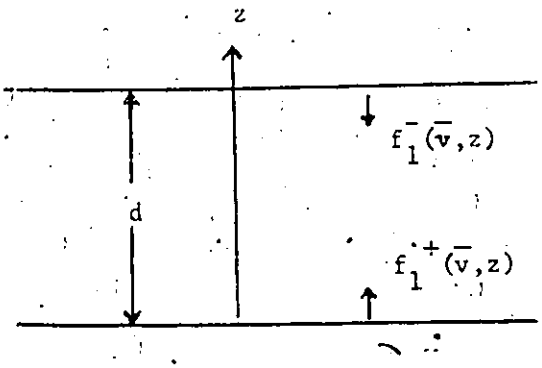

The Boltzman transport equation is

$$(A\text{-}1) \qquad -e\bar{E} \cdot \nabla_p f + \bar{v} \cdot \nabla_x f = \frac{f-f_o}{t}$$

where $\bar{v}$ is the electron velocity, $\bar{E}$ is the applied electric field and f is the statistical distribution function and t is the relaxation time. Now suppose the electric field is in the x-direction so the distribution function may be written in the form:

$$(A\text{-}2) \qquad f = f_o + f_1(\bar{v},z)$$

where $f(\bar{v},z)\,dxdydzdv_x dv_x dv_z$ denotes the number of electrons per volume element at a distance z from the surface of the film with velocity between (v_x, v_x+dv_x), $(v_y, v_y + dv_y)$ and $(v_z, v_z + dv_z)$.

Furhter neglecing the product Ef_1, equation (A-1) reduces

$$t\sigma \quad (A\text{-}3) \qquad \frac{eE}{m}\frac{\partial f}{\partial v_x} + v_z\frac{\partial f_1}{\partial z} = -\frac{f_1}{t}$$

The general solution is then:

$$(A\text{-}4) \qquad f_1(\bar{v}z) = \frac{etE}{m}\frac{\partial f_o}{\partial v_x}\left\{\Gamma + F(v)\exp\left(-\frac{z}{tv_z}\right)\right\}$$

where $\Gamma(\bar{v})$ is an arbitrary function of $\bar{v}$ determined by the boundary conditions at the surfaces of the film. To determine the boundary conditions, we first assume that every free path is terminated at the surface, so the scattering is entirely diffuse. The distribution function of the electrons leaving each surface must be independent of direction. Hence for electrons moving away from the surface $z = 0$, equation (A-4) can only be satisfied if we choose $F(\bar{v})$ such that $f_1(\bar{v},o) = o$, i.e. $F(\bar{v}) = -1$. Similarly $-F(\bar{v}) = \exp\left(-\frac{d}{tv_z}\right)$ for all electrons moving away from the surface $z = d$. There are two distributions function:

$$(A\text{-}5) \qquad f_1^{+}(\bar{v},z) = \frac{etE}{m}\frac{\partial f_o}{\partial v_x}\left\{1 - \exp\left(\frac{-z}{tv_z}\right)\right\} \qquad v_z > 0$$

$$(A\text{-}6) \qquad f_1^{-}(\bar{v},z) = \frac{etE}{m}\frac{\partial f_o}{\partial v_x}\left\{1 - \exp\left(-\frac{d-z}{tv_z}\right)\right\} \qquad v_z < 0$$

The current density for a position z is given by

$$(A\text{-}7) \qquad J(z) = -2e\left(\frac{m}{n}\right)^3\int v_x f_1 d\bar{v}_x$$

By introducing the polar coordinates (v,θ,ϕ) in the velocity space, equation (A-7) can be readily integrated to

$$(A\text{-}8) \qquad J(z) = \frac{2e^2m^2E}{h^3}\int_o^{\infty} dv \int_o^{2\pi} d\phi\, tv^3\cos^2\phi\,\frac{df_o}{dv}$$

$$\cdot\left[\int_o^{\pi/2}\sin^3\theta\left\{1-\exp\left(\frac{-z}{tv\cos\theta}\right)\right\}d\theta + \int_{\pi/2}^{\pi}\sin^3\theta\left\{1-\exp\left(\frac{d-z}{tv\cos\theta}\right)\right\}d\theta\right.$$

The overall current I is then given by

$$(A\text{-}9)\quad I = \frac{4\pi e^2 mE\tau v^3}{h^3}\left[\frac{2}{3} - \frac{\ell}{4d} + \frac{\ell}{d}\int_0^{\pi/2} \sin^3\theta\cos\theta\; e^{\frac{vd}{\ell\cos\theta}}\, d\theta\right]$$

hence the conductivity $\sigma = J/E$ is

$$(A\text{-}10)\quad \sigma = \sigma_o\left[1 - \frac{3\ell}{8d} + \frac{3\ell}{2d}\int_0^{\pi/2} \sin^3\theta\cos\theta\, e^{\frac{-d}{\ell\cos\theta}} d\theta\right]$$

where $\sigma_o = \frac{8\pi e^2 m\tau v^3}{h^3}$ being the conductivity of the bulk metal. Defining $k = d/\ell_o$ and $x = 1/\cos\theta$ equation (A-10) can be simplified and led to equation (31).

Next, assuming a portion P of the electrons are scattered specularly at the film surfaces and that a portion (1-p) of electrons are scattered randomly. At the surface $z = 0$, the electron leaving at $z = 0$ have the distribution function of the form

$$(A\text{-}11)\quad f_o + f_1^+(v_z, z = 0)$$

but a portion of the electrons arriving at $z = 0$ are scattered specularly, i.e. $p\{f_o + f_1(-v_z, z = o)\}$, while those scattered randomly give a contribution g which is independent of the direction $\bar{v}$, hence by (A-11), we have

$$(A\text{-}12)\quad f_2 + f_1^+(v_z, z=o) = p\{f_o + f_1^-(-v_2, z=0)\} + g$$

or

$$(A\text{-}13)\quad g = (1-p)\, f_o + \frac{e\tau E}{m}\frac{\partial f_o}{\partial v_x}\left(1-p + F(\bar{v})\,(1-p)e^{\frac{-d}{\tau v_z}}\right)$$

$$= (1-p)\, f_o$$

since g is independent of $\bar{v}$, thus

$$(A\text{-}14) \quad F(\bar{v}) = (1-p)/(1-pe^{\frac{-d}{\tau v_z}}) \quad \text{for } v_z > 0$$

Similarly, at the surface z = d, we have

$$(A\text{-}15) \quad F(\bar{v}) = (1-p)/(1-pe^{\frac{d}{\tau v_z}}) \quad \text{for } v_z < 0$$

Therefore, the two distribution functions are

$$(A\text{-}16) \quad f_1^{+}(\bar{v},z) = \frac{e\tau E}{m}\frac{\partial f_o}{\partial v_x}\left\{1 - \frac{1-p}{1-pe^{\frac{-d}{\tau v_z}}} e^{\frac{-z}{\tau v_z}}\right\}$$

$$(A\text{-}17) \quad f_1^{-}(\bar{v},a) = \frac{e\tau E}{m}\frac{\partial f_o}{\partial v_x}\left\{1 - \frac{1-p}{1-pe^{\frac{d}{\tau v_z}}} e^{\frac{d-z}{\tau v_z}}\right\}$$

Following the same procedure we arrive at equation (34)

APPENDIX B

Van der Pauw's Four Probes Method

Consider a flat, homogeneous, irregular sample completely free of isolated holes and provide it with four sufficiently small contacts A,B,C, and D at arbitrary places on the circumference as shown.

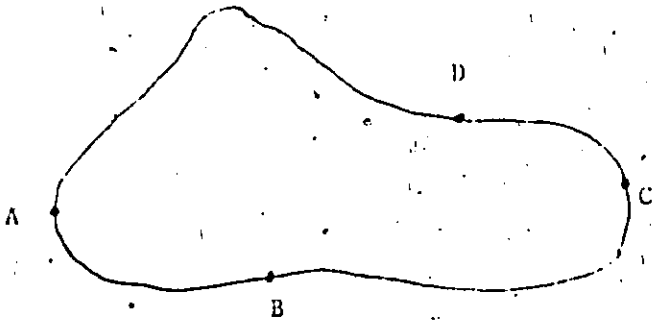

Since the sample is homogeneous in thickness and free of holes, it is always possible to find a function which conformally maps the sample to a semi-infinite plane with the four contacts along its boundary spaced at a distance, a,b, and c respectively as shown below

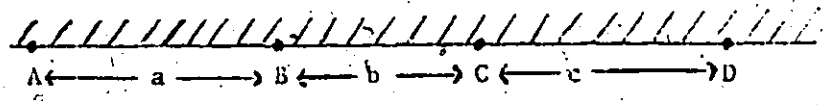

Let d denote the thickness of the sample and ρ the resistivity. A current j enters the semi-infinite plane at the contact A and leaves it at contact B. At a distance γ from A, the current density

is

$$(B\text{-}1) \qquad J = j/\pi\gamma d$$

The field strength E is given by

$$(B\text{-}2) \qquad E = \rho J$$

For the current enters at A, the potential difference between contacts C and D is

$$(B\text{-}3) \qquad (V_D - V_C)_{in} = \int_D^C E d\gamma = -\frac{\rho j}{\pi d} \ln\left(\frac{a+b+c}{a+b}\right)$$

For the current leaves at B, the potential difference between contacts C and D is

$$(B\text{-}4) \qquad (V_D - V_C)_{out} = \int_D^C E d\gamma = \frac{\rho j}{\pi d} \ln\left(\frac{b+c}{d}\right)$$

Super-position of equations (B-3) and (B-4) yields the potential difference between contacts C and D due to the current enters at contact A and leaves it at contact B, and is given by:

$$(B\text{-}5) \qquad V_D - V_C = \frac{\rho j}{\pi d} \ln\left[\frac{(a+b)(b+c)}{b(a+b+b+c)}\right]$$

Similarly, if a current j enters at contact B and leaves it at contact C, the potential difference between contacts B and A is given by:

$$(B\text{-}6) \qquad V_A - V_D = \frac{\rho j}{\pi d} \ln\left[\frac{(a+b)(b+c)}{ac}\right]$$

Hence by defining

$$(B-7) \quad R_{AB,CD} = \frac{V_D - V_C}{I_{AB}} \quad \text{and}$$

$$(B-8) \quad R_{BC,DA} = \frac{V_A - V_D}{I_{AB}}$$

it is obvious that

$$(B-9) \quad \exp.\ \left(-\frac{\pi d}{\rho} R_{AB,CD}\right) + \exp\ \left(-\frac{\pi d}{\rho} R_{BC,DA}\right) = 1$$

For simplification, we put

$$(B-10) \quad \pi d\ R_{AB,CD} = X_1$$

$$\pi d\ R_{BC,DA} = X_2$$

equation (B-9) can be reduced to

$$(B-11) \quad \exp\ (-X_1/\rho) + \exp\ (-X_2/\rho) = 1$$

which is the same as

$$(B-12) \quad \exp\ [-(X_1 + X_2)/2\rho]\ \cosh[(X_1 - X_2)/2\rho] = 1/2$$

by putting

$$(B-13) \quad \frac{X_1 + X_2}{2\rho} = \frac{\ln 2}{f}$$

the relation between the factor f and the ratio $R_{AB,CD}$ to $R_{BC,DA}$ is:

$$(B-14) \quad \cosh^{-1} \frac{(R_{AB,CD}/R_{BC,DA}) - 1}{(R_{AB,CD}/R_{BC,DA}) + 1} \cdot \frac{\ln 2}{f} = \frac{1}{2} \exp\ \left(\frac{\ln 2}{f}\right)$$

which is represented graphically in Fig. 13.

BIBLIOGRAPHY

1. A. Brenner and G. Riddel, J. Res. Natl. Bur. Standards, 37 31 (1946), 39 385 (1947)
2. R. L. Cohen, J. F. D'Amico and K. W. West, J. Electrochem. Soc., 118 2042 (1971)
3. S. L. Chow, N. E. Hedgecock, M. Schlesinger and J. Rezek, J. Electrochem. Soc., 119 1013 (1972)
4. W. Goldie, "Metallic Coating of Plastic", Vol. 1, Electrochem. Publication Ltd., England (1968)
5. R. Sard, J. Electrochem. Soc., 117 864 (1970)
6. J. P. Marton and M. Schlesinger, J. Electrochem. Soc., 115 16 (1968)
7. G. A. Jones and M. Aspand, Phys. Stat. Sol. (a) 11 637 (1972)
8. R. D. Fisher and S. D. Taylor, J. Appl. Phys., 37 2512 (1966)
9. A. S. Frieze, R. Sard and R. Weil, J. Electrochem. Soc., 115 586 (1968)
10. J. R. DePew, IBM Tech. Rept., TR 44.0152 (1971)
11. M. G. Miksic, R. Traviese, A. Arcus and R. H. Wright, J. Electrochem. Soc., 113 360 (1966)
12. Y. Moradzadeh, J. Electrochem. Soc., 112 891 (1965)
13. R. D. Fisher and W. H. Chilton, J. Electrochem. Soc., 109 485 (1962)
14. G. A. Jones and B. K. Middleton, J. Material Sci., 3 519 (1968)

15. Gh. Calugaru, E. Diaconu and I. Diaconu, Thin Solid Films 10 445 (1973)

16. M. Aspland, G. A. Jones and B. K. Middleton, IEEE Trans. Magnetics, MAG-5 314 (1969)

17. G. Gutziet, Plating, 47 No. 1 63 (1960)

18. H. Iwasa, M. Yokozawa and I. Teramoto, J. Electrochemical Soc., 115 485 (1968)

19. N. Feldstein and T. S. Lancsek, J. Electrochem. Soc., 118 869 (1971)

20. D. McBride and G. P. Vlasak, J. Electrochem. Soc., 118 2055 (1971)

21. R. L. Cohen and K. W. West, J. Electrochem. Soc., 119 433 (1972)

22. N. Feldstein and J. A. Weiner, J. Electrochem. Soc., 120 475 (1973)

23. C. H. De Minjer and P. F. P. v. d. Boom, J. Electrochem. Soc., 120 1644 (1973)

24. N. Feldstein and J. A. Weiner, Plating 59 140 (1972)

25. N. Feldstein and T. S. Lancsek, U. S. Patent, 3,666,527 (1972)

26. N. Feldstein and J. A. Weiner, J. Electrochem. Soc., 119 668 (1972)

27. N. Feldstein, J. A. Weiner and G. L. Schnable, J. Electrochem. Soc., 119 1486 (1972)

28. N. Feldstein, S. L. Chow and M. Schlesinger, J. Electrochem. Soc., 120 875 (1973)

29. J. Gueron, Ann. Chim., 11 225 (1935)

30. C. R. Shipley, Jr., U. S. Patent, 3,011,920 (1961)

31. E. D. D'ottavio, U. S. Patent, 3,532,578 (1970)

32. R. L. Cohen and K. W. West, J. Electrochem. Soc., 120 502 (1973)

33. Brit. Patent, 929, 799

34. A. Rantell and A. Holtzman, Tran. Inst. Metal Finishing, 51 62 (1973)

35. M. Tsukakara, T. Kishi, H. Yamamoto and T. Nagai, J. Metal Finishing (Japan) 23 83 (1973)

36. N. Feldstein, N. Schlesinger, N. E. Hedgecock and S. L. Chow, J. Electrochem. Soc., 121 738 (1974)

37. J. M. Ziman, "Electron and Phonons", Oxford University Press, Fairtown, N. J. (1962)

38. N. F. Mott and H. Jones, "The Theory and the Properties of Metals and alloys", London, Dover (1958)

39. A. H. Wilson, "The Theory of Metals", London, Cambridge University Press (1953)

40. J. J. Thomson, Proc. Cambridge Phil. Soc., 11 120 (1901)

41. K. Fuchs, Proc. Cambridge Phil. Soc., 34 100 (1930)

42. E. H. Sondheimer, Adv. Phys., 1 1(1952)

43. G. Brandli and P. Cotti, Helv. Phys. Acta 38 801 (1965)

44. K. L. Chopra, "Thin Film Phenomena", McGraw-Hill, N. Y., (1969)

45. D. S. Campbell, D. I. C. Thesis, Imperial College, London (1967)

46. A. F. Mayadas, R. Feder and R. Rosenberg, J. Vac. Sci. Technol., 6 690 (1969)

47. P. Wissmann, Thin Solid Films, 6 R67 (1970)

48. J. M. Heras and E. Toscano, Ber. Bunsenges, Physik Chem., 75 1135 (1971)

49. A. F. Mayadas and M. Shatzkes, Phys. Rev., B1 1382 (1970)

50. T. J. Coutts, Thin Solid Films, 7 77 (1971)

51. D. C. Larson, Phys. of Thin Film., 6 81 (1971)

52. D. S. Campbell and A. R. Morley, Rept. Progr. Phys., 34 Part 1 283 (1971)

53. K. L. Chopra, Phys. Lett., 15 21 (1965)

54. A. von Bassewitz and E. N. Mitchell, Phys. Rev., 182 712 (1969)

55. F. J. Blatt and H. G. Satz, Helv. Phys. Acta, 33 1007 (1960)

56. M. ya Azbel and R. N. Gurzhi, Sov. Phys.-J.E.T.P. 15 1133 (1962)

57. E. R. Andrew, Proc. Phys. Soc. A, 62 77 (1949)

58. R. I. Boughton and J. E. Neighlor, J. Low Temp.Phys., 7 241 (1972)

59. J. Bass, Adv. Phys., 21 431 (1972)

60. S. S. Minn, J. Res. Centr. Natl. Res. Sci. Lab. Bellevue (Paris) 51 131 (1960)

61. C. A. Neugebauer and M. B. Webb, J. Appl. Phys., 33 74 (1962)

62. T. E. Hartman, J. Appl. Phys., 34 943 (1963)

63. D. S. Herman and T. N. Rhodin, J. Appl. Phys., 37 1594 (1966)

64. K. van Steensel, Philips Res. Rept., 22 246 (1967)

65. J. G. Simmons, J. Appl. Phys., 35 2655 (1964)

66. C. J. Gorter, Physica, 17 777 (1951)

67. G. Darmois, J. Phys. Radium., 17 211 (1956)

68. P. Sheng and B. Abeles, Phys. Rev. Lett., 28 34 (1972)

69. P. Sheng, B. Abeles and Y. Arie, Phys. Rev. Lett., 31 44 (1973)

70. J. I. Gittleman, Y. Goldstein and S. Bvzowski, Phys. Rev. B 25 3609 (1972)

71. R. M. Hill, Nature, 204 35 (1964)

72. R. M. Hill, Proc. Roy. Soc., A309 377, 396 (1969)

73. R. M. Hill, Contemp. Phys., 10 221 (1969)

74. A. Miller and E. Abrahams, Phys. Rev., 120 745 (1960)

75. J. F. Dewald, J. Phys. Chem. Solid, 14 155 (1960)

76. L. Y. Wei, J. Chem. Phys., 39 2709 (1963)

77. B. T. Boiko, L. S. Palatnik and A. N. Synelnikov, Thin Solid Films 7 305 (1971)

78. A. A. Milgram and C. S. Lu, J. Appl. Phys., 37 4773 (1966)

79. C. A. Neugebauer, "Measurement Techniques for Thin Films", ed. Schwartz and Schwartz, Electrochem. Soc., N. Y., 191 (1967)

80. C. A. Neugebauer, Trans. 9th Natl. Vac. Symp., Los Angeles, ed. Bancroft, MacMillan, N. Y., 45 (1962)

81. E. H. Hall, Am. J. Math., 2 287 (1879)

82. E. M. Pugh, Phys. Rev., 36 1503 (1930)

83. E. H. Sondheimer, Phys. Rev., 80 401 (1950)

84. T. C. Boyce and W. H. Wong, Phys. Lett. 36A 323 (1971)

85. P. S. Sennett and G. D. Scott, A.O.S.A., 40 203 (1950)

86. Shipley 9F and 19F, Shipley Company Inc., Newton, Mass. U.S.A.

87. C. E. Hall, "Introduction to Electron Microscopy", McGraw-Hill N.Y., (1953)

88. P. W. Hawkes, "Electron Optics and Electron Microscopy", Taylor and Francis Ltd., London, Barnes and Noble Book, N. Y. (1972)

89. M. E. Haine, "The Electron Microscopy", Interscience, N.Y. (1961)

90. G. Thomas, "Transmission Electron Microscopy of Metals", John-Wiley and Sons, N. Y. (1962)

91. R. D. Heidenreich, "Fundamental of Transmission Electron Microscope" Interscience, N. Y. (1964)

92. P. B. Hirsch, A. Howie and M. J. Whelan, Phil. Trans. Roy. Soc., A252 499 (1960)

93. H. Bethe, Ann. Phy., 87 55 (1950)

94. H. Heshimoto, M. Maunami and T. Naiki, Phil. Trans. Roy. Soc. A253 459 (1961)

95. D. P. Ewald, Ann. d. Phys., 49 1, 117 (1916); 54 519 (1917)

96. Z. G. Pinsker, "Electron Diffraction", Butterworth, London (1953)

97. G. Fisher, D. Grieg and E. Mooser, Rev. Sci. Instr., 34 842 (1961)

98. J. H. Fermer and A. Knekshus, Rev. Sci. Instr., 36 763 (1965)

99. W. D. Edwards, J. Sci. Instr. 42 432 (1965)

100. S. D. Hottman and H. A. Pohl, Rev. Sci. Instr., 42 387 (1971)

101. van der Pauw, Philips Res. Rept., 13 1 (1958)

102. van der Pauw, Philips Tech. Rev., 20 220 (1958)

103. T. M. B. Baleshta and J. D. Keys, Am. J. Phys., 36 23 (1968)

104. M. Schlesinger, J. Electrochem. Soc., 121 667 (1974)

105. R. P. Elliott, "Constitution of Binary Alloys", Supp. 1, McGraw-Hill, N. Y., 734 (1965)

106. G. S. Cargill III., J. Appl. Phys., 41 12 (1970)

107. B. G. Bagley and D. Turnbull, J. Appl. Phys., 39 5681 (1968)

108. P. A. Albert, K. Kovac, H. R. Lilienthal, T. R. McGuire and Y. Nakamura, J. Appl. Phys., 38 1258 (1967)

109. A. W. Goldstein, W. Rostober and F. Schossbuger, J. Electrochem. Soc., 104 (1957)

110. K. T. Ziehlke, W. S. Dritt and C. H. Mahoney, Metal Progr., 77 No. 2, 84 (1960)

111. V. P. Moiseev, Acad. Sci. U.S.S.R., 26 382 (1962)

112. J. Dixmier and K. Doi, Compt. Rend., 257 2451 (1963)

113. J. Dixmier, K. Doi and A. Guinier in "Physics of Noncrystalline Solids", ed. J. A. Prins, 67 (1964)

114. A. H. Graham, R. W. Lindsay and H. J. Reed, J. Electrochem. Soc., 109 1200 (1962); 112 401 (1965)

115. N. V. Kotel'nikov, N. A. Korenev, P. A. Malimon and T. D. Ermolina, Sov. Phys.-Doklady 7 No. 10, 896 (1962)

116. N. F. Mott and R. W. Gurney, Rept. Progr. Phys., 5 46 (1938)

117. W. H. Zachariasen, J. Am. Chem. Soc., 54 3841 (1932)

118. J. B. Bernal, Nature, 185 68(1960)

119. G. L. Moss, M.Sc. Thesis, University of London (1961)

120. O. S. Heavens, Single Crystal Films, The MacMillan Company, N. Y. 383-394 (1964)

121. B. W. Kinston, R. Pascula and M. Prutton, Thin Solid Films 6 267 (1970)

122. N. A. Korenev, Acad: Sci., U.S.S.R. 29 651 (1965)

123. M. Schlesinger andS. L. Chow (unpublished results)

124. T. Kanbe and K. Kanomatsu, J. Phys. Soc. Japan 24 1396 (1968)

125. U. Admon and A. Bar-or, J. Appl. Phys. 44 2300 (1973)

126. G. S. Cargill III and R. W. Cochrane, in "Amorphous Magnetism", ed. H. O. Hooper and A. M. deGraff, p. 313, (1973)

127. J. Goddard and J. G. Wright, Brit. J. Appl. Phys., 15 806 (1964)

128. E. B. Davies and P. J. Grundy, Phys. Stat. Sol., (a) 8 89 (1971)

129. C. T. Woo, M. Schlesinger, J. Rezek and S. L. Chow, (to be published in Materials Science and Engineering, 1974)

130. J. S. Salko and K. H. Olsen, J. Appl. Phys., 32 2035 (1961)

131. M. Schlesinger and J. P. Marton, J. Phys. Chem. Solid, 29 188 (1968)

132. S. T. Pai, J. P. Marton and J. Brown, J. Appl. Phys., 43 282 (1972)

133. G. Bates, J. Appl. Phys., 37 1164 (1966)

134. J. G. M. deLau, J. Appl. Phys., 41 5355 (1970)

135. M. Schlesinger and J. P. Marton, J. Appl. Phys., 40 507 (1968)

136. S. T. Pai and J. P. Marton, J. Appl. Phys., 43 4972 (1972)

137. C. A. Neugebauer, J. B. Newkirk and D. A. Vermilyea, "Structure and Properties of Thin Films", John-Wiley & Sons, N. Y., 253(1959)

138. S. Mader and A. S. Norwick and H. Widmer, Acta, Met., 15 203 (1967)

139. A. Ganulee, J. Appl. Phys., 43 3943 (1972)

140. E. C. Crittenden, Jr. and R. W. Hoffman, J. Phys. Radium., 17 220 (1956)

141. M. Mayer, R. Nossek and H. Thomas, J. Phys. Radium., 17 204 (1956)

142. W. Cirkler, Z. Physics, 147 481 (1957)

143. K. L. Chopra and S. K. Bahl, J. Appl. Phys., 38 3607 (1967)

144. H. Danison and A. Colombani, Compt. Rend. 252 3992 (1961), 253 411 (1961)

145. P. S. Galepov, Phys. Metals and Metall. 34 No. 5, 134 (1972)

146. J. Luttinger, Phys. Rev., 112 739 (1958)

147. F. Seitz, "The Modern Theory of Solids", McGraw-Hill, N. Y., 183 (1940)

148. J. Volger, Phys. Rev., 29 1023 (1950)

149. R. H. Bube, Appl. Phys. Lett., 13 136 (1968)

150. G. H. Blound, R. H. Bube and A. L. Robinson, J. Appl. Phys., 41 2190 (1970)

151. J. Heleskivi and T. Salo, J. Appl. Phys., 43 740 (1972)

152. K. Lipskis, A. Sakalas and J. Viscakas, Phys. Stat. Sol., 4 K217 (1971)

153. J. Drake and M. Schlesinger, Solid State Commun., 11 1597 (1973)

154. J. Drake and M. Schlesinger, Phys. Rev., B8 5221 (1973)

155. E. Snow and J. T. Waber, Acta. Metall., 17 623 (1969)

156. C. M. Hurd, "The Hall Effect in Metals and Alloys", p. 330, Plenum Press, N. Y. (1972).

157. E. M. Pugh and N. Roscober, Rev. Med. Phys. 25 151 (1953)

AUTHOR'S VITA

3rd March 1945	Born in Shanghai, China
May 1969	Graduated from the Nanyang University Singapore with B.Sc. degree
May 1970	Graduated from the Nanyang University Singapore with B.Sc. (Hon.) degree
Oct. 1971	Graduated from the University of Western Ontario, Canada with M.Sc. degree
Nov. 1974	Graduated from the University of Windsor, Canada with Ph.D degree.

Publications

1. The Role of u.v. Light in the Inhibition of Electroless Deposition J. Electrochemical Soc. 119 1013 (1972).

2. Electron Microscope Study of the Nucleation and Growth of Electroless Cobalt and Nickel. J. Electrochemical Soc. 119 1614 (1972)

3. Electron Microscope Studies of an Improved Sensitizer Solution J. Electrochemical Soc. 120 875 (1973)

4. Electron Microscope Investigation of Mixed Stannous Chloride/Palladium Chloride Catalysts for Plating Dielectric Substrates. J. Electrochemical Soc. 121 738 (1974)

5. Twins in Electroless Copper Films. Accepted for Publication in Materials Science and Engineering